OULU 2021
C 802

ACTA UNIVERSITATIS OULUENSIS

Harisankar Nellattukuzhi Sreenivasan

SYNTHESIS AND ALKALI ACTIVATION OF MAGNESIUM-RICH ALUMINOSILICATES

UNIVERSITY OF OULU GRADUATE SCHOOL;
UNIVERSITY OF OULU,
FACULTY OF TECHNOLOGY

ACTA UNIVERSITATIS OULUENSIS
C Technica 802

HARISANKAR NELLATTUKUZHI SREENIVASAN

SYNTHESIS AND ALKALI ACTIVATION OF MAGNESIUM-RICH ALUMINOSILICATES

Academic dissertation to be presented with the assent of the Doctoral Training Committee of Technology and Natural Sciences of the University of Oulu for public defence in the OP-Pohjola auditorium (L6), Linnanmaa, on 8 October 2021, at 12 noon

UNIVERSITY OF OULU, OULU 2021

Acta Univ. Oul. C 802, 2021

Supervised by
Associate Professor Päivö Kinnunen

Reviewed by
Assistant Professor Erika La Plante
Associate Professor Jørgen Skibsted

Opponent
Associate Professor Isabella Lancelloti

ISBN 978-952-62-3058-0 (Paperback)
ISBN 978-952-62-3059-7 (PDF)

ISSN 0355-3213 (Printed)
ISSN 1796-2226 (Online)

Cover Design
Raimo Ahonen

PUNAMUSTA
TAMPERE 2021

Nellattukuzhi Sreenivasan, Harisankar, Synthesis and alkali activation of Magnesium-rich aluminosilicates.
University of Oulu Graduate School; University of Oulu, Faculty of Technology
Acta Univ. Oul. C 802, 2021
University of Oulu, P.O. Box 8000, FI-90014 University of Oulu, Finland

Abstract

Alkali-activated materials (AAMs) are alternative cementitious materials with lower carbon footprints compared to traditional Portland cement (PC). In addition to Ca, Si, and Al, the precursors used in the preparation of AAMs can sometimes include considerable amounts of Mg, so that Mg significantly influences the structure and properties of AAMs. When compared to Ca, Si, and Al, relatively few studies have focused on the role of Mg in AAMs. This thesis deals with alkali activation of Mg-rich aluminosilicate precursors with the following objectives: 1) preparation, characterization, and estimation of alkaline reactivity of Na-Mg aluminosilicate glasses; 2) synthesis of AAMs from Na-Mg aluminosilicate glasses and their detailed characterization to understand the fate of Mg; and 3) estimation of the potential of phlogopite as a Mg-rich raw material for alkali activation.

The structural study of Na-Mg aluminosilicate glasses indicates that the higher cationic field strength (CFS) of Mg than Na makes Mg preferable as a network modifier, whereas Na acts as a charge compensator. Alkaline reactivity studies of Na-Mg aluminosilicate glasses reveal that as Mg replaces Na in glasses, the reactivity of the glasses increases initially, attains a maximum, and then drops. This trend can be explained by the interplay between glass depolymerization and optical basicity: depolymerization dictates the glass reactivity initially, while the effect of optical basicity dominates at later stages. Detailed structural study of AAMs prepared from Na-Mg aluminosilicate glasses indicates that Mg in AAMs exists as an amorphous magnesium silicate (AMS) phase, but the existence of this phase is not well documented in the literature. The driving force for AMS formation is the high CFS of Mg, which leads to effective stabilization of the depolymerized silicate species. The absence of hydrotalcite-group phases from these AAMs is due to the depletion of Al by zeolite production. The assessment of phlogopite mineral as a Mg-rich precursor for alkali activation indicates that untreated phlogopite is highly inert. However, thermal treatment could enhance the alkaline reactivity of phlogopite.

Keywords: alkali-activated materials, aluminosilicate glasses, amorphous magnesium silicate, cationic field strength, fate of Mg, geopolymer, hydrotalcite, phlogopite

Nellattukuzhi Sreenivasan, Harisankar, Mg-rikas alumiinisilikaattien synteesi ja alkalin aktivointi.
Oulun yliopiston tutkijakoulu; Oulun yliopisto, Teknillinen tiedekunta
Acta Univ. Oul. C 802, 2021
Oulun yliopisto, PL 8000, 90014 Oulun yliopisto

Tiivistelmä

Alkali -aktivoidut materiaalit (AAM) ovat vaihtoehtoisia sementtimateriaaleja, joilla on pienempi hiilijalanjälki verrattuna perinteiseen portland -sementtiin (PC). Ca: n, Si: n ja Al: n lisäksi esiasteissa (joita käytetään AAM: ien valmistukseen) voi joskus olla huomattava määrä Mg: tä, ja tämä johtaa siihen, että Mg vaikuttaa merkittävästi AAM: ien rakenteeseen ja ominaisuuksiin. Verrattuna Ca, Si ja Al, on ollut suhteellisen vähän tutkimuksia, joissa keskitytään Mg: n rooliin AAM: issä. Tämä opinnäytetyö käsittelee Mg-rikkaiden alumiinisilikaattiesiasteiden alkaliaktivaatiota seuraavilla tavoitteilla: 1) Na-Mg-alumiinisilikaattilasien alkalisen reaktiivisuuden valmistelu, karakterisointi ja arviointi; 2) synteesi AAM: istä Na-Mg-alumiinisilikaattilasista ja niiden yksityiskohtainen karakterisointi Mg: n kohtalon ymmärtämiseksi; 3) Flogopiitin potentiaalin arviointi Mg-rikkaana raaka-aineena alkalin aktivoimiseksi.

Na-Mg-alumiinisilikaattilasien rakennetutkimus osoittaa, että Mg: n korkeamman kationisen kentänvoimakkuuden (CFS) takia Na: n vuoksi Mg on edullinen verkon muokkaajana, kun taas Na toimii varauksen kompensoijana. Na-Mg-alumiinisilikaattilasien alkaliset reaktiivisuustutkimukset paljastavat, että kun Mg korvaa Na: n lasissa, lasien reaktiivisuus kasvaa aluksi ja saavuttaa maksimin, minkä jälkeen se laskee. Tämä suuntaus voidaan selittää lasin depolymeroinnin ja optisen emäksisyyden välisellä vuorovaikutuksella: depolymerointi sanelee aluksi lasin reaktiivisuuden, kun taas optisen emäksisyyden vaikutus hallitsee myöhemmässä vaiheessa. Yksityiskohtainen rakenteellinen tutkimus AAM: ista, jotka on valmistettu Na-Mg-alumiinisilikaattilasista, osoittaa, että Mg AAM-yhdisteissä esiintyy amorfisena magnesiumsilikaatti (AMS) -faasina, jonka olemassaoloa ei ole hyvin dokumentoitu kirjallisuudessa. AMS: n muodostumisen liikkeellepaneva voima on Mg: n korkea CFS, mikä johtaa depolymeroitujen silikaattilajien tehokkaaseen vakautumiseen. Hydrotaltsiittiryhmän faasien puuttuminen näistä AAM: ista on havaittu johtuvan Al: n ehtymisestä zeoliittituotannolla. Flogopiittimineraalin arviointi Mg-rikkaana esiasteena alkalin aktivoitumiselle osoittaa, että käsittelemätön flogopiitti on erittäin inerti. Lämpökäsittely voi kuitenkin parantaa flogopiitin emäksistä reaktiivisuutta.

Asiasanat: alkaliaktiiviset materiaalit, alumiinisilikaattilasit, amorfinen magnesiumsilikaatti, flogopiitti, geopolymeeri, hydrotalsiitti, kationinen kentänvoimakkuus, Mg: n kohtalo

Dedicated to my mom, dad, and sister

Acknowledgments

This thesis work was performed in the Fibre and Particle Engineering Research Unit at the University of Oulu, Finland, from 2016–2020. Funding for this work was received from the European Union's Horizon 2020 Research and Innovation Programme under the Marie Skłodowska-Curie COFUND Grant Agreement No. 713606 (I4FUTURE), as well as "Novel synthesis methods for porous ceramics from mine tailings," under Academy of Finland (292526). The author also thanks the Oulu University Scholarship Foundation and the University of Oulu Graduate School for financial support.

This work would have been impossible without the careful guidance and unrelenting support I received from my principal supervisor, Assoc. Prof. Päivö Kinnunen, who was always there to help me, irrespective of whether I had small or big issues. I also express my sincere gratitude to my ex-principal supervisor, Prof. Mirja Illikainen, for her valuable mentoring and for providing me with the opportunity to join the research unit in 2016. I am heavily indebted to my co-supervisor, Prof. John L. Provis, for his guidance in the area of material science. I am grateful to my co-supervisor, Assoc. Prof. Wei Cao, for his guidance, especially in the field of synchrotron-based characterization techniques.

I am grateful to the reviewers of this thesis, Asst. Professor Erika La Plante and Assoc. Prof. Jørgen Skibsted. I am thankful to my follow-up group members, Dr. Stanislav Gornostayev, and Dr. Katja Ohenoja for their valuable suggestions. I am also grateful to laboratory engineer Dr. Tuomas Stoor for all the help he extended in office-related matters.

For assisting me with research work and improving the quality of research publications, I am obliged to all my publication co-authors: Prof. Marko Huttula, Prof. Ville-Veikko Telkki, Dr. Anu M. Kantola, Dr. Elijah Adesanya, Assoc. Prof. Minna Patanen, Dr. Eetu-Pekka Heikkinen, Dr. Priyadharshini Perumal, MSc. He Niu, Dr. Yongfeng Hu, Dr. Qunfeng Xiao, Dr. Mohsen Shakouri. I am also thankful to Dr. Satu Ojala, Asst. Prof. Juho Yliniemi, and Asst. Prof. Tero Luukkonen for the assistance I received in research-related matters. I am grateful to Dr. Hoang Nguyen for his tips on thesis writing. I am obliged to all the lab technicians of our research unit: Elisa Wirkkala MSc, Jarno Karvonen MSc, and Jani Österlund MSc for helping me with matters related to performing lab experiments.

I am thankful to all the members of the Fibre and Particle Engineering Research Unit, especially to my office mates Adediran Adeolu MSc and Amzad Bhuyan MSc, for the help they extended to me on professional as well as personal matters. I am

thankful to Dr. Prem Kumar Seelam for helping me when I moved to Oulu in 2016. I sincerely thank Tun Tun Nyo MSc, Marcin Selent MSc, Santtu Heinilehto MSc, Sami Saukko MSc, Pasi Juntunen MSc, Leena Palmu MSc, Tommi Kokkonen MSc, and Riku Mattila MSc for the help they extended in research-related matters.

My deepest gratitude goes to my mom, dad, and sister for all the support I have received from them over the years. My parents, both of whom are school teachers by profession, tried to instill a sense of passion for knowledge since my childhood, and this formed the basis of my passion for research, without which I could not have finished this thesis work. I also appreciate the support I received from them when I decided to move to Finland to pursue my doctoral degree.

Oulu, 8th of October 2021 Harisankar N. Sreenivasan

List of abbreviations

AA	alkali activation
AAM	alkali-activated material
BE	binding energy
BFS	blast furnace slag
CFS	cation field strength
e.g.	exempli gratia
etc.	et cetera
FA	fly ash
ICP-OES	inductively coupled plasma optical emission spectrometer
i.e.	id est
EDS	energy-dispersive X-ray
FWHM	full width at half maximum
MAS NMR	magic angle spinning nuclear magnetic resonance
MMCE	mixed-modifier cation effect
RT	room temperature
SEM	scanning electron microscopy
STEM	scanning transmission electron microscopy
TG-MS	thermogravimetry-mass spectrometry
XANES	X-ray absorption near edge spectroscopy
XPS	X-ray photoelectron spectroscopy
XRD	X-ray diffraction

List of original publications

This thesis is based on the following publications, which are referred to throughout the text by their Roman numerals:

I Sreenivasan, H., Kinnunen, P., Adesanya E., Patanen, M., Kantola, A. M., Telkki, V.-V., Huttula, M., Cao, W., Provis, J. L., & Illikainen, M. (2020). Field strength of network-modifying cation dictates the structure of (Na-Mg) aluminosilicate glasses. *Frontiers in Materials, 7*, 267. https://doi.org/10.3389/fmats.2020.00267

II Sreenivasan, H., Cao, W., Hu Y., Xiao, Q., Shakouri, M., Huttula, M., Provis, J. L., Illikainen, M., & Kinnunen, P. (2020). Towards designing reactive glasses for alkali activation: Understanding the origins of alkaline reactivity of Na-Mg aluminosilicate glasses. *PlOS ONE, 15*(12), e0244621. https://doi.org/10.1371/journal.pone.0244621

III Sreenivasan, H., Adesanya E., Niu, H., Perumal, P., Kantola, A. M., Telkki, V.-V., Huttula, M., Cao, W., Provis, J. L., Illikainen, M., & Kinnunen, P. (2021). Evidence of formation of an amorphous magnesium silicate (AMS) phase during alkali activation of (Na-Mg) aluminosilicate glasses. *Cement and Concrete Research, 145*,106464. https://doi.org/10.1016/j.cemconres.2021.106464

IV Sreenivasan, H., Kinnunen, P., Heikkinen, E.-P., & Illikainen, M. (2017). Thermally treated phlogopite as magnesium-rich precursor for alkali activation purpose. *Minerals Engineering, 113*, 47–54. https://doi.org/10.1016/j.mineng.2017.08.003

In all these original publications, the author of this thesis was involved in conceptualization, designing, conducting, and analysis of experiments, as well as writing the first draft and revised versions of each manuscript, with guidance from the supervisors and co-authors. In Publication I, EA and AMK helped the author in performing SEM and MAS NMR experiments respectively. In Publication II, the XANES experiments were performed with the help of WC, YH, MS, and QX. In Publication III, EA helped with SEM experiments, HN helped with TG-MS experiments, and AMK helped with MAS NMR experiments. In Publication IV, HH performed thermodynamic simulation.

Contents

Abstract
Tiivistelmä
Acknowledgments **9**
List of abbreviations **11**
List of original publications **13**
Contents **15**
1 Introduction **17**
1.1 Background ... 17
1.2 Aims of the thesis ... 18
1.3 Outline of the thesis ... 19
2 Fundamentals **21**
2.1 Need for improved understanding of the fate of Mg in AAMs ... 21
2.2 Structure and reactivity of Na-Mg aluminosilicate glasses ... 23
2.3 Phlogopite as a Mg-rich precursor for AA ... 27
3 Materials and methods **29**
3.1 Materials ... 29
3.1.1 Phlogopite ... 29
3.1.2 Metakaolin ... 29
3.1.3 Other materials ... 29
3.2 Methods ... 30
3.2.1 Material characterization ... 30
3.2.2 Preparation of Na-Mg aluminosilicate glasses ... 33
3.2.3 Alkaline dissolution experiments ... 34
3.2.4 Preparation of AAMs from Na-Mg aluminosilicate glasses ... 34
3.2.5 Phlogopite thermal treatment ... 35
3.2.6 Acid dissolution experiments ... 36
4 Results and discussion **37**
4.1 Characterization of Na-Mg aluminosilicate glasses ... 37
4.1.1 XRD analysis of glasses ... 37
4.1.2 SEM analysis of glasses ... 38
4.1.3 XPS analysis of glasses ... 40
4.1.4 ^{29}Si MAS NMR analysis of glasses ... 43
4.1.5 XANES analysis of glasses ... 52
4.2 Alkaline reactivity of Na-Mg aluminosilicate glasses ... 55
4.2.1 Si and Al alkaline solubility ... 55

4.2.2 XRD analysis of solid residues 57
4.2.3 TEM analysis of solid residues 58
4.2.4 ^{27}Al MAS NMR analysis of residues 59
4.2.5 Further discussion on reactivity 62
4.3 The fate of Mg in AAMs prepared from Na-Mg aluminosilicate glasses 64
4.3.1 Compressive strength analysis of AAMs 64
4.3.2 XRD analysis of AAMs 65
4.3.3 ^{27}Al MAS NMR spectral analysis of samples 68
4.3.4 ^{29}Si MAS NMR spectral analysis of the samples 70
4.3.5 SEM analysis of AAMs 74
4.3.6 TG-MS characterization of AAMs 79
4.4 Alkaline reactivity of thermally treated phlogopite 82
4.4.1 Phase changes during thermal treatment 82
4.4.2 Enhancement in Si and Al solubility upon thermal treatment 84
4.4.3 Understanding the K solubility 86
4.4.4 Understanding the fate of Fe and Mg 87
4.4.5 Estimation of the composition of the precipitated products 91
4.4.6 The overall alkali activation potential of P1600g 92
5 Conclusion and outlook **95**
List of references **101**
Original publications **111**

1 Introduction

1.1 Background

Global warming is a grave concern for human civilization and the environment. The current consensus is that one of the main reasons for global warming is the man-made emissions of greenhouse gases [1], [2]. Emissions of CO_2 account for as much as 76% of the total global greenhouse gas emissions [2]. Hence, massive pressure is being placed on reducing CO_2 emissions in all economic sectors, including the industrial sector. The Portland cement (PC) industry forms a significant feature of human civilization, as cement is second only to water in terms of the annual overall volumetric consumption of resources on earth by humanity [3]. Cement production has undergone considerable growth during the last couple of decades and is anticipated to double (in terms of production volume) by 2050 owing mainly to the large demand in developing countries [4]. However, even now, the cement industry contributes as much as 5–8% of the overall CO_2 emissions [5]. Half of these emissions are raw material-related, while the other half are associated with the fuel-related aspects in the manufacturing process [6]. Considering the significant contribution of the cement industry toward CO_2 emissions and the fact that cement demand is poised to rise considerably in the near future [7], a great need exists to develop novel cementitious materials with lower carbon footprints.

Alkali-activated materials (AAMs), also referred to as geopolymers, are considered good alternative cementitious materials with lower carbon footprints [8], [9]. Their synthesis can be tuned in a convenient manner to promote desirable properties, such as low shrinkage, high compressive strength, slow or fast setting, fire resistance, acid resistance, and low thermal conductivity [10]. In this way, AAMs can replace PC in many infrastructure-related applications and may be considered in niche applications, such as high-temperature applications, production of lightweight materials, underground well construction, and stabilization of hazardous wastes [8].

AAMs are prepared by the alkaline activation of raw materials, such as metakaolin, blast furnace slag (BFS), and coal fly ash (FA). The Ca content of the raw materials dictates the dominant binder phase formed during alkali activation: use of high-Ca raw materials results in the formation of a calcium aluminosilicate hydrate gel (C-A-S-H) as the dominant binder phase; intermediate Ca raw materials and blends lead to a mixture of C-A-S-H and an alkali aluminosilicate phase (N-A-

S-H, if the Na content in the system is high); the low-Ca raw materials produce N-A-S-H [8].

In addition to Ca, Si, and Al, the raw materials used for the preparation of AAMs can possess considerable amounts of Mg. In this situation, Mg can have a significant influence on the formation of the product phases, thereby affecting the structure, properties, and final use of AAMs. When compared to Ca, Si, and Al, relatively few studies have focused on the role of Mg in AAMs. This necessitates more detailed studies on alkali activation of Mg-containing raw materials. However, most of the Mg-rich precursors normally used for AAM synthesis contain impurities/other significant constituents whose presence may complicate the precise identification of the fate of Mg in AAMs. In this respect, simple Mg-containing synthetic precursors, such as Na-Mg aluminosilicate glasses, could be valuable in providing better insights into the fate of Mg.

Another significant aspect is the need for natural Mg-rich minerals for the production of AAMs. Many of the raw materials used in AAMs contain inherently low amounts of Mg. The practice of adding external MgO to the alkali activation mixture is not environmentally sound, as MgO is produced mostly through decomposition of $MgCO_3$, which results in CO_2 emissions [10]. This means that new non-carbonate-based and cheap Mg-rich raw materials need to be sought out for alkali activation. Phlogopite is a promising candidate, and it is locally available in Finland in large quantities as mining waste.

1.2 Aims of the thesis

This thesis deals with alkali activation of Mg-containing precursors. The major objectives of the work are the following:

1. Preparation, characterization, and estimation of alkaline reactivity of Na-Mg aluminosilicate glasses (Publications I and II).
2. Synthesis of AAMs from Na-Mg aluminosilicate glasses and their detailed characterization to understand the fate of Mg (Publication III).
3. Estimation of the potential of phlogopite as a Mg-rich raw material for alkali activation purposes (Publication IV).

1.3 Outline of the thesis

This thesis includes five chapters. Chapter 1 provides overall background information related to the thesis work and the main objectives under consideration. Chapter 2 is a continuation of the background information dealing mostly with the technical aspects involved. This chapter includes the following: the need for improved understanding of the fate of Mg in AAMs; fundamentals of the structure and reactivity of the Na-Mg aluminosilicate glasses; and phlogopite as a Mg-rich precursor for AA. Chapter 3 introduces the materials used, sample preparation methods, and sample characterization techniques. Chapter 4 contains the findings of this research work and a detailed discussion of the same. Chapter 5 provides a brief summary of the major findings of the thesis work, as well as suggested research themes for future work.

2 Fundamentals

2.1 Need for improved understanding of the fate of Mg in AAMs

Mg-containing phases can have significant effects on the structure and properties of AAMs. The possible fates of Mg in the AAMs include the following phases: brucite ($Mg(OH)_2$); hydrotalcite-group minerals ($[Mg_{1-x}Al_xOH][OH, ½CO_3]\cdot mH_2O$), Mg (hydroxy-)carbonates, and/or Mg silicate hydrate (M-S-H). Each of these has its own effect on the structure, properties, and final use of the AAMs. Late brucite formation can cause volume expansion issues in cementitious materials [11], [12]. Higher formation of hydrotalcite can decrease Al integration into the C-A-S-H phase and can produce AAMs with enhanced mechanical strength [13]. AAMs possessing high amounts of hydrotalcite are known to offer superior resistance to chloride attack [14] and to carbonation degradation [15]. The M-S-H phase can act as a high-strength cementitious material [16] and is a suitable material in the context of nuclear waste management [12], [17], [18]. If exposure of cementitious material to atmospheric CO_2 can result in the formation of Mg (hydroxy-)carbonates, this can make the manufacturing of cementitious material more ecofriendly through a reduced carbon footprint [12]. Considering the significant manner in which Mg-containing phases can impact the structure, properties, and final use of AAMs, a greater need exists for improved understanding of the fate of Mg during the alkali activation process.

A summary of the major products and the fate of Mg in AAMs prepared from Mg-rich precursors reported in previous literature studies is provided in Table 1. The primary aim of this table is to provide a glimpse into the different types of Mg-rich precursors used for AAM synthesis and the fate of Mg in each (hence, the table has not been prepared in an exhaustive manner). Hydrotalcite-group phases (having different OH/CO_3 and Mg/Al and ratios) are the most commonly observed Mg-containing phase in AAMs synthesized from a wide array of Mg-containing precursors [15], [19]–[28]. The presence of certain Mg-containing phases, such as M-S-H, Na-Mg aluminosilicate hydrate (N-M-A-S-H), and brucite, has been reported in AAMs prepared from high-Mg Ni slags [27], [29]. A few studies have also failed to detect any specific Mg-containing phase, even though Mg-rich precursors were used to prepare the AAMs [28], [30], [31]. Walling et al. [26] activated blends of $Mg(OH)_2$ and SiO_2 with $NaAlO_2$ and observed no hydrotalcite phase at high Si:Al ratios, while a hydrotalcite phase was detected in the case of a

blend with low Si:Al (equivalent MgO content of blends used in the study = 27–34 wt.%). Those authors reported that $Mg(OH)_2$ in the precursor shows a rather low reactivity. However, one basic question to be addressed is why $Mg(OH)_2$ reacts in blends with low Si:Al ratios (to form hydrotalcite), but does not in the case of blends possessing high Si:Al ratios. Kinnunen et al. [30] synthesized AAM from a stone wool + fly ash mixture using an activation solution consisting of a NaOH + $NaAlO_2$ mixture (the MgO content of the systems = 9.2–12.2 wt.%) but detected no hydrotalcite phase in any of the AAMs. Zhang et al. [31] prepared AAMs from BFS through sodium silicate activation and observed no hydrotalcite phases in the AAMs (the MgO content of BFS was 9.3 wt.%). Considering these three studies, open questions that remain in the literature include the reason why no Mg-containing phase is formed in certain AAMs and whether any chance exists for the formation of Mg-containing phases that are not easily detected in certain AAMs. Addressing these issues may be feasible through alkali activation of simple Mg-containing raw materials, such as Na-Mg aluminosilicate glasses.

Table 1. Main products formed and the fate of Mg during alkali activation of Mg-rich precursors, according to selected studies (Reprinted [adapted] under CC BY 4.0 license from Publication III © 2021 Authors).

Precursors	Mix design (mole ratio): Si:Al:Mg:Ca:Na	Fate of Mg	Major product	Ref.
BFS	1: (0.33–0.43): (0.21–0.26): (0.99–1.27): (0.18-0.22)	HT	C-A-S-H	[15]
BFS	1: 0.40: 0.29: 1.00: 0.09	HT	C-A-S-H	[19]
BFS+MK	1: 0.60: 0.23: 0.96: 0.17	HT	C-A-S-H	[20]
BFS+ FA	1: 0.43: (0.23–0.61): 0.77: (0.16–0.34)	HT	C-A-S-H	[21]
BFS +$Mg(OH)_2$	1: 0.44: (0.34–4.07): 1.24: (0.36–0.82)	HT	C-A-S-H	[22]
BFS +MgO	1: 0.36: (0.45–0.54): 1.38: (0.15–0.24)	HT	C-A-S-H	[23]
Stone wool	1: 0.45: 0.41: 0.41: 1.94	HT	C-A-S-H	[24]
Synthetic precursors	1: (0.05–0.15): (0.05–0.29): (0.70–1.15): (0.03 -0.08)	HT	C-A-S-H	[25]
Synthetic slags	1: (0.44–0.53): (0.01–0.70): (1.02–1.61): 0.26	HT	C-A-S-H	[26]
High Mg-NS	1: (0.07–0.15): (0.73 -1.08): (0.07–0.21): (0.47–0.51)	M-S-H + HT+B	M-S-H	[27]

Precursors	Mix design (mole ratio): Si:Al:Mg:Ca:Na	Fate of Mg	Major product	Ref.
High Mg-NS + FA	1: (0.33–0.62): (0.03–0.43): (0.08–0.13): (0.22–0.30)	N-M-A-S	N-M-A-S	[29]
SiO_2 + $Mg(OH)_2$ + $NaAlO_2$	1: 1.50: 3.00: 0: 1.50	HT	Zeolite	[28]
SiO_2 + $Mg(OH)_2$ + $NaAlO_2$	1: (0.60–1.00): (1.20–2.00): 0: (0.60–1.00)	---	Zeolite	[28]
Stone wool + FA	1: (0.46–0.80): (0.18–0.43): (0.18–0.38): (0.39 -1.81)	---	C-A-S-H	[30]
BFS	1: 0.48: 0.40: 1.21: 0.16	---	C-A-S-H	[31]

Note: a) For column 1: BFS—blast furnace slag; MK—metakaolin; FA—fly ash; NS—nickel slag. b) For column 3: HT—hydrotalcite-like phase; B—brucite; M-S-H—magnesium silicate hydrate; N-M-A-S—sodium magnesium aluminosilicate hydrate. c) For column 4: C-A-S-H—calcium aluminosilicate hydrate; M-S-H—magnesium silicate hydrate; N-M-A-S—magnesium aluminosilicate hydrate.

2.2 Structure and reactivity of Na-Mg aluminosilicate glasses

To gain better insights into the fate of Mg during alkali activation, Na-Mg aluminosilicate glasses are chosen as precursors for alkali activation. This necessitates some basic introduction regarding the structure and reactivity of Na-Mg aluminosilicate glasses.

The structure of Na-Mg aluminosilicate glass can be shown to form from amorphous silica in a stepwise manner, as depicted in Fig. 1. The structure of amorphous silica has a 3-D network of completely polymerized silicate (SiO_4) tetrahedra (where all oxygen atoms act as bridging oxygens, BOs). Here, all the Si species can be represented in Q^4 form; in the Q^n representation, n ($0 \leq n \leq 4$) denotes the number of BOs surrounding the Si atom as the nearest neighbor. The introduction of Na breaks the bond between BO and Si, leading to the formation of non-bridging oxygen (NBO). The formation of NBOs inevitably leads to network depolymerization through the creation of Si species, such as Q^0, Q^1, Q^2, and Q^3. If the quantity of Na introduced is large, some Na may exist in free oxide form [32]. The introduction of Al brings another degree of complexity into the system. The added Al exists as tetrahedral aluminate (AlO_4) species, where the apical oxygen atoms (which are BO [33]) carry an electrical charge deficit. Hence, a part of the Na originally performing a network modifier role in the system now needs to act

as charge compensators for the apical oxygen. This leads to the depletion of the Na acting as a network modifier in the system, thereby resulting in network polymerization. In the presence of AlO_4 species, Na is preferred for charge-compensation roles over network modification roles [34].

The introduction of Mg introduces a further degree of complexity into the system. Similar to Na, Mg can either perform a network modification role or a charge-compensation role. This raises the question of how the network-modifying and charge-compensation roles are distributed among Na and Mg. This distribution can have a significant impact on the structure of glass and will be influenced by the charge density of Na and Mg. The charge density of cations can be represented as the cation field strength, CFS. CFS = Z/r^2, where r denotes cation radius in Å and Z represents cation charge. The CFS of Mg is 0.46 $Å^{-2}$, while the same for Na is 0.18 $Å^{-2}$ [35].

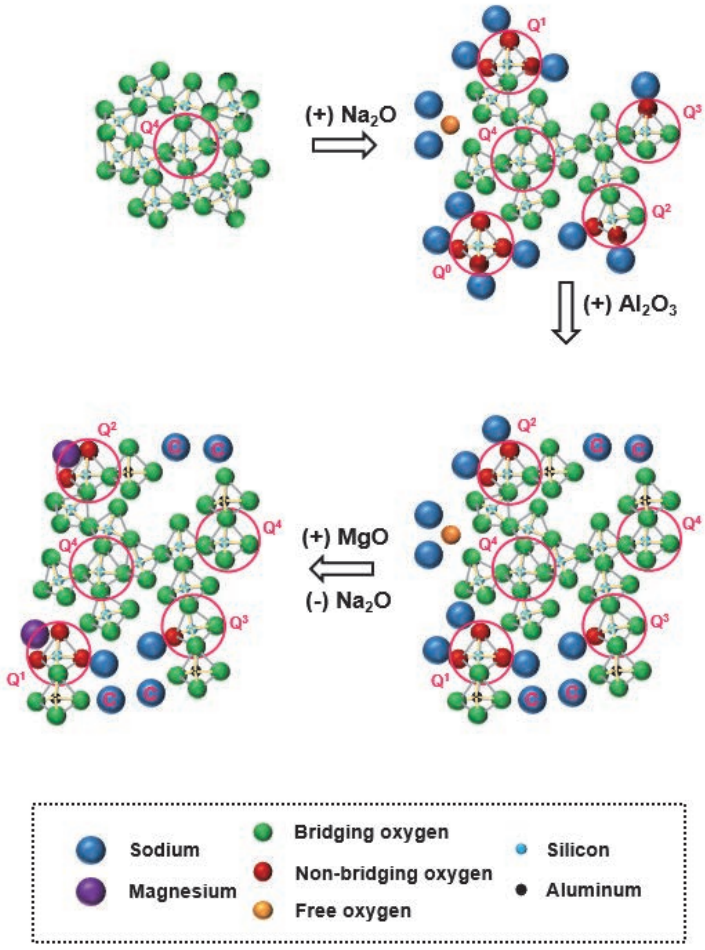

Fig. 1. Evolution of Na-Mg aluminosilicate glass from a silica melt. Regarding the roles of network-modifying cations, charge compensators are marked as "C", whereas network modifiers are those near NBO and free oxide forms are those near free oxygen (Reprinted [adapted] under CC BY 4.0 license from Publication I © 2020 Authors).

Several studies in the literature have focused on Mg-containing aluminosilicate glasses. Allu et al. [36] studied Ca-Mg aluminosilicate glasses using ^{29}Si and ^{27}Al MAS NMR spectroscopy and in situ Raman spectroscopy. They observed that increases in the Mg/Ca ratio of the aluminosilicate glasses resulted in the following: 1) in the case of silicon speciation, the proportion of highly depolymerized $Q^n(mAl)$

species increases, and 2) in the case of aluminum coordination, the proportion of pentahedral and octahedral aluminum increases, while that of tetrahedral aluminum decreases. This indicates a straining of the aluminum environments. Allwardt et al. [37] studied K-Ca-Mg aluminosilicate glasses using ^{27}Al MAS NMR spectroscopy, and observed that an increase in the Mg content of the aluminosilicate glasses increased the average aluminum coordination. Neuville et al. [38] studied Ca-Mg aluminosilicate glasses and Mg aluminosilicate glasses using Raman spectroscopy and ^{27}Al MAS NMR spectroscopy. They found that: 1) in the case of Ca-Mg aluminosilicate glasses, increases in the Mg/Ca ratio led to increases in the proportion of pentahedral and octahedral aluminum, and 2) in the case of Mg aluminosilicate glasses, a decrease in the silica content of the glasses resulted in increased proportions of pentahedral and octahedral aluminum. Kuryaeva et al. [39] studied the properties of the glass and the melt of diopside composition ($CaMgSi_2O_6$) in comparison with those of anorthite composition ($CaAl_2Si_2O_8$), and argued that Mg^{2+} can fulfill the functions of both network modifier and network former. Bista et al. [40] studied Ca-Mg aluminosilicate glasses using ^{27}Al, ^{29}Si, and ^{17}O MAS NMR spectroscopies, and observed that increases in the Mg/Ca content of glasses increased the proportion of pentahedral and octahedral aluminum. Weigel et al. [41] studied Li-Na-K-Ca-Mg-Sr-Ba-Zn aluminosilicate glasses using Brillouin spectroscopy and observed that glasses with higher Mg content possessed higher atomic density and elastic moduli. This could have arisen due to tighter binding of Al-O to Mg with high CFS. Lee et al. [42] studied the extent of disorder in Mg aluminosilicate glasses using ^{27}Al and ^{17}O MAS NMR spectroscopy. These authors observed that as the Mg content of aluminosilicate glasses increases: 1) the topological and configurational disorder around Al increases, and 2) Mg preferentially forms Mg-O-Si bonds than Mg-O-Al bonds. They also reported that the degree of aluminum avoidance is lower in the case of Mg aluminosilicate glasses when compared to Na or Ca aluminosilicate glasses.

One of the often-used parameters for estimating glass reactivity is NBO/T, the number of non-bridging oxygens/number of tetrahedral cations [43], [44], and it is expressed as

$$\frac{\mathrm{NBO}}{\mathrm{T}} = \frac{2\left(X_{MO}+X_{M_2O}+3f_{M_2O_3}-X_{Al_2O_3}-(1-f)X_{M_2O_3}\right)}{X_{SiO_2}+2X_{Al_2O_3}+2(1-f)X_{M_2O_3}}, \quad (1)$$

where X = the mole fraction of the specific oxide component; MO = MgO, CaO, SrO, FeO, etc.; M_2O= K_2O, Li_2O, Na_2O, etc.; M_2O_3= Al_2O_3, Cr_2O_3, Fe_2O_3, etc., and f = the mole fraction of the M_2O_3 performing the role of network modifier. A glass

with a higher NBO/T is expected to exhibit higher reactivity. One of the flaws of the NBO/T concept is that it cannot differentiate the influence of different types of network-modifying cations on glass reactivity. Another parameter used to estimate glass reactivity, optical basicity (Λ), gives due consideration to the influence of different types of network-modifying cations [43], [45]–[48]. The optical basicity (Λ) is expressed as

$$\Lambda = \frac{\Sigma X_i n_i \Lambda_i}{\Sigma X_i n_i}, \quad (2)$$

where X_i = the mole fraction of the specific oxide component, n_i represents the number of oxygens in the formula unit of the oxide component (e.g., $n_i = 1$ for K_2O and $n_i = 3$ for Fe_2O_3), Λ_i denotes the optical basicity of the oxide component (e.g., $\Lambda_i = 0.48$ for SiO_2 , $\Lambda_i = 1.15$ for Na_2O, $\Lambda_i = 1.4$ for K_2O, and $\Lambda_i = 0.78$ for MgO) [43]. A glass with higher optical basicity is expected to exhibit higher reactivity.

2.3 Phlogopite as a Mg-rich precursor for AA

Phlogopite is a Mg-rich mineral and is found in significant proportions in mine tailings worldwide, including Finland. The apatite mine in Siilinjärvi (Eastern Finland), which has been producing apatite since 1979 [49], has resulted in storage of over 220 Mt of phlogopite mine tailings. At present, only a small fraction of phlogopite is being used for commercial purposes, such as filler material and potassium fertilizer for organic farming, while the major fraction is stored as tailings in a tailings dam [50]. Phlogopite contains significant amounts of Si and Al, making it a potential candidate for alkali activation. Phlogopite is a clay mineral that is classified under the mica category of phyllosilicates, and its unit structure consists of an octahedral sheet (made of MgO_6 units) sandwiched between two tetrahedral sheets (made of SiO_4 and AlO_4 units), as shown in Fig. 2. The ideal chemical composition of phlogopite corresponds to $KMg_3AlSi_3O_{10}(OH)_2$. However, naturally occurring phlogopite is often contaminated with Fe^{2+} (which partially replaces Mg^{2+}) and F^- (which partially replaces OH^-) [51].

Phlogopite cannot be used directly for alkali activation because of its high chemical stability [52], [53]. However, thermal treatment can improve the pozzolanic activity of clay and clay minerals [54]–[56]. During thermal treatment, hydroxyl groups are removed from the structure, and this promotes the formation of amorphous phases, thereby leading to increased reactivity [56], [57]. Each clay mineral is characterized by an optimum activation temperature for pozzolanic

activity [54], [55], [58], [59]; however, in the case of phlogopite, no previous studies have reported thermal treatment for improving pozzolanic activity.

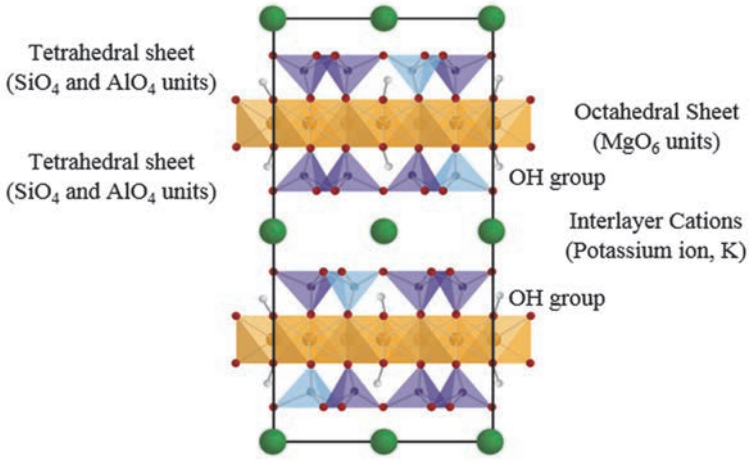

Fig. 2. Structure of an ideal phlogopite. The color codes for elemental spheres are as follows: Si (dark blue), Al (light blue), O (red), H (white), and K (green) (Reprinted, with permission, from Publication IV © 2017 Elsevier Ltd.).

3 Materials and methods

3.1 Materials

3.1.1 Phlogopite

The phlogopite (Phl) was secured from LKAB Minerals Oy, Siilinjärvi, Eastern Finland. It was generated as a by-product from apatite ore processing at the mine. The chemical composition of phlogopite is shown in Table 2.

Table 2. Chemical composition of phlogopite and metakaolin (% wt/wt) (LOI = loss on ignition; Others = Na_2O+ TiO_2 + Co_3O_4) (Reprinted [adapted], with permission, from Publication IV © 2017 Elsevier Ltd.).

Sample	SiO_2	Al_2O_3	MgO	Fe_2O_3	K_2O	CaO	F	LOI	Others
Phlogopite	40.9	9.8	23.8	9.1	8.6	1.5	0.5	5.6	0.6
Metakaolin	53.5	36.4	0.3	1.0	2.6	0.1	-	5.9	0.2

3.1.2 Metakaolin

Metakaolin was used as a standard alkali activation material; its alkaline solubility was used as a benchmark for comparison purpose. The Metastar 402 brand of metakaolin was procured from Imerys Minerals. The chemical composition of metakaolin is shown in Table 2.

3.1.3 Other materials

Sodium hydroxide (purity >99%), obtained from Merck (Germany), was used to prepare alkaline solutions for dissolution experiments (section 3.2.3). Nitric acid (64–66%), obtained from Sigma-Aldrich, was used to prepare acid solutions of various concentrations for neutralization (section 3.2.3) and acid solubility tests (section 3.2.6). Deionized water was used whenever required. Raw materials used for the preparation of glasses (original aluminosilicate glasses and reference glasses) included Al oxide (purity 99.5%, Sigma-Aldrich), Si oxide (purity 99.5%, Alfa Aesar); Mg oxide (purity 99.0%, Sigma-Aldrich), and Na carbonate (purity 99.0 %, Sigma-Aldrich). For XPS (X-ray photoelectron spectroscopy) analysis, the following reference compounds were used: Na carbonate (purity 99.0%, Sigma-

Aldrich), Mg carbonate (40.0–43.5% as MgO, Sigma-Aldrich;), Mg oxide (purity 99.0%, Sigma-Aldrich), and Mg hydroxide (purity 99.0%, Sigma-Aldrich).

3.2 Methods

3.2.1 Material characterization

Milling of samples, wherever required, was performed using a vibratory disc mill (Retsch RS 200) operated at a speed of 1000 rpm. The sample was milled for 1–5 min until the desired particle size distribution was obtained.

The particle size of powdered samples was estimated using an LS 13 320 laser diffraction particle size analyzer (Beckman Coulter). Air was used as a dispersion medium in all experiments. This method has several advantages, including high sensitivity, high resolution size information, and good reproducibility [60]. However, one of its limitations is that the refractive index of the particle of interest should differ substantially from that of the surrounding medium to ensure detection [60].

The chemical composition of the samples was analyzed using a PANalytical AXios^{mAX} XRF spectrometer fitted with a rhodium tube with a maximum power rating of 4 kW. This method has advantages, such as high accuracy and precision and high orderliness of the emission spectrum [61]. However, it has disadvantages, such as possible errors in calibration and matrix effects [61].

X-ray diffraction (XRD) patterns were recorded using a Rigaku SmartLab 9 kW XRD instrument. The analysis employed the following parameters: Co Kα radiation ($K\alpha_1$=1.78892 Å; $K\alpha_2$=1.79278 Å; $K\alpha_1/K\alpha_2$=0.5); scan rate of 3°⁄min between 5° and 85° 2θ; 0.02°/step. The phases were identified using “X'pert HighScore Plus” (PANalytical) software. Before the XRD analysis, samples were subjected to hand grinding using a mortar and pestle made of corundum to achieve randomness of crystallite orientation and to obtain sufficient crystallites to produce a representative distribution of intensity. The advantages of this method include high reliability and sensitivity [62]. The disadvantages include the possibility of not detecting phases whose content is less than 2% and the difficulty in measuring disordered phases [62].

The elemental concentrations in liquid samples were determined using a Thermo Fisher Scientific iCAP6500 Duo inductively coupled plasma optical emission spectrometer (ICP-OES) fitted with a Cetac ASX-520 auto sampler. The

preparation of samples before ICP-OES analysis was as follows: a sample with a volume of 1 mL was introduced into a polypropylene centrifuge tube (volume = 30 mL) and 3 mL of aqua regia was added. The centrifuge tubes were stoppered and sonicated for 20 min. The sample tube was then filled up to 25 mL with deionized water and centrifuged for 20 min at 10,000 rpm. The supernatant was subjected to elemental analysis by ICP-OES. This method has several advantages, including high sensitivity and reproducibility and low matrix effects [63]. Its drawbacks include continuum background emission, and spectral overlap [63].

Scanning transmission electron microscope (STEM) images of samples were recorded using a JEOL JEM-2200FS fitted with an energy-dispersive X-ray spectroscopy (EDS) detector (JEOL Dry SD100GV, 100 mm^2, 0.98 Sr). The advantages of this method include high magnification and resolution, while one disadvantage is that analysis is restricted to electron-transparent materials [64].

A Bruker Avance III 300 spectrometer operated at 59.65 MHz was employed for recording the ^{29}Si MAS NMR spectra of the samples. The samples were introduced into zirconia rotors 7 mm in diameter. The experiments involved the following parameters: rotation frequency of 7 kHz and 8192 scans with a 3 s repetition rate. A relaxation time of 3 s reproduced the spectra of metakaolin-based alkali-activated materials previously reported in the literature and was deemed sufficient to produce reliable spectra. For referencing chemical shifts, tetramethylsilane (set to 0 ppm) was used as the external standard. In the case of ^{27}Al experiments, a frequency of 78.24 MHz was used, and 2048 scans were collected with 2 s repetition time. For referencing chemical shifts, $Al(NO_3)_3$ (set to 0 ppm) was used as the external standard. Solid state MAS NMR spectroscopy has many advantages, as it is non-destructive, non-invasive, selective to nuclei, and gives reliable quantification [65]. Its disadvantages include the fact that expertise is needed for data treatment and some samples may possess low sensitivity and require long analysis [65].

The ^{29}Si MAS NMR spectral deconvolutions (into Gaussian components) in case of glasses were performed using Origin software. During deconvolution, the following procedure was employed: the parameters of Gaussian components, such as the full width at half maximum (FWHM), peak position, and intensity, were varied independently; the χ^2 minimization principle was used. Limitations associated with this procedure are addressed in section 4.1.4.

A Thermo Fisher Scientific XPS System (ESCALAB 250Xi) was employed for XPS analysis of the samples. For referencing the binding energies (BEs) of various elements, the BE of adventitious carbon (C1s, defined to be 284.6 eV) was

used. The advantages of this method include reliable atomic quantification, as well as quantification of oxidation states and easy interpretation [66]. Its disadvantages include that the information pertains only to the surface (1–20 nm) and the samples must be compatible with a high-vacuum environment [66].

A Zeiss Ultra Plus field emission scanning electron microscope (FESEM) fitted with an Oxford energy-dispersive X-ray spectroscopy (EDS) detector was employed for recording SEM images of samples. Aztec software was used for performing elemental mapping. The sample preparation involved impregnation in epoxy resin and hardening for 24 h. After resin hardening, the sample surface was subjected to a polishing process using diamond (0.25 μm) paste to obtain a smoothened surface. The smoothened surface was then sputter coated with carbon to form a conductive layer. The advantages of this method include high resolution and magnification and reliable quantitative elemental analysis [67]. The disadvantages of the method are that it reveals only surface information, the sample must be vacuum sensitive, and the possibility of artifacts exists [67].

The X-ray absorption experiments were conducted in the Canadian Light Source, located in Saskatoon, Canada. The SXRMB beamline of the station was used for all measurements. Powder samples were transferred onto double-sided conductive carbon tape and introduced into the vacuum chamber. SiO_2 and Si wafers were used for energy calibration and referencing. The fluorescence spectra of the samples were recorded using a 7-element SDD detector. In case of Si references and samples having high Si content, the total electron yield was used (this was done to prevent the issue of the self-absorption connected with the fluorescence mode). The data treatment consisted of normalization, background removal, and XANES analysis and was performed using the Athena program [68]. The advantages of this method include: it is element specific, it can be used as a local atomic probe, and it can reveal information about coordination as well as oxidation state of elements [69]. One of its disadvantages is its limitations in distinguishing scattering atoms with slight differences in atomic number [69].

The compressive strength of the AAMs was measured using a Zwick 100 machine. During the measurements, a loading force ramp of 2.4 kN/s was used until failure.

Thermal analysis was performed using a Netzsch STA 449 F3 TGA-DTA/DSC analyzer (Selb, Germany) fitted with a mass spectrometer (MS). The sample (mass = 20 mg) was placed in an alumina crucible, which was then heated with a ramp rate of 10 °C min^{-1} up to 700 °C in a nitrogen environment (purge rate = 200

mL/min). Prior to thermal analysis, the samples were homogenized by grinding using a mortar and pestle made of corundum.

3.2.2 Preparation of Na-Mg aluminosilicate glasses

A series of 10 Na-Mg aluminosilicate glasses (compositions shown in Table 3) were prepared. Raw materials were mixed in appropriate amounts and ground in a vibratory disc mill (Retsch RS 200) for 3 min at a speed of 1500 rpm. The ground mixture (each batch consisted of 50 g) was placed in a platinum crucible and introduced into a Nabertherm high-temperature furnace (HT 08/18). The sample was heated to 1600 °C at a rate of 20 °C/min, then held at the highest temperature for 1.5 h. The melt obtained at the end of the heating procedure was subjected to rapid quenching by pouring into water held at RT. The glasses so obtained were subjected to drying at 60 °C for 48 h. The dried glasses were melted again (same procedure as mentioned before) to ensure homogeneity of the glasses. The glasses were then grounded in a vibratory disc mill (1000 rpm 1–5 min).

Reference glasses used for NMR and XPS analysis were also synthesized in a similar manner as above. Reference glasses with the following formulas were prepared: $Mg_{0.50}Si_{2.50}Al_{1.00}O_{7.00}$, $Na_{0.75}Si_{2.50}Al_{0.75}O_{6.50}$, $Mg_{0.25}Si_{2.50}Al_{0.50}O_{6.00}$, $Na_{1.00}Si_{2.50}Al_{1.00}O_{7.00}$, $Mg_{0.50}Si_{1.00}O_{2.50}$, $Na_{1.00}Si_{1.00}O_{2.50}$, $Mg_{1.00}Si_{1.00}O_{3.00}$, $Na_{2.00}Si_{1.00}O_{3.00}$, $Mg_{1.00}Si_{1.00}O_{3.00,}$ $Na_{2.00}Si_{1.00}O_{3.00}$, $Mg_{0.50}Al_{1.00}Si_{2.50}O_{7.00,}$ and $Na_{1.00}Al_{1.00}Si_{2.50}O_{7.00}$.

Table 3. Composition of Na-Mg aluminosilicate glasses (Under CC BY 4.0 license from Publication III © 2021 Authors).

Glass code	Formula of glass	MgO (wt.%)	NBO/Si
G1	$Na_{1.60}Al_{0.40}Si_{1.00}O_{3.40}$	0	
G2	$Na_{1.42}Mg_{0.09}Al_{0.40}Si_{1.00}O_{3.40}$	2.8	
G3	$Na_{1.25}Mg_{0.18}Al_{0.40}Si_{1.00}O_{3.40}$	5.6	
G4	$Na_{1.07}Mg_{0.26}Al_{0.40}Si_{1.00}O_{3.40}$	8.6	
G5	$Na_{0.90}Mg_{0.35}Al_{0.40}Si_{1.00}O_{3.40}$	11.6	1.25
G6	$Na_{0.72}Mg_{0.44}Al_{0.40}Si_{1.00}O_{3.40}$	14.7	
G7	$Na_{0.54}Mg_{0.53}Al_{0.40}Si_{1.00}O_{3.40}$	18.0	
G8	$Na_{0.37}Mg_{0.62}Al_{0.40}Si_{1.00}O_{3.40}$	21.3	
G9	$Na_{0.19}Mg_{0.70}Al_{0.40}Si_{1.00}O_{3.40}$	24.8	
G10	$Mg_{0.80}Al_{0.40}Si_{1.00}O_{3.40}$	28.3	

Note that calcium was omitted from the aluminosilicate glass compositions. Calcium is usually present in Mg-containing aluminosilicate glass systems used in the context of alkali activation. However, in this study, calcium was omitted because the presence of calcium could sometimes interfere with the precise identification of the fate of magnesium in AAMs. All the glasses used in the study had a Si:Al ratio of 2.5, which was formulated after consulting the Si:Al ratios of the Mg-containing blast furnace slags used in alkali activation contexts [11], [13], [15], [19], [21]. The network modifier content (based on the NBO/T ratio) of the glasses used in the study roughly corresponds to the network modifier content of the blast furnace slags used in the context of alkali activation [11], [13], [15], [19], [21].

3.2.3 Alkaline dissolution experiments

These experiments were conducted in the case of Na-Mg aluminosilicate glasses, thermally treated phlogopite samples, and metakaolin. Before being subjected to alkaline solubility experiments, each sample was milled to an average particle size between 1 μm and 10 μm. The solubility experiment involved treating material with 6 M NaOH solution (liquid to solid ratio = 40 w/w) in a polypropylene bottle. The experiment was conducted at 23±0.5 °C for 24 h. During the entire duration of the experiment, the polypropylene bottle was subjected to shaking motion (frequency = 150/min) with the help of a horizontal shaking table (IKA KS 260 orbital shaker). After the solubility test, the sample was filtered using a 0.45 μm filter paper. The filtrate was acidified with 6 M HNO_3 to a pH less than 2 (to avoid precipitation of the dissolved species). The elemental concentration of the acidified filtrate was determined by ICP. The solid residue remaining after the solubility test was washed with distilled water multiple times and dried in a desiccator at room temperature for 2 days.

3.2.4 Preparation of AAMs from Na-Mg aluminosilicate glasses

Both the glass precursor (100 g) and the alkaline solution (35 g of 6 M NaOH) were mixed in a high shear mixer (brand: IKA EUROSTAR 20) for 30 min at a speed of 3000 rpm. The mixed slurry was transferred to cylindrical plastic molds (25 mm diameter and 25 mm height) and then sealed airtight inside plastic bags. The sealed plastic bags were first kept for 1 day at 40 °C and later transferred to RT, where they were cured for 1 year. The AAM prepared from glass Gy was labeled AGy.

3.2.5 Phlogopite thermal treatment

The milled phlogopite sample (with an average particle size between 1 μm and 10 μm) was subjected to thermal treatment. This involved calcination of the sample (a batch consisted of 40 g sample placed inside a corundum crucible) at a series of temperatures from 100 °C to 1300 °C using a Nabertherm high-temperature furnace (HT 08/18). The heating rate employed was 20 °C/min and the sample was held at the final temperature for 30 min before being rapidly cooled to RT. The calcined sample was labeled as P*x*, where *x* represents the temperature of calcination. Calcination of phlogopite samples to 1400 °C and 1500 °C resulted in partial melting with poor flow properties. Hence, those samples were discarded. For estimating the melting behavior of the phlogopite sample, a thermodynamic simulation was performed for the chemical composition representing the phlogopite. This employed utilization of commercial FactSage software version 7.0 and its FactPS and FToxid databases. The results of the thermodynamic simulation, in the form of a temperature-pressure phase diagram, are shown in Fig 3. The thick line in the figure denotes the solidus below which only the solid phase exists. Complete liquid slag is obtained when the temperature is above 1550 °C. Hence, one sample was synthesized by melting phlogopite at 1600 °C using a platinum crucible and then rapidly cooling the melt by pouring it over a water-cooled copper plate. The sample so obtained was labeled as P1600g.

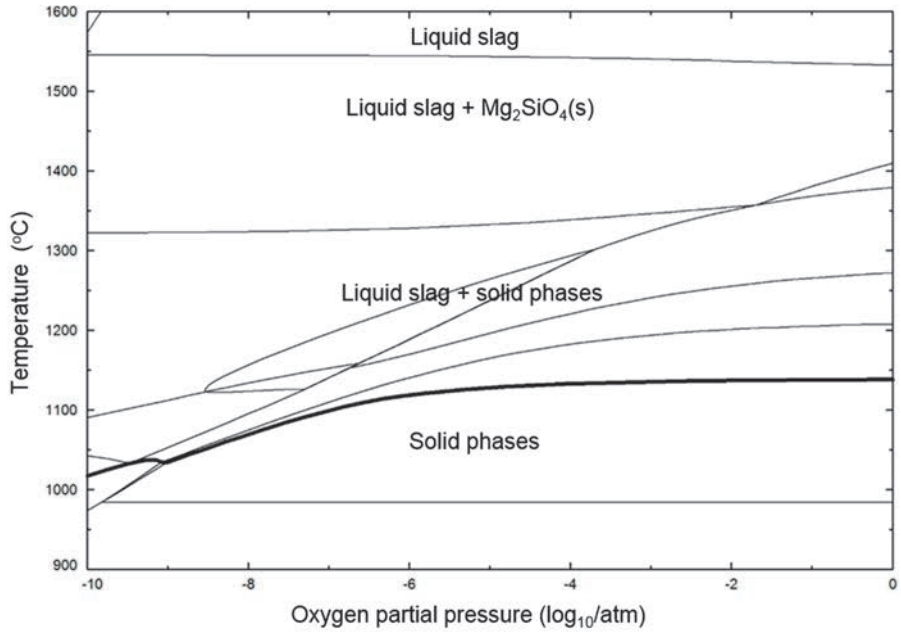

Fig. 3. The temperature-pressure phase diagram for a chemical system corresponding to phlogopite composition (Reprinted, with permission, from Publication IV © 2017 Elsevier Ltd.).

3.2.6 Acid dissolution experiments

The acid dissolution of the solid residue obtained from alkaline dissolution experiments was also performed to estimate the approximate composition of the precipitated products. Five different concentrations of HNO_3 (0.003 M, 0.010 M, 0.030 M, 0.100 M, and 0.300 M) were used for this experiment. The procedure adopted was similar to that of the alkaline solubility experiment, except for the following differences: 1) HNO_3 solution was used instead of NaOH solution, and 2) the experiment was conducted only for 10 min instead of 24 h.

4 Results and discussion

4.1 Characterization of Na-Mg aluminosilicate glasses

4.1.1 XRD analysis of glasses

Two distinct amorphous regions, along with a minor crystalline component, are visible in the XRD patterns (Fig 4.) of the Na endmember of the glass series (G1). One amorphous region (Am1) spreads from 17.0° to 32.0°, while the second (Am2) extends from 32.0° to 45.0°. The minor crystalline component is attributed to Na carbonate, which forms due to atmospheric carbonation of the free oxide form of Na present in the glass. Network-modifying cations can exist in free oxide form in glasses with high NBO/Si ratios [32].

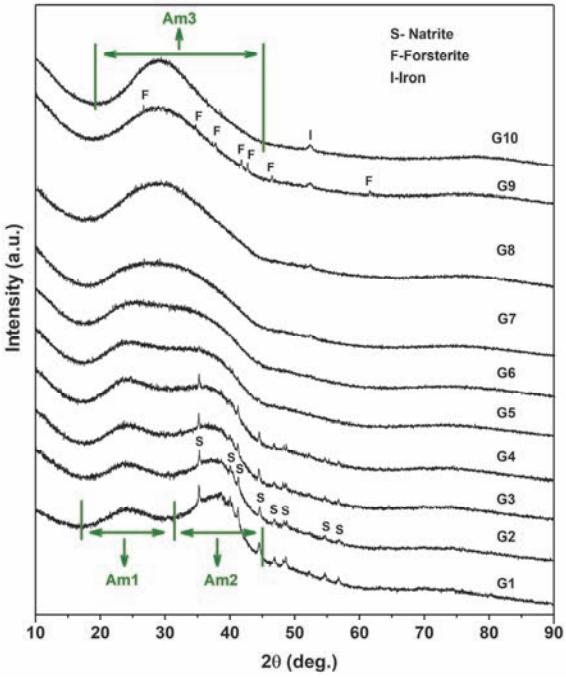

Fig. 4. Results of the XRD analysis of Na-Mg aluminosilicate glasses (Reprinted [adapted] under CC BY 4.0 license from Publication I © 2020 Authors).

As Mg is introduced into the Na endmember, Am1 remains almost intact. However, in the case of Am2, the introduction of Mg in the Na endmember leads to a reduction in the intensity. Toward the Mg endmember, Am2 merges with Am1, thereby leading to the formation of a new amorphous region (Am3).

With the incorporation of Mg in the Na endmember, the intensity of reflections of Na carbonate decreases. The crystalline contributions of Na carbonate are absent in all the samples of the glass series after G5. The glass G9 exhibits crystalline reflections of forsterite (Mg_2SiO_4), which has a composition known to offer high resistance to vitrification processes [70]. The formation of forsterite indicates the existence of Q^0 species. Presence of Q^0 species has been reported in glass systems having high NBO/Si ratios [32].

Note that a signal is visible at around 52.30° in certain samples (G8, G9, and G10). This is attributed to the Fe metal that originated from the steel grinding disc used for milling the samples.

4.1.2 SEM analysis of glasses

SEM analysis of glasses has been performed to understand the phase separation in glasses. Phase separation is a type of chemical disorder in glasses, wherein the cationic constituents do not distribute in a completely random fashion within the glass network. An important factor known to cause phase separation in silicate glasses is the nature of network-modifying cations [71].

SEM images, along with overlay of EDS elemental mapping of glasses, are shown in Fig. 5. The microscopic images of G1 and G6 reveal homogenous distributions of Si and Al, although the Na distribution in G1 shows regions of segregation that correspond to Na carbonate (which was found in XRD analysis of G1). The glasses G9 and G10, which form the Mg-rich glasses of the aluminosilicate glass series, reveal phase separation. G9 shows clear Si phase separation, while G10 shows both Si and Al phase separation to considerable extents. The presence of Mg (when compared to Na) is known to cause higher phase separation in silicate glasses [71], [72].

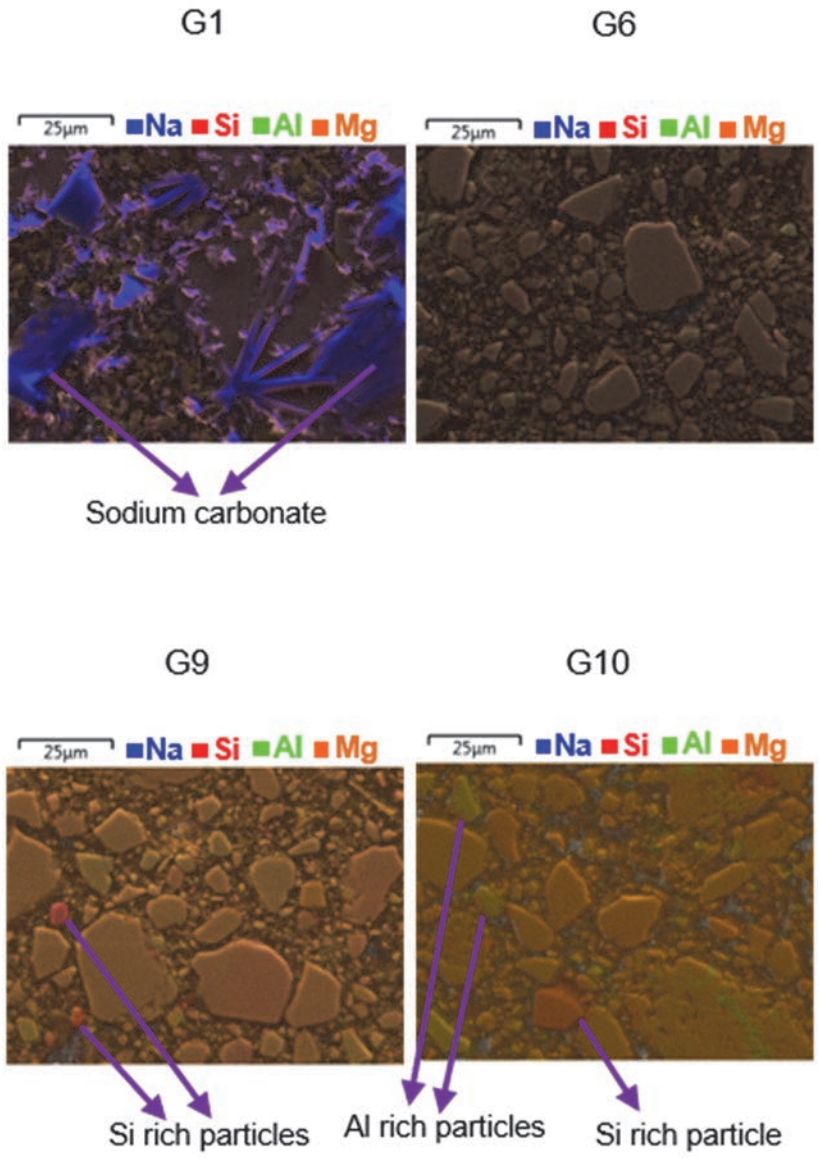

Fig. 5. SEM images and EDS elemental mapping overlay of glasses (Reprinted [adapted] under CC BY 4.0 license from Publication I © 2020 Authors).

4.1.3 XPS analysis of glasses

With the aim of obtaining insights into the role of Na in the studied glasses, the binding energies (BE) of sodium (Na 1s) were determined in the studied glasses and several reference compounds (Fig. 6). The reference compounds consisted of compounds where Na occurs exclusively as a network modifier/charge compensator/free-oxide. The BE of Na in the reference compounds follows the trend: free form < network modifier < charge compensator. In the case of the studied glasses, the Na 1s BE of the Na endmember lies between the regimes of the Na 1s BEs of the free form and the network modifier. The introduction of Mg in the glasses causes a gradual increase in BE, and it approaches close to the regime of a charge compensator in cases of glass compositions close to the Mg endmember. This leads to the conclusion that the Mg introduced into the Na endmember glass initially replaces Na as a network modifier and finally replaces Na as a charge compensator toward the Mg endmember.

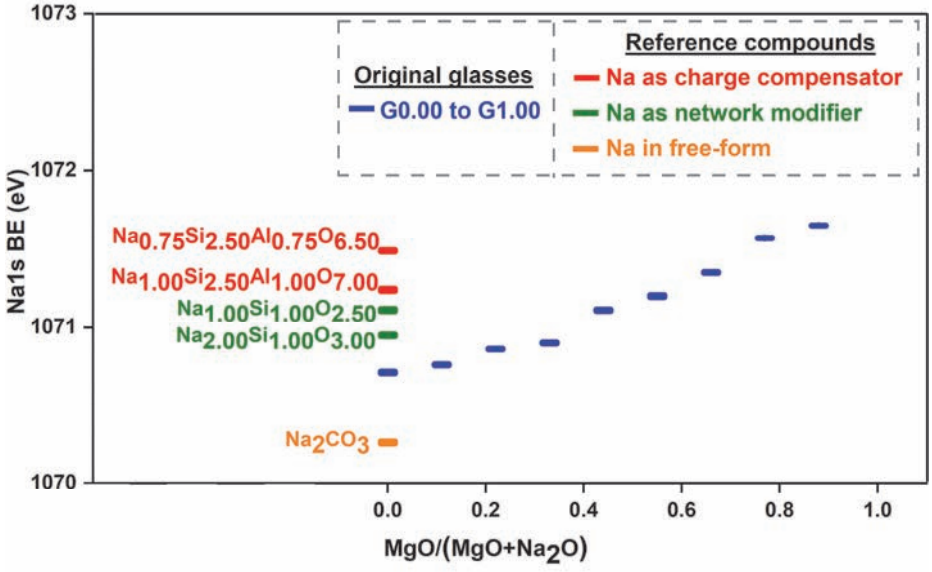

Fig. 6. Binding energy diagram for Na (Reprinted [adapted] under CC BY 4.0 license from Publication I © 2020 Authors).

The BE of Mg (2p) in the studied glasses and a few reference compounds (where Mg occurs solely as a free form/network modifier/charge compensator) has been

estimated (Fig. 7). The BE trend observed is as follows: network modifier < charge compensator (the free form of Mg can exist as $MgCO_3$, MgO, and/or $Mg(OH)_2$, where Mg exhibits different BEs). In case of the studied glasses, the following observation can be made regarding the Mg 2p BE trend: as the Mg content of glasses increases, the BE gradually increases and finally approaches the region of a charge compensator toward the Mg endmember. This implies that as Mg is introduced into the glass system, it initially acts as a network modifier and finally as a charge compensator toward the Mg endmember.

Combining the BE analysis of Na and Mg in the studied glasses, the following conclusion can be drawn: in an aluminosilicate glass system, Mg is preferred over Na for network modification, while Na is preferred over Mg for charge compensation. The role of Na and Mg, as indicated by XPS analysis, is shown in Fig. 8. SEM-EDS evidence for this role preference among Na and Mg in an aluminosilicate system is discussed later, in section 4.3.5.

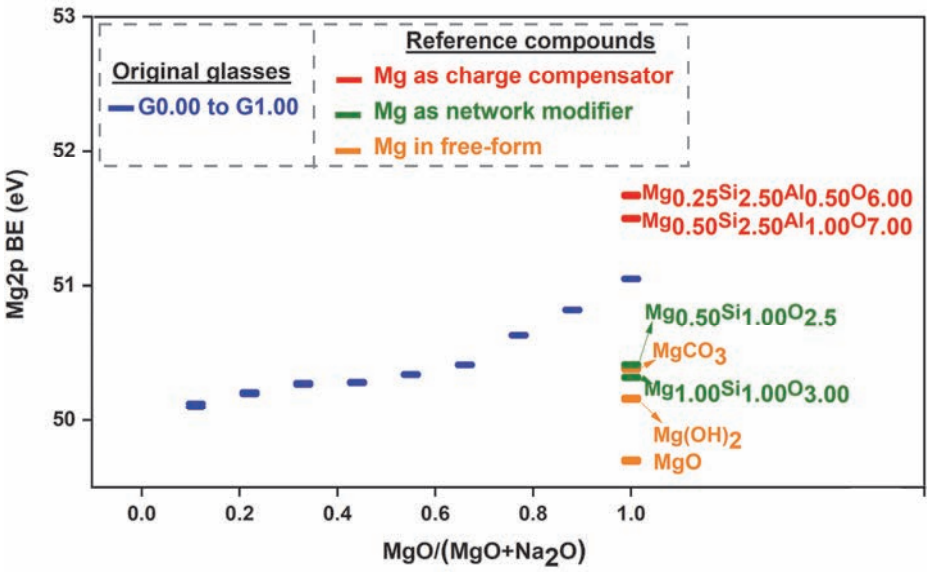

Fig. 7. Binding energy diagram for Mg (Reprinted [adapted] under CC BY 4.0 license from Publication I © 2020 Authors).

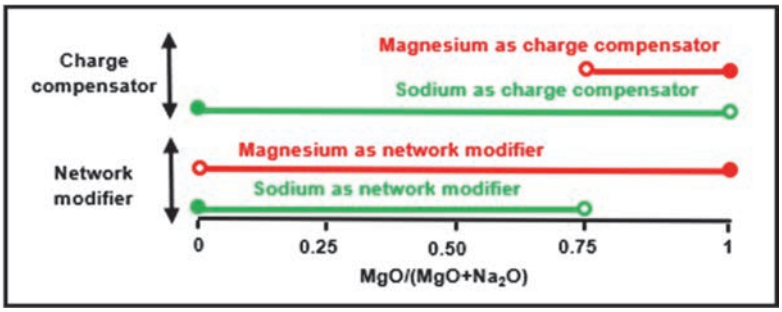

Fig. 8. Roles of Na and Mg in glasses, as concluded from XPS analysis (Reprinted [adapted] under CC BY 4.0 license from Publication I © 2020 Authors).

The role preference between Na and Mg, as implied by XPS analysis, can be explained by the concept of CFS. As Mg has a higher CFS than Na, it possesses a higher density of positive charge than Na. When compared to an apical oxygen atom (which is BO), an NBO atom has a higher density of negative charge. Mg (when compared to Na), with its high positive charge density, can effectively neutralize the NBO (which has a high negative charge density). Conversely, Na, with its low positive charge density, is more efficient at neutralizing apical oxygen (which has low negative charge density). This implies that Mg prefers to associate with NBO, thereby acting as network modifier. A similar rationale explains the preference of Na for a charge-compensation role (by associating with BO).

The O 1s BE increases as Na is replaced by Mg in the glass systems (Fig. 9). This occurs because the Mg-O bond has a less ionic character when compared to the Na-O bond [73]; hence, the O 1s BE in the Mg-O bond is high when compared to that in the Na-O bond [Publication I]. The Si 2p BE rises gradually as Mg replaces Na (Fig. 9), and it finally rises steeply toward the Mg endmember. As the Si-O bond is brought into closer proximity to a less ionic Mg-O bond (when compared to Na-O bond), the Si 2p BE is bound to increase according to the interjection rule [75]. The trend in BE of Al 2p is similar to that of Si 2p, and a similar explanation (as given for Si 2p BE trend) is also valid here.

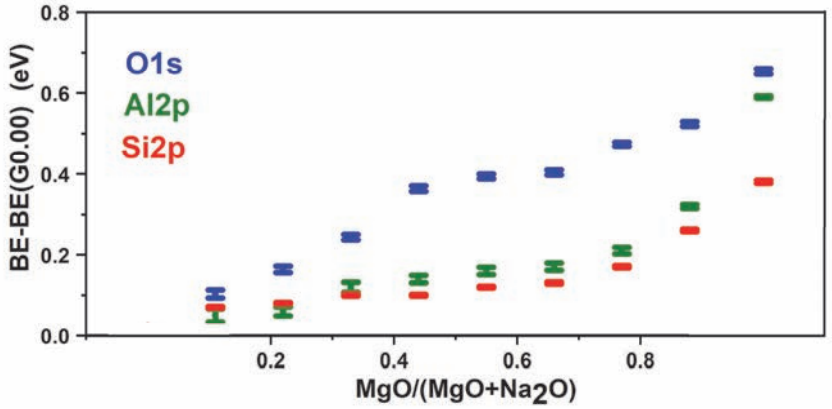

Fig. 9. The binding energy diagram for O, Al, and Si (Reprinted [adapted] under CC BY 4.0 license from Publication I © 2020 Authors).

4.1.4 ^{29}Si MAS NMR analysis of glasses

The Si in aluminosilicate glasses is known to occur almost exclusively in tetrahedral coordination under ordinary conditions of temperature and pressure [62]. Hence, the Si species in aluminosilicate glasses can be conveniently denoted by $Q^n(m\text{Al})$, where n ($4 \geq n \geq 0$) denotes the number of BO atoms around the Si atom, while m ($n \geq m \geq 0$) denotes the number of Al atoms that occupy the next-nearest neighbor sites around the Si atom. This implies that up to 15 different $Q^n(m\text{Al})$ Si species are possible in aluminosilicate glasses. These $Q^n(m\text{Al})$ Si species can be identified and quantified by credible deconvolution of the ^{29}Si NMR spectra [76], [77].

The majority of the studies previously reported on the Q^n species quantification in glasses by ^{29}Si NMR spectral deconvolution were performed on fully polymerized aluminosilicate glass systems. In those systems, the amount of network-modifying cations is just sufficient to neutralize the negative charge associated with tetrahedral aluminum species; hence, no depolymerization occurs in the glass network. In other words, Si in those systems can occur in a maximum of five states: $Q^4(4\text{Al})$, $Q^4(3\text{Al})$, $Q^4(2\text{Al})$, $Q^4(1\text{Al})$, and $Q^4(0\text{Al})$. This simplifies the spectral deconvolution process and allows its performance in a satisfactory manner since less overlap occurs among the various components. However, in the case of depolymerized aluminosilicate systems with excess network-modifying cations, performing spectral deconvolution is a big challenge, as up to 15 $Q^n(m\text{Al})$

components can intersect. Hence, relatively few studies have been conducted in this area. One significant attempt in this direction was made by Mysen et al. [76], who performed ^{29}Si NMR spectral deconvolution in a credible manner for up to 10 components. In the present study, we followed a similar procedure, but we also included contributions from highly depolymerized species, such as Q^0 and Q^1. Both these components were omitted in the work of the aforementioned authors. The highly depolymerized species are included in our work for the following reasons: 1) our glass systems contain higher amounts of network-modifying cations, and 2) XRD analysis of glasses provided evidence for the existence of Q^0 species (as reflections of crystalline forsterite appeared in sample G8).

The chemical shift values for various $Q^n(m\text{Al})$ components were estimated in the ^{29}Si MAS NMR spectra of the studied aluminosilicate glasses by performing deconvolutions for the spectra of a few simple reference glasses. The details are provided in the published work by the author (Publication I). $Mg_{1.00}Si_{1.00}O_{3.00}$ and $Na_{2.00}Si_{1.00}O_{3.00,}$ were used to estimate the chemical shift values for Q^0–Q^3 species in Mg silicate and Na silicate, respectively. $Mg_{0.50}Al_{1.00}Si_{2.50}O_{7.00}$ and $Na_{1.00}Al_{1.00}Si_{2.50}O_{7.00}$ were used to estimate the chemical shift values for $Q^4(m\text{Al})$ species in Mg aluminosilicate and Na aluminosilicate, respectively.

Considering the challenges associated with the ^{29}Si MAS NMR spectral deconvolution in the case of the studied aluminosilicate glasses, the credibility of spectral deconvolution was ensured in the following manner: (1) selecting appropriate chemical shift values and widths for each component by referring to the literature [76], [78]–[80] as well as by conducting spectral deconvolution for a few simple reference glasses, as mentioned before; (2) comparing the theoretical Si: Al ratio (the bulk value) to the experimental Si: Al ratio (estimated through spectral deconvolution); and (3) comparing the theoretical NBO/Si ratio (the bulk value) to experimental NBO/Si ratio (estimated through spectral deconvolution). The full details of the procedure followed are provided in the published work by the author (Publication I).

Despite the adoption of a rigorous deconvolution procedure, significant uncertainties are still possible, associated with the estimation of various $Q^4(m\text{Al})$ species. These uncertainties are due to: (1) uncertainty originating from chemical shift variation of the component, and (2) uncertainty evolving from width variation of the component. Thus, these two uncertainties were estimated individually, and the total uncertainty was calculated by summing up these two uncertainties. The full details of the uncertainty calculation are provided in the supporting information of the published work by the author (Publication I).

The ^{29}Si NMR spectrum of each aluminosilicate glass was deconvoluted into 11 components, denoting the known $Q^4(m\text{Al})$ species in these glasses. The spectral deconvolution in case of G1 is shown in Fig. 10, while those of the remaining aluminosilicate glasses are provided in the published work by the author (Publication I). The theoretical and experimental Si:Al ratios are similar for all glasses, except for glass compositions toward the Mg endmember, where theoretical values are lower than the experimental values (Fig. 11). This can reflect the existence of phase separation in glass compositions close to the Mg endmember, as seen in the SEM analysis. The theoretical values are higher for the NBO:Si ratio than for the experimental values for glasses having compositions close to the Na endmember, while both values are similar for glass compositions toward the Mg endmember (Fig. 11). As per the XRD characterization of the aluminosilicate glasses, in the case of glasses toward the Na endmember, a portion of Na occurs in a free form (observed as Na carbonate). This implies that the actual amount of Na that performs network modification or charge compensation is less than the bulk amount of Na. This can be the reason why the theoretical values for the NBO:Si ratio are higher than the experimental values for glasses having compositions close to the Na endmember.

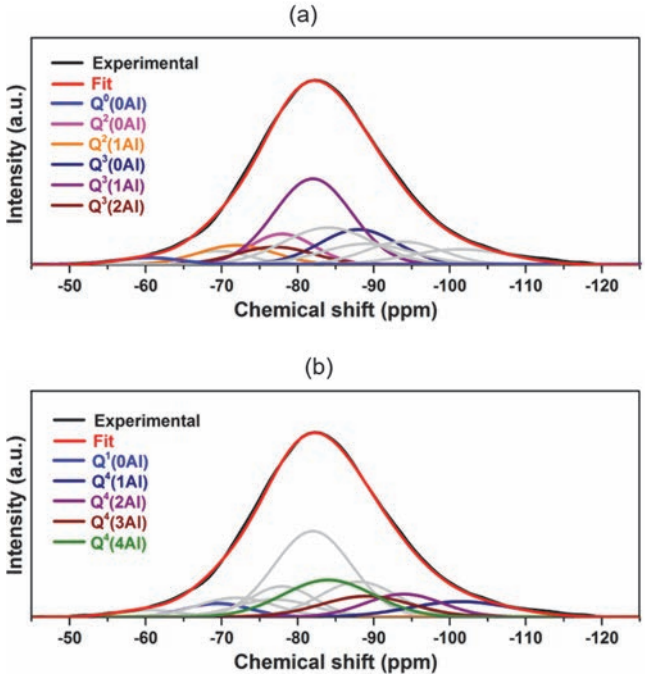

Fig. 10. ^{29}Si MAS NMR spectral deconvolution of G1 (a, b highlight different peaks within the deconvolution) (Reprinted [adapted] under CC BY 4.0 license from Publication I © 2020 Authors).

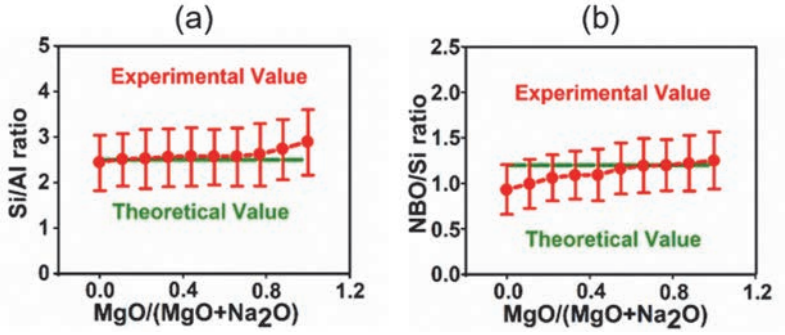

Fig. 11. (a) Si/Al ratio (theoretical vs. experimental). (b) NBO/Si ratio (theoretical vs. experimental) (Reprinted [adapted] under CC BY 4.0 license from Publication I © 2020 Authors).

An overview of Q^n speciation in the aluminosilicate glasses obtained by ^{29}Si NMR spectral deconvolution is shown in Fig. 12. The Na endmember (G1) mostly consists of Q^3 (45%), Q^4 (35%), and Q^2 (15 %) species. It has a smaller proportion of highly depolymerized species (Q^1 = 2% and Q^0 = 4%). As Mg is introduced initially into the Na endmember ($0< MgO/(MgO+Na_2O<0.75$), noticeable changes occur in the amounts of Q^3 and Q^2 species, while the proportion of Q^4 species remains almost unaltered (note that the Q^3 and Q^2 species are associated with network-modifying cations, while the Q^4 species are associated with charge-compensator cations). This observation agrees with the conclusion from XPS analysis that Mg introduced into the Na endmember preferentially acts as a network modifier. As the $MgO/(MgO+Na_2O$ increases from 0 to 0.75, the following trends in the proportions of Q^3 and Q^2 species are observed: 1) the amounts of Q^3(2Al), Q^3(1Al), and Q^3(0Al) species decrease, and 2) the amounts of Q^2(1Al) and Q^2(0Al) species increase (Fig. 13). As the $MgO/(MgO+Na_2O$ ratio increases beyond 0.75, noticeable changes occur in the Q^4 species. Although the total amount of Q^4 species remains unaltered (Fig. 14), the following changes occur among the Q^4(mAl) species: 1) the amounts of the Al-rich Q^4 species (Q^4(3Al) & Q^4(4Al)) decrease, and 2) the quantity of the Al-poor Q^4 species (Q^4(1Al) & Q^4(2Al) increases. A slight increment in the amounts of highly depolymerized species (Q^1 and Q^0) is also visible toward the Mg endmember. This observation agrees with the XRD analysis, which indicated the existence of $MgSiO_4$ (having Q^0 species) in glass compositions close to the Mg endmember.

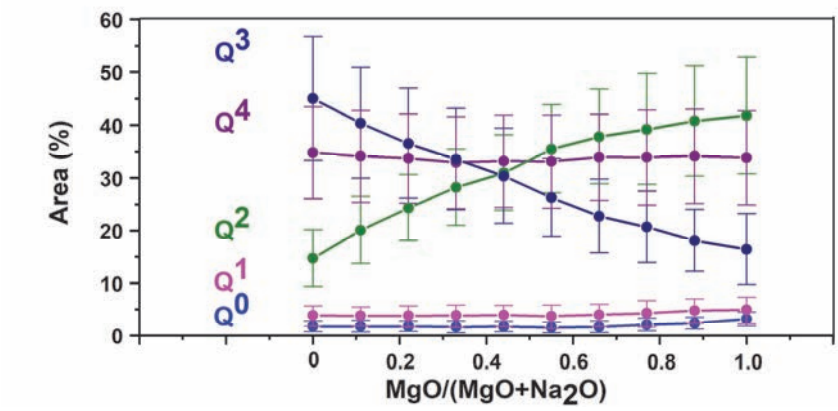

Fig. 12. Overview of Q^n speciation in (Na-Mg) aluminosilicate glasses (Reprinted [adapted] under CC BY 4.0 license from Publication I © 2020 Authors).

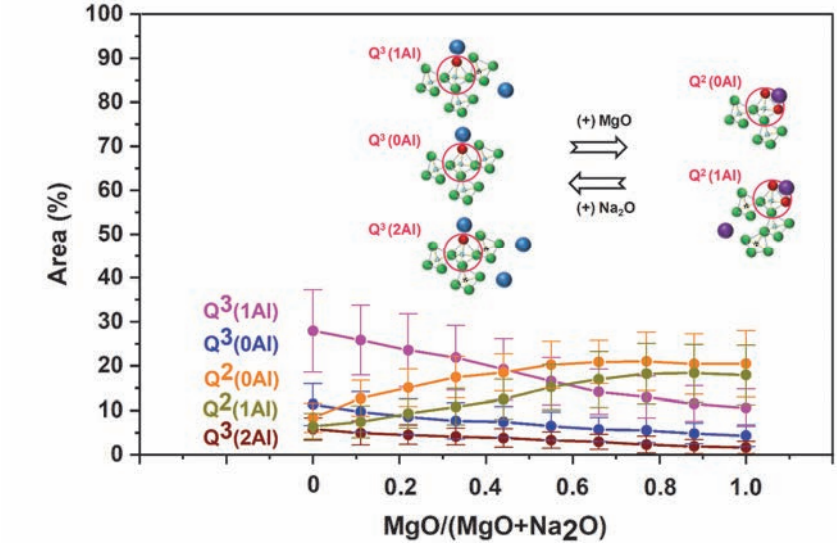

Fig. 13. Q^2 and Q^3 speciation in (Na-Mg) aluminosilicate glasses (Reprinted [adapted] under CC BY 4.0 license from Publication I © 2020 Authors).

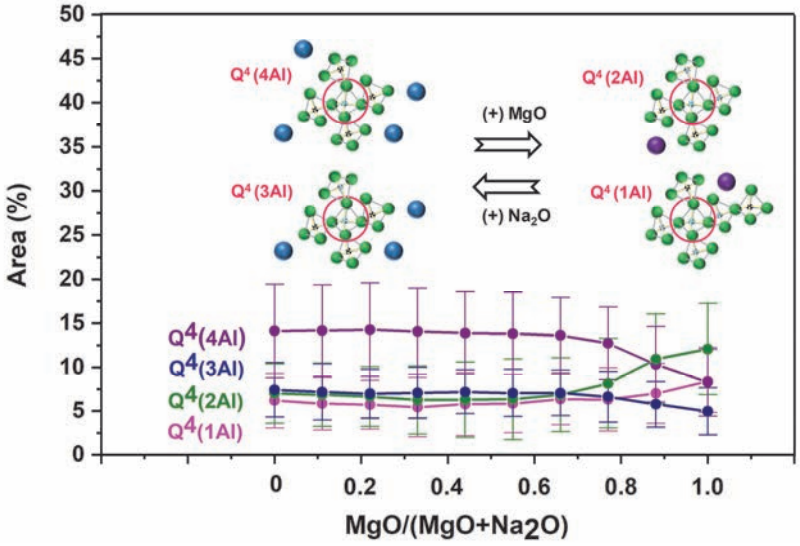

Fig. 14. Q^4 speciation in (Na-Mg) aluminosilicate glasses (Reprinted [adapted] under CC BY 4.0 license from Publication I © 2020 Authors).

The trends observed in the Q^n speciation of the studied glasses agree with observations in the previous studies reported in the literature. In our current study, the proportion of Q^2 species increased, while that of Q^3 species decreased, as Mg replaced Na in the glasses. Jones et al. [81] studied Na-Ca silicate glasses with the help of ^{29}Si MAS NMR spectroscopy and concluded that Na has a preference for Q^3 species, while Ca prefers the Q^2 species. Since the CFS is higher for Ca than for Na [35], the behavior of Ca in Na-Ca silicate glasses is similar to that of Mg in Na-Mg silicate glasses. Neuville et al. [82] performed Raman spectroscopic analysis of Na-Ca silicate glasses and observed that replacement of Ca with Na caused a reduction in the Q^3/Q^2 ratio. Schneider et al. [79] conducted a structural study of Na-Ca silicate glasses using ^{29}Si MAS NMR spectroscopy and observed that introduction of Na into the glasses led to a reduction in the proportion of Q^2 species, whereas the proportion of Q^3 species increased. Gambuzzi et al. [83] employed ^{29}Si and ^{27}Al MAS and MQMAS spectroscopies to study Na-Ca aluminosilicate glasses and observed that Na has a greater affinity for Q^4 and Q^3 species, while Ca prefers to associate with Q^2 and Q^1 species. Another observation made in the present study is that the amount of Al-rich Q^4 species (Q^4(3Al) & Q^4(4Al)) decreases, while the quantity of the Al-poor Q^4 species (Q^4(1Al) & Q^4(2Al)) increases, as Mg replaces

Na in the charge-compensator region (glass compositions close to Mg endmember). This agrees with previous studies in the literature on aluminosilicate glasses with similar Si:Al ratios. Mysen et al. [76] investigated the structure of Na aluminosilicate glasses employing ^{29}Si MAS NMR spectroscopy and observed that among $Q^4(m\text{Al})$ species, the proportions of Q^4(3Al) & Q^4(4Al) species were significantly higher when compared to the Q^4(0Al), Q^4(1Al), and Q^4(2Al) species. Lee and Stebbins [80] studied Ca aluminosilicate glasses by ^{29}Si MAS NMR spectroscopy and observed that $Q^4(m\text{Al})$ species were dominated by Q^4(1Al) and Q^4(2Al) species.

The connectivity of framework units is a significant structural feature of aluminosilicate glasses. It refers to the degree to which framework cations mix among themselves, and it can have significant effects on the properties of the aluminosilicate glasses [84]. Framework connectivity in the studied glasses can be understood by estimating the Al distribution in Q^n species; this can provide information regarding whether a specific Q^n species prefers to form Si-O-Si bonds or Si-O-Al bonds.

Estimation of the Al distribution in Q^n species (Fig. 15) indicated that Al prefers to associate with Q^4 species rather than with depolymerized Q^n species. Independent of the MgO/(MgO+Na_2O) ratio, all the aluminosilicate glasses showed an association of roughly 60% of total Al with Q^4 species. (Toward the Mg endmember, a slight decrease occurs in the proportion of Al associated with Q^4 species, which may be attributed to a reduction in Al-rich Q^4 species, as observed earlier). A significant proportion of Al is also associated with Q^3 and Q^2 species. In the case of the Na endmember, around 32% of the total Al resides with Q^3 species, while 8% of the total Al associates with Q^2 species. The distribution of Al in Q^2 and Q^3 species is influenced by the MgO/(MgO+Na_2O) ratio. The introduction of Mg into the glasses decreases the proportion of Al associated with Q^3 species, while increasing the proportion of Al confined to Q^2 species. In case of the Mg endmember, around 28% of the total Al associates with Q^2 species, while 13% of the total Al is confined to Q^3 species

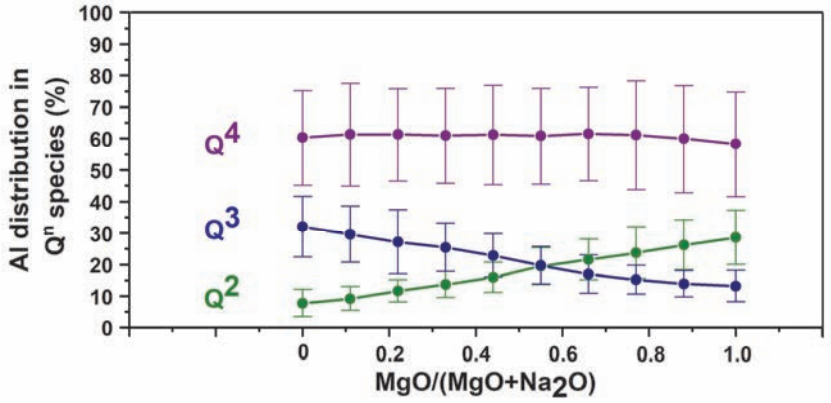

Fig. 15. Distribution of Al associated with various Q^n species (Reprinted [adapted] under CC BY 4.0 license from Publication I © 2020 Authors).

The preferential association of Al with Q^4 species (as mentioned above) agrees with previously reported studies. Gambuzzi et al. [83] employed ^{29}Si and ^{27}Al MAS and MQMAS spectroscopies to study Na-Ca aluminosilicate glasses and observed that Al has the following order for affinity for Q^n species: $Q^4 > Q^3 > Q^2$. Neuville et al. [85] conducted a structural study of Ca aluminosilicate glasses using XANES and ^{27}Al MQ-MAS spectroscopies and found that Al is mostly confined to Q^4 species. Mysen et al. [76] investigated the structure of Na aluminosilicate glasses using ^{29}Si MAS NMR spectroscopy and observed that roughly 70% of the Al is associated with Q^4 species. A number of structural studies on Na/Ca aluminosilicate glasses using Raman spectroscopy revealed an affinity of Al for Q^4 species [86], [87]. Alumina tetrahedra can associate with Q^4 species with a lower energy penalty (when compared to other Q^n species) for the following reasons: 1) bridging Al-O bonds are longer than bridging Si-O bonds, and 2) the average bond angles are larger in Si-O-Al than in Si-O-Si [76].

The trends observed in Q^n speciation obtained through ^{29}Si MAS NMR analysis can be explained theoretically by considering the CFS of the network-modifying cations. The proportion of Q^2 species increases, while that of Q^3 species decreases, as Mg replaces Na in the glasses. The negative charge densities are higher for Q^2 than for Q^3 species, as the former are associated with 2 NBO, while latter are associated with only 1 NBO. Therefore, Mg, with its higher CFS (when compared to Na), can more effectively stabilize Q^2 species. This leads to preferential association of Mg with Q^2 species. A similar mechanism can explain

the preferential association of Na with Q^3 species. Another observation in the current study is that the amount of Al-rich Q^4 species (Q^4(3Al) & Q^4(4Al)) decreases, while the quantity of the Al-poor Q^4 species (Q^4(1Al) & Q^4(2Al)) increases, as Mg replaces Na in the charge-compensator region (glass compositions close to the Mg endmember). The Q^4(3Al) and Q^4(4Al) sites (which associate with 1.5 and 2 units of Mg^{2+}, respectively) are subjected to greater distortion because of the higher CFS of Mg compared to the Q^4(1Al) and Q^4(2Al) sites (which associate with 0.5 and 1 units of Mg^{2+}, respectively). Hence, when Mg performs the role of a charge compensator, the Q^4(1Al) and Q^4(2Al) sites are more favored than the Q^4(3Al) and Q^4(4Al) sites.

4.1.5 XANES analysis of glasses

Insights into the local atomic order around Si atoms in glasses can be obtained from XANES. XANES spectra at the Si K-edge of the glasses (Fig. 16) indicate the presence of 5 major peaks: peaks A, B, C, D, and E. The peak positions and assignments corresponding to these peaks (shown in Table 4) are in agreement with the literature [88]–[91].

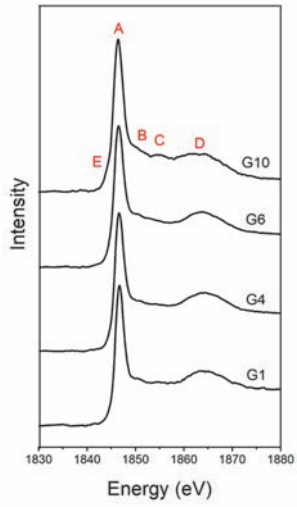

Fig. 16. Si K-edge XANES spectra of Na-Mg aluminosilicate glasses (Reprinted [adapted] under CC BY 4.0 license from Publication II © 2020 Authors).

Table 4. Peaks in Si XANES of Na-Mg aluminosilicate glasses

Peak label	Peak position	Peak assignment
A	≈ 1846 eV	Si 1s → t_2 states (Si 3p/3s)
B	≈ 1851 eV	multiple scattering
C	≈ 1855 eV	Si 1s → e states (Si 3d/3p)
D	≈ 1864 eV	Si 1s → t_2 states (Si 3d/3p)
E	≈ 1844 eV	Si 1s → a_1 states (Si 3s/3p)

Peak A represents the white line of X-rays, and the K-edge exists under it toward the lower energy side [91]. The peak A position (≈ 1846 eV) is attributed to tetrahedral Si in glasses [92]. Peak B is less predominant in all glasses except the Mg endmember. The intensity of peak B depends on the nature of network-modifying cation and is lower in Na silicate glasses than in Ca silicate glasses [91]. The intensity of peak C is higher in the Mg endmember than in the other glasses. Peak C is more profound when the network modifier in silicate glass is Ca rather than K/Na [91]. Peak D is a comparatively broad in nature, and its intensity has been correlated to the average Si-O-Si bond angle and Si-Si bond length [93], [94]. Hence, the broadening of peak D (Fig. 16) with the increase in Mg content of the glasses corresponds to a wider distribution in the bond angle and bond length. This agrees with the ^{29}Si MAS NMR analysis presented above, which showed an increase in the proportion of highly depolymerized silicate species (Q^0 and Q^1) towards the Mg endmember. Peak D also shifts to a lower energy with an increase in the Mg content of glasses. A similar shifting of peak D to lower energy was observed when Na was substituted by Ca in silicate glasses [91]. Peak E is more intense in the Mg endmember than in other glasses. The predominance of this peak may be attributed to bond mixing of the Si 3p and 3s orbitals [90].

The Si K-edge position was estimated by locating the local maxima in the 1st derivative of the XANES intensity with respect to energy (Fig. 17). As the Mg content of the glasses increases, the Si K-edge energy decreases. The Si K-edge position is known to shift to lower energies with increased depolymerization in glasses [91], [95]. This indicates that replacement of Na by Mg in glasses increases depolymerization, in agreement with the ^{29}Si MAS NMR analysis (which indicated an increase in the proportion of Q^2 species and a decrease in the proportion of Q^3 species as Na is replaced by Mg). The FWHM of the Si K-edge (Fig. 18) increases with a rise in the Mg content of the glasses and represents a higher structural disorder.

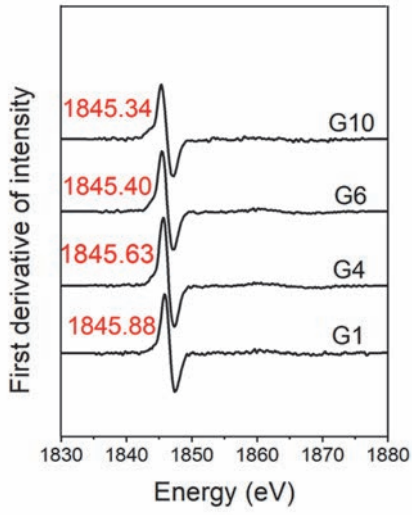

Fig. 17. Plot of the 1st derivative of Si XANES spectra of Na-Mg aluminosilicate glasses (Reprinted [adapted] under CC BY 4.0 license from Publication II © 2020 Authors).

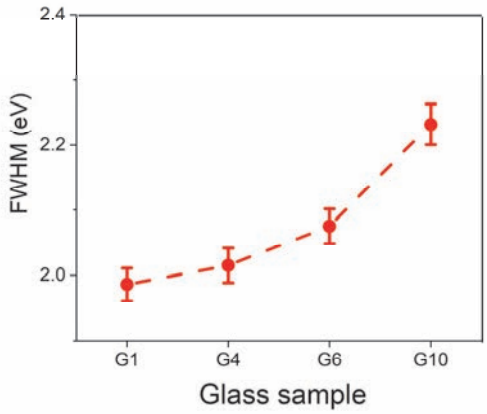

Fig. 18. FWHM of the Si K-edge of Na-Mg aluminosilicate glasses (Reprinted [adapted] under CC BY 4.0 license from Publication II © 2020 Authors).

The radial distance plot obtained from XANES is provided in Fig 19. The first intense shell corresponds mainly to the Si-O bond (≈1.6 Å), and partly to the Al-O bond (≈1.7 Å). The Mg-O bond (2.0 to 2.3 Å) may also contribute to this shell to a

minor extent. As the Mg content of the glasses increases: 1) the position of this shell shifts slightly to the right, which may be associated with increased depolymerization, and 2) the width of the shell also increases, indicating a wider bond length distribution and increased structural disorder. Being a light element, Si is a weak scatterer; hence, information about shells beyond the first shell is difficult to obtain.

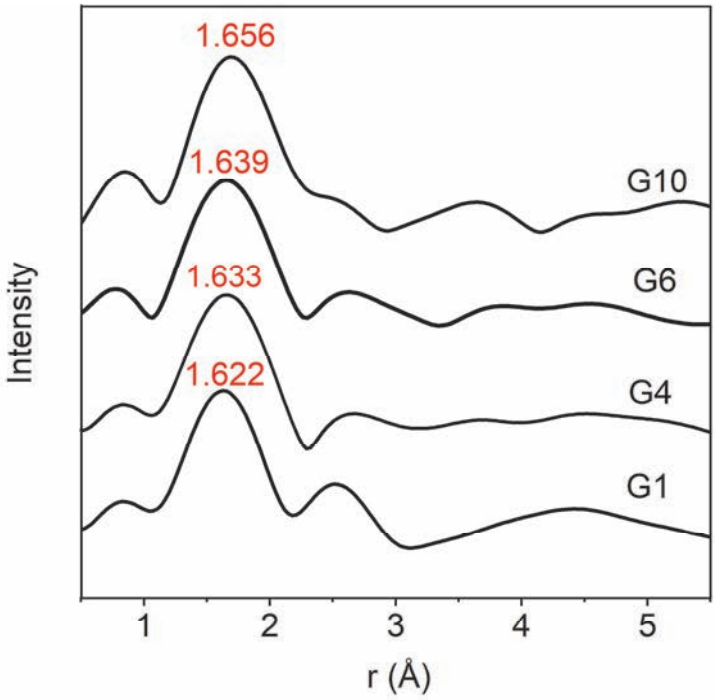

Fig. 19. Radial distance plot obtained from the XANES spectra of Na-Mg aluminosilicate glasses (Reprinted [adapted] under CC BY 4.0 license from Publication II © 2020 Authors).

4.2 Alkaline reactivity of Na-Mg aluminosilicate glasses

4.2.1 Si and Al alkaline solubility

The results of the alkaline solubility testing of Si are shown in Fig. 20. In the case of the Na endmember (f = 0, where f = MgO/[MgO+Na_2O], calculated as mole

fraction), the Si solubility observed is around 25%. An increase in the value of *f* increases the Si solubility until *f* = 0.33. The highest solubility (roughly 35%) is exhibited by the glass with *f* = 0.33. Increasing the value of *f* beyond 0.33 leads to a gradual reduction in solubility. The Mg endmember (*f* = 1) shows the lowest Si solubility (roughly 16%).

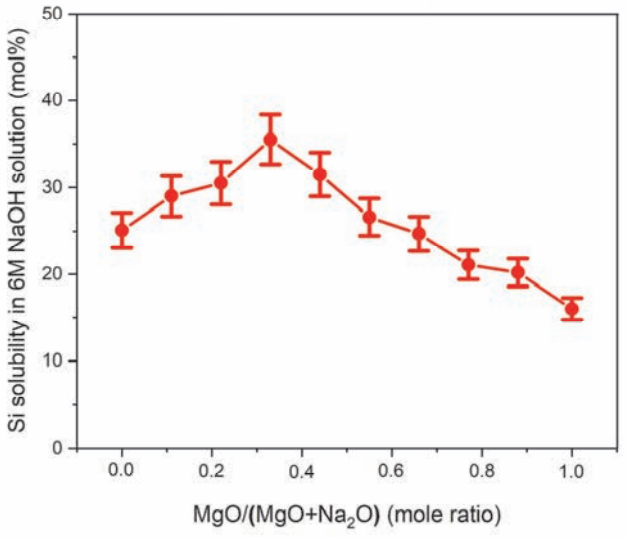

Fig. 20. Si alkaline solubility from Na-Mg aluminosilicate glasses (Reprinted [adapted] under CC BY 4.0 license from Publication II © 2020 Authors).

For the Na endmember (*f*= 0), the observed Al solubility is approximately 23% (Fig. 21). An increase in the value of *f* results in a solubility rise until *x* = 0.33. This trend in Al solubility is similar to that of the Si solubility; however, the proportional increase is lower than that of Si. The highest Al solubility (around 30%) is shown by a glass with *f* = 0.33. A further rise in the value of f results in a decrease in the Al solubility. This trend in Al solubility is similar to that of the Si solubility; however, the proportional decrease is higher than that of Si. The Mg endmember exhibits the lowest Al solubility, at around 6%. The reason for the differences in Al and Si solubilities is the occurrence of precipitation reactions, which will be discussed in upcoming sections (section 4.2.2, 4.2.3, and 4.2.4).

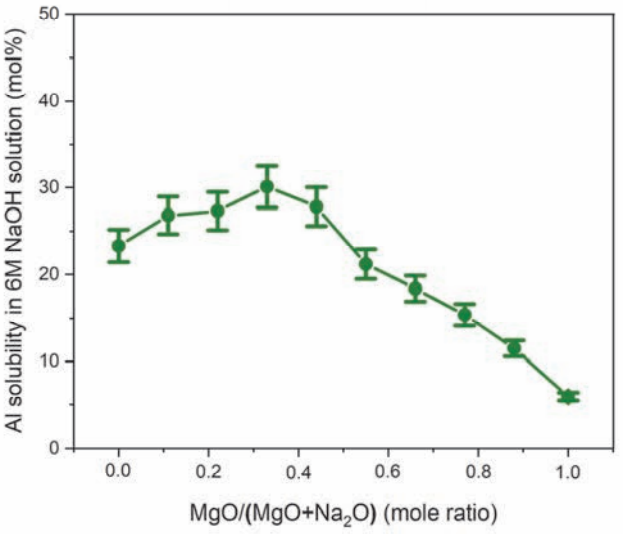

Fig. 21. Al alkaline solubility from Na-Mg aluminosilicate glasses (Reprinted [adapted] under CC BY 4.0 license from Publication II © 2020 Authors).

4.2.2 XRD analysis of solid residues

The XRD analysis of the glasses and the solid residues obtained after the alkaline dissolution of the glasses are shown in Fig. 22. The Na endmember (G1) is predominantly amorphous in nature, except for a minor crystalline Na carbonate (natrite, Na_2CO_3, PDF no: 04-011-4108) contribution. The solid residue (RG1) is exclusively amorphous, indicating that Na carbonate dissolves during the alkaline dissolution of glasses. The same trend is seen for the solid residues of glasses G2, G3, and G4. The solid residue (RG2) is mostly amorphous, except for a minor crystalline hydrotalcite-group phase (quintinite, $Mg_{0.67}Al_{0.33}(CO_3)_{0.17}(OH)_2(H_2O)_{0.5}$, PDF No: 04-015-4253). This indicates that a portion of the soluble Al is precipitated as hydrotalcite. A similar trend is observed in the case of the solid residues of all glasses from G3 to G10. The intensity of hydrotalcite increases as the Mg content of the glasses rises. The formation of hydrotalcite as a precipitation product can explain the reduced Al solubility (in comparison to Si solubility) observed earlier (Fig. 20 and 21). Reflections of forsterite (Mg_2SiO_4, PDF no: 04-

007-7321) observed in G9 are retained in the solid residue RG9. This indicates the high resistance of forsterite to alkaline dissolution.

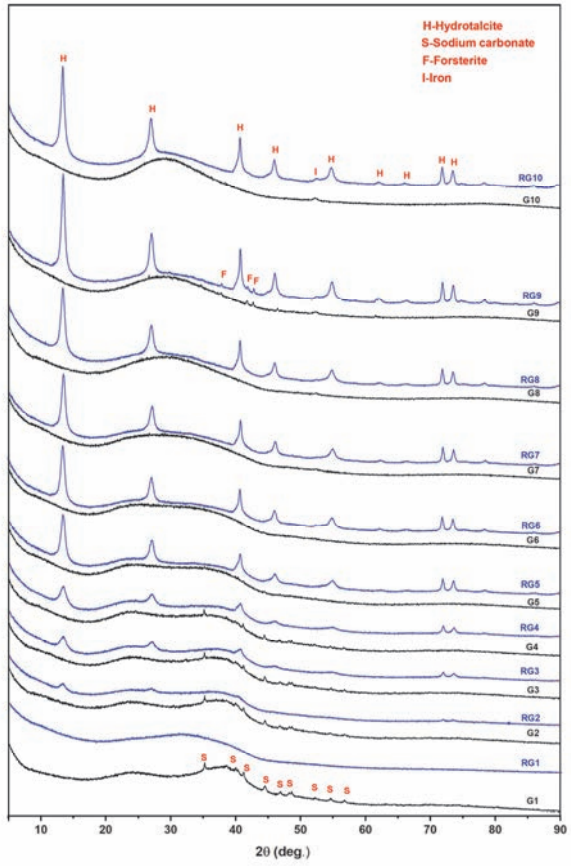

Fig. 22. XRD characterization of the glasses (represented as Gx), and the solid residues (represented as RGx) obtained after alkaline dissolution (Reprinted [adapted] under CC BY 4.0 license from Publication II © 2020 Authors).

4.2.3 TEM analysis of solid residues

The STEM images and elemental maps for glasses and the solid residues are shown in Fig. 23. The Na endmember (G1) has irregular glass particles with homogenous Si and Al distributions. However, Na is non-homogenously distributed, and the

areas having high Na concentration correspond to Na carbonate, in agreement with the previous XRD analysis (Fig. 22). The solid residue (RG1) has smooth corroded glass particles without any precipitated products. The residue also shows areas with high Na concentration, which could be due to Na carbonate, although this Na carbonate was not detected in the XRD analysis of RG1 (Fig. 22). The glass sample G5 consists of irregular glass particles with homogenous distributions of Na, Si, and Al. The solid residue (RG5) has corroded glass particles, together with precipitated products. These precipitated products are richer in Mg and Al and have no noticeable contributions of Na and Si. This observation agrees with the XRD analysis of RG5, which detected a hydrotalcite-group phase. The explanation given for the G5-to-RG5 transformation also holds for the G10-to-RG10 transformation, except that the latter has more hydrotalcite-group phase. This agrees with the XRD characterization, which revealed higher formation of the hydrotalcite-group phase with increases in the Mg content of the glasses.

4.2.4 ^{27}Al MAS NMR analysis of residues.

The ^{27}Al MAS NMR spectral analysis of residues is provided in Fig. 24. The spectrum of RG4 exhibits a broad band (centered at ≈ 55 ppm) that spans from 20 ppm to 70 ppm. This band is attributed to the unreacted glass precursor. The spectrum additionally exhibits a sharp Al^{VI} band (at ≈ 8.2 ppm) pertaining to the hydrotalcite phase [96], whose presence was also confirmed in the XRD analysis of RG4 (Fig. 22). This band becomes more intense on moving from RG4 to RG10, implying greater formation of hydrotalcite, which corroborates the XRD analysis. None of the residue spectra provided evidence for the existence of any precipitated aluminosilicate product, as the formation of an aluminosilicate product would have resulted in sharper Al^{IV} bands. This corroborates the TEM analysis (Fig. 23) and XRD analysis (Fig. 22) of the residues.

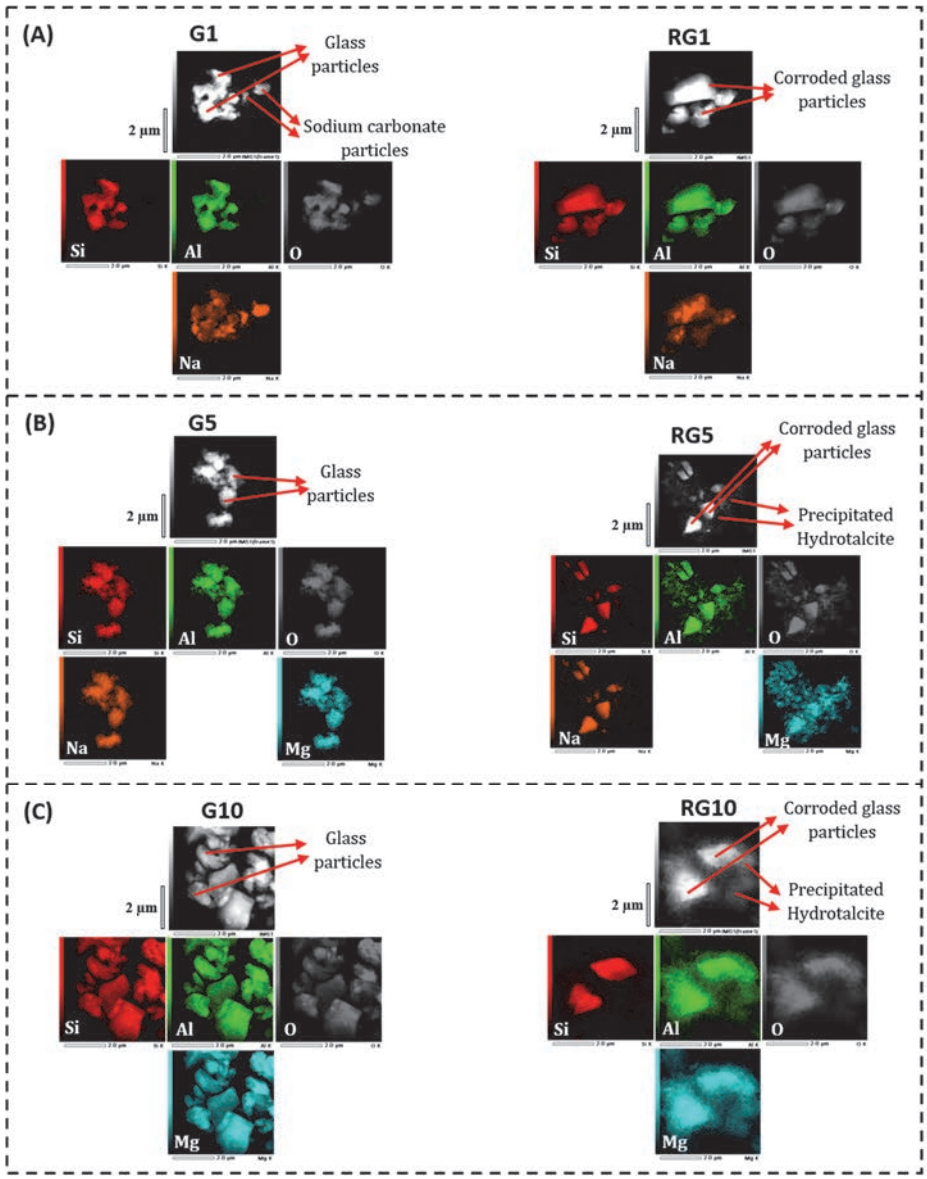

Fig. 23. STEM images and elemental maps for the glasses *(*represented as Gx), and the solid residues (represented as RGx) obtained after alkaline dissolution (Reprinted [adapted] under CC BY 4.0 license from Publication II © 2020 Authors).

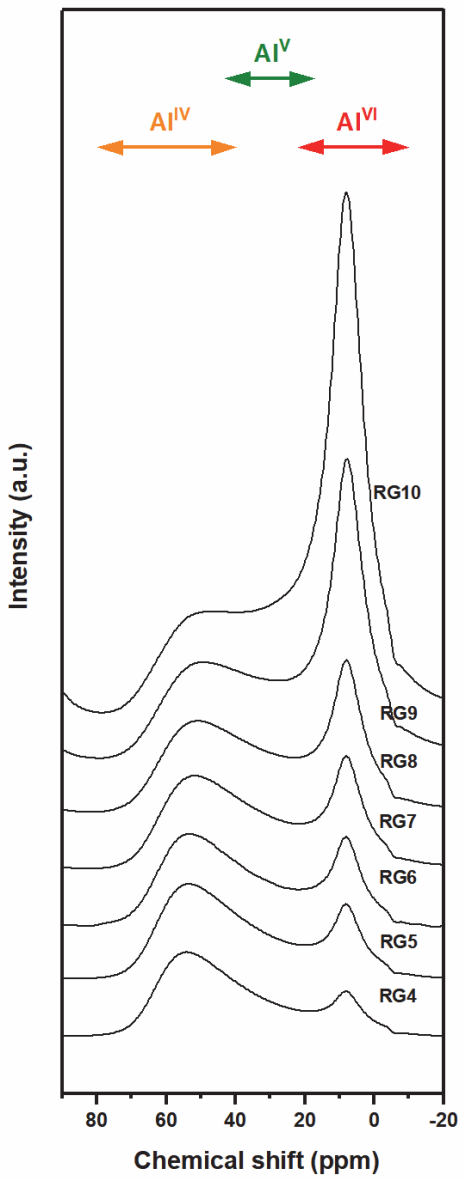

Fig. 24. ^{27}Al MAS NMR analysis of the residues obtained from alkaline dissolution of Na-Mg aluminosilicate glasses (Reprinted [adapted] under CC BY 4.0 license from Publication III © 2021 Authors).

4.2.5 Further discussion on reactivity

The STEM, ^{27}Al MAS NMR, and XRD characterizations of the solid residues revealed that a portion of the dissolved Al forms precipitated products. Hence, the dissolved concentrations of Al (Fig. 21) do not indicate the true reactivity of the glasses. Conversely, no noticeable contribution is evident for Si in the precipitate formation. Hence, the solubility of Si (as estimated in Fig. 20) may be used to represent the true reactivity of the glasses under the experimental conditions applied here.

The Si solubility analysis (Fig. 20) reveals the following trend in glass reactivity: An increase in Mg content of the glasses causes an initial increase in the reactivity of glasses until a maximum is attained for f = 0.33, after which the reactivity drops. The traditional parameters for estimating glass reactivity (optical basicity and NBO/T) cannot explain the observed trend in glass reactivity. A plot of optical basicity and NBO/T of the glasses is shown in Fig. 25. Since NBO/T is the same for all the glasses, the glasses should exhibit similar reactivities, but this contradicts the experimentally determined glass reactivities. Another flaw in using NBO/T for estimating reactivity is evidenced by the XRD characterization of G9 and RG9, as forsterite (Mg_2SiO_4), which is originally present in G9, is retained in RG9 after alkali dissolution, thereby demonstrating its resistance to alkaline attack. Forsterite is a nesosilicate mineral and has the highest feasible NBO/T value (4) for any silicate; hence, it should exhibit high reactivity according to this analogy. The resistance of forsterite to alkaline dissolution therefore indicates a flaw in using NBO/T for estimating reactivity. Note that NBO/T, in general, is a good parameter for estimating the glass reactivity in specific glassy materials. However, in the current study, NBO/T performs poorly, and one reason could be that forsterite is crystalline. Crystalline compositions exhibit lower reactivity than their glassy counterparts [97].

The other traditional parameter for estimating glass, optical basicity, also does not explain the glass reactivity trend completely. Replacement of Na by Mg leads to a reduction in optical basicity (Fig. 25), indicating that glass reactivity should drop with the introduction of Mg. This may probably explain the reduction in glass reactivity after the maximum value (of glass reactivity); however, it cannot explain the initial rise in reactivity of the glasses (before the maximum value of glass reactivity is achieved).

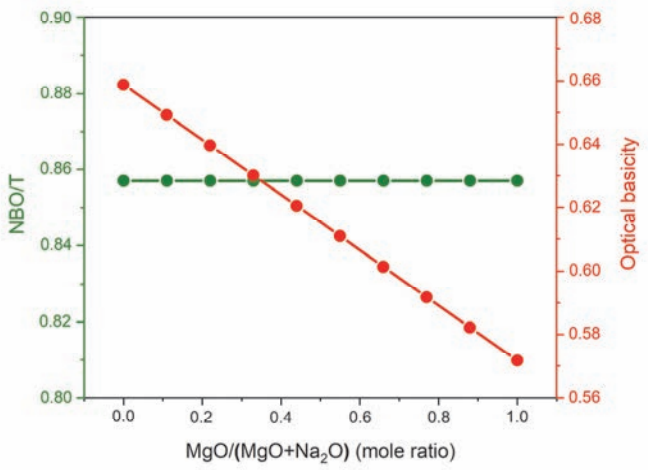

Fig. 25. Plot of optical basicity and NBO/T of the aluminosilicate glasses (Reprinted [adapted] under CC BY 4.0 license from Publication II © 2020 Authors).

While elucidating the reactivity of the glasses, the structural aspects deserve due attention, apart from the traditional parameters for estimating glass reactivity (NBO/T and optical basicity). The ^{29}Si MAS NMR analysis (section 4.1.4) of the glasses indicated an increased depolymerization upon introduction of Mg (the proportion of Q^2 species increased, while the proportion of Q^3 species decreased, as Na is replaced by Mg). As the depolymerization of glass increases, the reactivity of glass will also increase. The glass reactivity (as observed in this study) is influenced by two factors: optical basicity and depolymerization of the glasses. During the initial replacement of Na by Mg, the influence of glass depolymerization dominates over the impact of optical basicity, leading to a rise in glass reactivity. However, at the later stages of Na replacement by Mg, the impact of optical basicity dominates over the influence of glass depolymerization, leading to a drop in glass reactivity.

The glass reactivity studies in this work deal with the effects on chemical durability (lower chemical durability represents higher glass reactivity) during the substitution of one network modifier in the glass by another network modifier. During the network modifier replacement in silicate glasses, the properties of the glasses vary in a non-linear fashion, and this phenomenon has been assumed to be due to a mixed-modifier cation effect (MMCE) [98]. Some ambiguity exists in the

literature on studies concerning the impact of MMCE on chemical durability. Studies by Bunker et al. [99] and Smets et al. [100] reported that the MMCE has no influence on the chemical durability in silicate glasses. By contrast, investigations by Day [101] and Zhifang et al. [102] revealed an influence of MMCE on the chemical durability. Their studies showed that network modifier replacement in silicate glasses initially increases the chemical durability, but the chemical durability decreases during the later replacement stages. This does not agree with our observations in the present study, as Na replacement by Mg led to an initial decrease in chemical durability but an increase in chemical durability during the later replacement stages. Note also that most of the literature studies on the effect of MMCE were performed on silicate systems without Al or with low Al. Zhifang et al. [102] reported that the impact of MMCE on chemical durability became insignificant in Ca/Na/K silicate glasses when a small portion of Si was substituted by Al . The ambiguity in the literature studies concerning the impact of MMCE on chemical durability could reflect the fact that the structural study of the glasses was not given due attention while estimating their chemical durability.

4.3 The fate of Mg in AAMs prepared from Na-Mg aluminosilicate glasses

4.3.1 Compressive strength analysis of AAMs

The compressive strength of AG1, the AAM prepared from the Na endmember of the glasses, is around 13 MPa (Fig. 26). With a rise in the Mg content of the glasses, the following trend is observed in the compressive strength of AAMs prepared from them: the compressive strength rises initially, reaches a maximum value of 25 MPa (in AG3), and then drops and dips to its lowest value of around 3 MPa in AG10. This trend in compressive strength roughly follows the trend observed in the alkaline reactivity of the glasses (section 4.2.5).

The samples remaining after performing the compressive strength measurement were ground to obtain powders for further analysis. Despite rigorous milling, three samples (AG3, AG2, and AG1) were not transformed into powdered form and instead formed sticky materials, perhaps due to the presence of large quantities of Na in those samples. Cryogenic milling was also performed for these samples, but they still failed to form powdered samples. Hence, these three AAMs could not be subjected to characterization by NMR, TG-MS, XRD, or SEM.

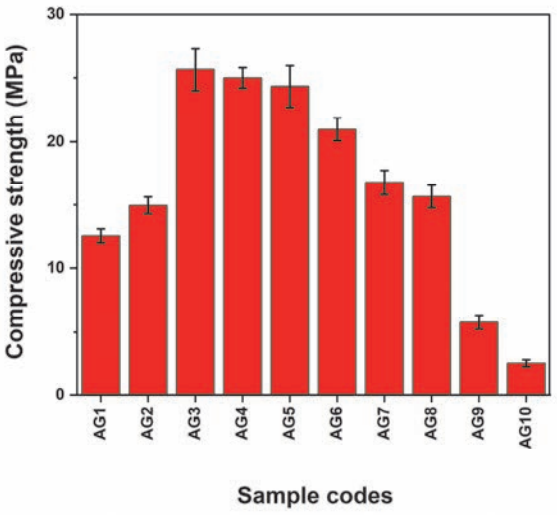

Fig. 26. Results of the compressive strength analysis of AAMs (Reprinted [adapted] under CC BY 4.0 license from Publication III © 2021 Authors).

4.3.2 XRD analysis of AAMs

The XRD characterization of the AAMs (Fig. 27) revealed LSX zeolite (LSX_1, $Na_{96}Al_{96}Si_{96}O_{384}\cdot(H_2O)_{384.3}$; PDF # 01-074-2534) as the main crystalline phase in AG4. The sample also contains the following: 1) small proportions of other zeolites, such as ZSM-11 ($Na_8Al_8Si_{40}O_{96}\cdot(H_2O)_8$; PDF # 04-018-2360) and natrolite ($Na_2Al_2Si_3O_{10}\cdot(H_2O)_2$; PDF # 00-022-1224), and 2) large proportions of thermonatrite ($Na_2CO_3\cdot H_2O$; PDF # 01-070-2148), which could be formed due to exposure of excess Na (present in the sample) to atmospheric CO_2. The sample AG5, like AG4, also has predominant crystalline contributions from LSX zeolite (LSX_1), but it also has thermonatrite and a small contribution from another LSX zeolite (LSX_2; $Na_{23}Al_{23}Si_{25}O_{96}\cdot(H_2O)_x$, PDF # 04-009-8639). In all the other AAMs (AG6 to A1G0), the predominant crystalline phase is garronite zeolite ($Na_4Al_4Si_4O_{16}\cdot(H_2O)_{7.6}$; PDF # 04-011-7946), with some thermonatrite, whose contribution declines with decreasing Na content in AAMs and almost disappears in the case of AG10. The sample AG9 retains the reflections of forsterite from the precursor glass G9 (Fig. 22), confirming the inertness of forsterite toward alkaline dissolution. A few samples show contributions from Fe; this is due to Fe contamination present in the corresponding precursors glasses/contamination originating from milling of AAMs in the disc mill.

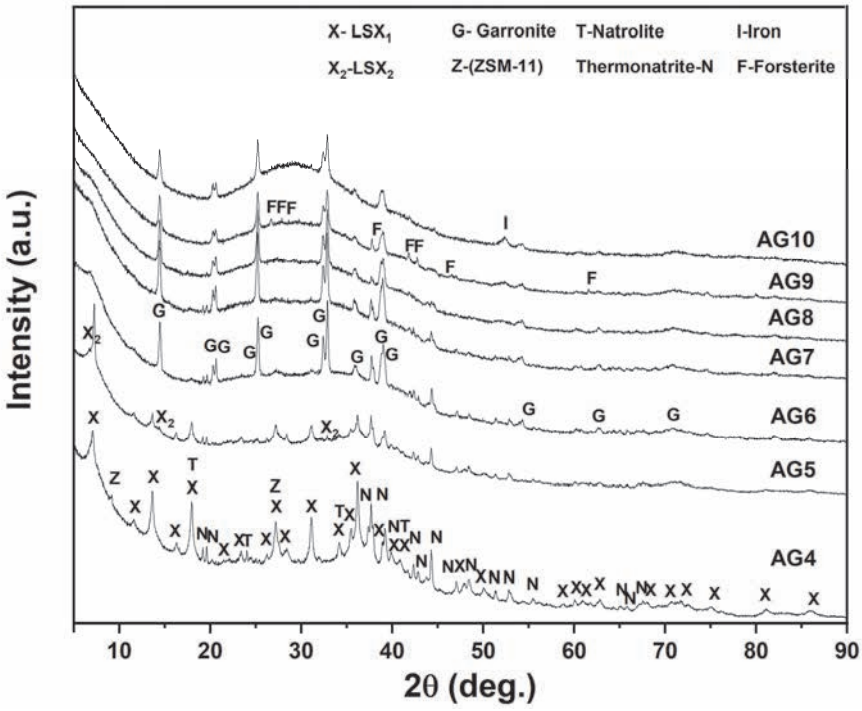

Fig. 27. XRD characterization of AAMS prepared from Na-Mg aluminosilicate glasses (Reprinted [adapted] under CC BY 4.0 license from Publication III © 2021 Authors).

The XRD characterization of AAMs (Fig. 27) provided no information regarding the state of Mg in AAMs. None of the AAMs exhibited XRD reflections pertaining to any crystalline Mg-containing phases, such as a hydrotalcite group, the most commonly reported fate of Mg in AAMs with significant Mg content. No formation of partially amorphous phases, such as M-S-H phases, is indicated in these AAMs. The XRD pattern of the M-S-H phases has characteristic broad peaks at 20°, 26°, 36°, and 61°, 2θ when the XRD analysis is performed with Cu radiation [17], [103]; however, as the current XRD study was performed with Co radiation, the formation of the M-S-H phase should produce broad peaks at 23°, 30°, 42°, and 71°. No broad peaks are present at the mentioned 2θ in any of the AAMs. This indicates that no M-S-H phase is formed in these AAMs. This agrees with the findings of Walling et al. [28], who also investigated AAMs in the Na_2O-MgO-Al_2O_3 -SiO_2-H_2O and

found no evidence for the formation of a M-S-H phase when blends containing $Mg(OH)_2$, SiO_2 and $NaAlO_2$ were cured at elevated temperature for 2 years.

Although no Mg-containing phase was detected in any of the AAMs synthesized from Na-Mg aluminosilicate glasses (Fig. 27), the XRD characterization of residues (Fig. 22) obtained after the alkaline dissolution (at a high L/S (liquid to solid) ratio of 40) of the same glasses indicated the formation of a hydrotalcite-group phase (quintinite; $Mg_{0.67}Al_{0.33}(CO_3)_{0.17}(OH)_2(H_2O)_{0.5}$; PDF # 04-015-4253). The aforementioned characterization by XRD, TEM, and ^{27}Al MAS NMR (sections 4.4.2, 4.2.3, and 4.2.4) of the residues revealed hydrotalcite as the sole precipitating phase and no noticeable contribution of Si toward precipitate formation; this is due to the high alkaline solubility of Si and the high L/S used in the experiment.

Combining the XRD analysis of AAMs (Fig. 27) and the characterization analysis of solid residues (Fig. 22, Fig. 23, and Fig. 24) from alkaline dissolution of glasses, the following conclusions can be drawn. The alkalinity (6 M NaOH) of the solution used for preparing AAMs is the same as that used for alkaline dissolution experiments; however, the L/S employed during the preparation of AAMs is 0.35, which is less than $1/100^{th}$ of the L/S employed during the alkali dissolution test. During the preparation of AAMs, the low L/S results in supersaturation of Mg, Al, and Si with respect to both the hydrotalcite phases and zeolite. In this situation, Al can be integrated into either hydrotalcite phases or zeolite, meaning that both hydrotalcite formation and zeolite formation can compete for Al integration. Apparently, under the studied conditions, the kinetics favor the formation of zeolites, and Al preferentially precipitates with Si to produce zeolites rather than integrating with Mg to produce hydrotalcite phases. By analyzing the chemical compositions of major zeolite phases in AAMs and those of precursor glasses used in the AAM synthesis, the following conclusions can be made. All the glasses have a Si:Al ratio of 2.5. However, the Si:Al ratio of the major zeolite phases (garronite and LSX) present in the AAMs is 1. This indicates that Al will act as the limiting reactant during the production of zeolites from these glasses. Hence, all the Al is utilized to produce zeolites, leaving no Al available to produce hydrotalcite. In conclusion, a hydrotalcite phase is not formed in AAMs since the kinetics favor zeolite rather than hydrotalcite phases, and this consumes all the Al at the same rate as it becomes dissolved from the glasses.

The preferential integration of Al into zeolites rather than hydrotalcite phases, as revealed by this work, may explain why no hydrotalcite phase was detected in some of the previous literature that reported AAMs with significant Mg content

(Table 1). Walling et al. [26] activated blends of $Mg(OH)_2$ and SiO_2 with $NaAlO_2$ and observed no hydrotalcite phase when Si:Al was high, whereas a hydrotalcite phase was detected in case of a blend with low Si:Al. Zeolites formed the major product in all the AAMs, and their Si:Al varied from 1.00 to 1.67. Those authors found no hydrotalcite phase formation in the case of precursor blends having Si:Al in the range of 1.00 to 1.67 (i.e., without any noticeable excess of Al [which would be available after producing zeolite] for reaction with $Mg(OH)_2$ to produce hydrotalcite). This can explain the absence of hydrotalcite phases in AAMs prepared from those precursor blends. The only precursor blend that produced a hydrotalcite phase in that study had a Si:Al ratio of 0.67. This precursor blend evidently contained a large excess of Al (available after producing zeolite), which reacted with $Mg(OH)_2$ to produce hydrotalcite.

Kinnunen et al. [30] synthesized AAM from a stone wool + fly ash mixture using an activation solution consisting of a NaOH + $NaAlO_2$ mixture (the MgO content of their systems varied from 9.2 to 12.2 wt.%). No hydrotalcite phase was detected in any of the AAMs. Those authors also observed that, in addition to the main C-A-S-H phase, the AAMs possessed a large proportion of zeolite ($Na_8(AlSiO_4)_6(OH)_2 \cdot H_2O$), which could explain why no hydrotalcite phase was detected. Zhang et al. [31] prepared AAMs from BFS through sodium silicate activation and observed no hydrotalcite phases in the AAMs (the MgO content of BFS was 9.3 wt.%). Those authors found that, in addition to the main C-A-S-H phases, the AAMs contained many crystalline aluminosilicate phases, such as zoisite, wairakaite, and natrolite. The existence of the many crystalline aluminosilicate phases in these AAMs probably explains why no hydrotalcite phase was formed.

4.3.3 ^{27}Al MAS NMR spectral analysis of samples

The ^{27}Al MAS NMR spectra of Na-Mg aluminosilicate glasses are provided in Fig. 27. In the case of G4, the spectrum has a broad band (with the maximum at approximately 55 pm) that extends from 0 ppm to 70 ppm. This corresponds mainly to the tetrahedrally coordinated aluminum (Al^{IV}) in the aluminosilicate glasses [104]. A rise in Mg content of the glasses broadens this band because the high charge density of the Mg cation (compared to Na) can produce a greater distortion in the local aluminum environment [42].

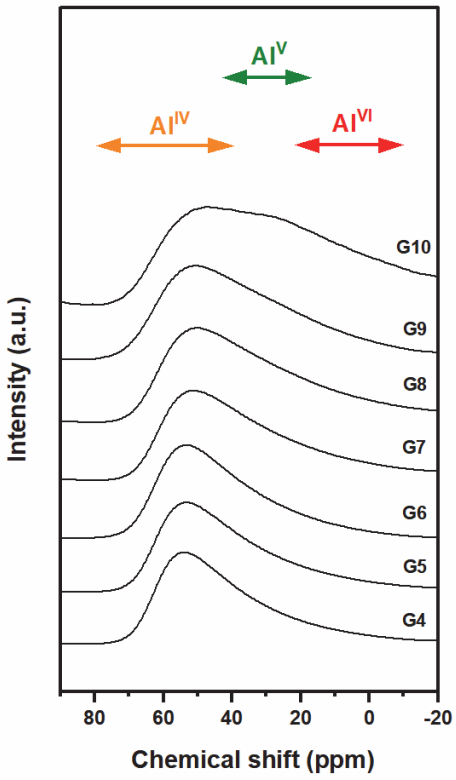

Fig. 28. ^{27}Al MAS NMR analysis of Na-Mg aluminosilicate glasses (Reprinted [adapted] under CC BY 4.0 license from Publication III © 2021 Authors).

The ^{27}Al MAS NMR spectra of AAMs are provided in Fig. 29. The band is narrower in AG4 than in its precursor G4, with a maximum at approximately 58 ppm (in the case of G4, the maximum was at approximately 55 ppm). This band corresponds to the Al^{IV} in zeolitic phases [105], as revealed in the XRD characterization (Fig. 27). No noticeable band is present in the octahedral region in the spectrum of AG4, which implies the absence of hydrotalcite phases. This agrees with the XRD pattern of AG4 (Fig. 27), which showed no reflections pertaining to hydrotalcite. As the Mg content of AAMs increases (from AG4 to AG10), the signal band broadens, corresponding to the reduction in reactivity of glasses with the rise in Mg content (from G4 to G10). This trend agrees with the trends observed in compressive strength (Fig. 26), and in the reactivity of glasses (section 4.2.5). A

minor broad Al^{VI} band (centered at approximately 7 ppm) develops slowly in the spectra of glasses as the Mg content of AAMs increases (from AG4 to AG10). This band corresponds to the unreacted glass precursor remaining in the AAMs. Note that none of the spectra of the AAMs provide evidence for the existence of hydrotalcite phases, as the formation of hydrotalcite should result in the appearance of a sharper Al^{VI} band [77].

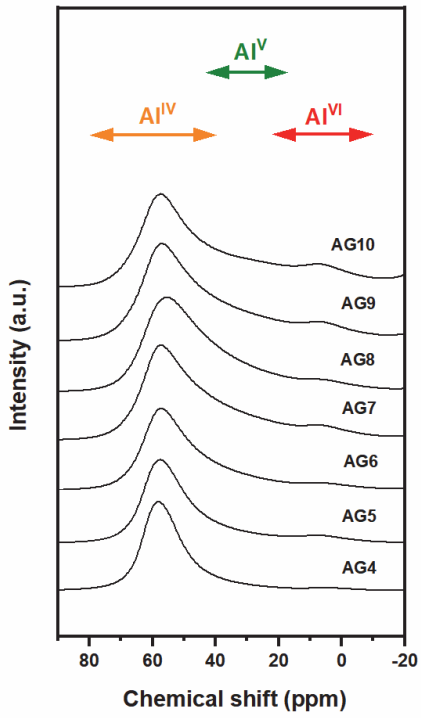

Fig. 29. ^{27}Al MAS NMR analysis of the AAMs (Reprinted [adapted] under CC BY 4.0 license from Publication III © 2021 Authors).

4.3.4 ^{29}Si MAS NMR spectral analysis of the samples

The ^{29}Si MAS NMR spectra obtained for the AAMs were subjected to deconvolution to obtain Gaussian components corresponding to different $Q^n(m\text{Al})$ species. Microsoft Excel was used for the deconvolution process essentially as in previous studies [15], [106]. The deconvolution process involved the following: 1)

a minimum number of Gaussian components were included to describe the original spectrum in a credible manner; 2) the FWHM for all Gaussian components was restricted to values less than 10 ppm; 3) chemical shift values for specific $Q^n(m\text{Al})$ species were decided by consulting a number of previous literature studies [25], [77], [78], [105]; 4) unreacted glass precursors (present in AAMs) were rescaled essentially as described in a previous study [106]; and 5) six Gaussian components corresponding to different $Q^n(m\text{Al})$ species in product components of AAMs were considered and their FWHM and chemical shift values are shown in Table 5. The spectral deconvolutions in the cases of AG4 and AG10 are provided in Fig. 30 and 31 as examples.

Table 5. The FWHM and chemical shift values used during the deconvolution process of the ^{29}Si MAS NMR spectra obtained for AAMs (Reprinted [adapted] under CC BY 4.0 license from Supporting Information of Publication III © 2021 Authors).

Component	Q^0	Q^1(0Al)	Q^2(1Al)	Q^2(0Al)	Q^4(4Al) or Q^3(1Al)	Q^4(3Al) or Q^3(0Al)
Chemical shift (ppm)	-70.5(±0.1)	-77.0(±0.2)	-80.0(±0.1)	-83.0(±0.1)	-85.0(±0.1)	-90(±0.5)
FWHM (ppm)	6.5 (±0.1)	5.8(±0.1)	5.0(±0.1)	5.0(±0.1)	5.8(±0.7)	7.2(±0.1)

The $Q^n(m\text{Al})$ speciation in the binding phase of the AAMs is provided in Fig. 32. The sample AG4 possesses the highest amount of extremely depolymerized silicate species (amount of $Q^{0-2}(m\text{Al})$ species ≈ 63%). On moving from AG4 to AG10, the amount of these species is reduced and dips to a minimum in AG10 (amount of $Q^{0-2}(m\text{Al})$ species ≈ 13%). The sample AG4 possesses the lowest amount of the most-polymerized silicate species (quantity of Q^{3-4}(mAl) species ≈ 40%). On moving from AG4 to AG10, the amount of these species increases and attains a maximum in case of AG10 (87%). The Q^4(3Al) and Q^4(4Al) species existing in the system correspond to the zeolites observed during the XRD characterization of the AAMs (Fig. 27).

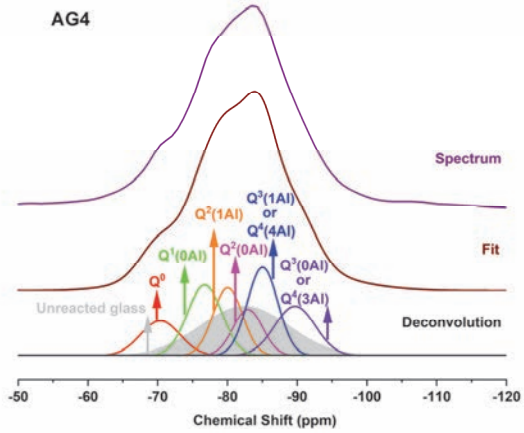

Fig. 30. Deconvolution of ^{29}Si MAS NMR spectrum of AG4 (Reprinted [adapted] under CC BY 4.0 license from Publication III © 2021 Authors).

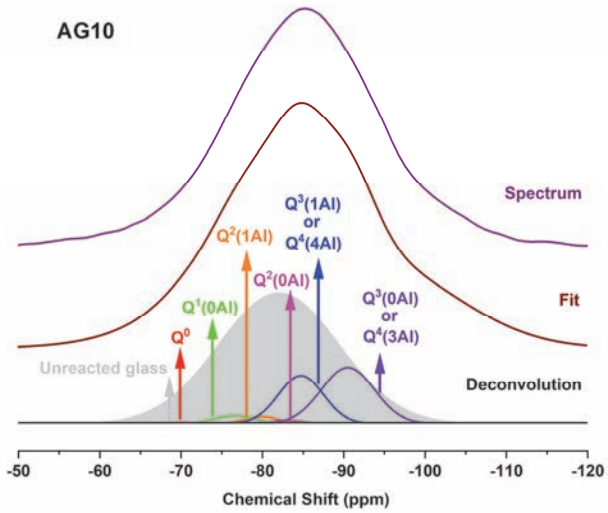

Fig. 31. Deconvolution of ^{29}Si MAS NMR spectrum of AG10 (Reprinted [adapted] under CC BY 4.0 license from Publication III © 2021 Authors).

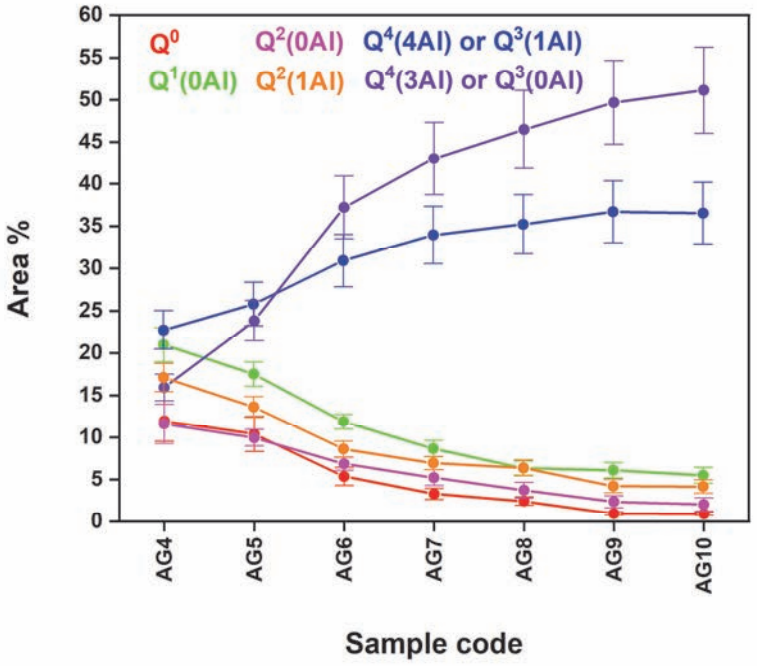

Fig. 32. Q^n speciation in the product phase of AAMs according to the ^{29}Si MAS NMR spectral analysis (Reprinted [adapted] under CC BY 4.0 license from Publication III © 2021 Authors).

The ^{29}Si NMR MAS spectral analysis provides evidence for the absence of the M-S-H phase in AAMs. The formation of an M-S-H phase would be expected to result in the appearance of characteristic resonances (attributed to Q^3 species) between -92.4 and -97.7 ppm, and, depending on the Mg/Si ratio, these resonances would contribute around 40–70% of the overall Q^n relative peak intensities pertaining to the M-S-H phase [107]. However, in the current study, the most negative chemical shift value obtained satisfactorily is -90.0 ppm. This implies that the AAMs do not contain the conventional M-S-H phase. This corroborates the XRD characterization of AAMs, which did not indicate any of the characteristic reflections of an M-S-H phase (Fig. 27). The $^{29}Si\{^1H\}$ CP/MAS NMR spectral analysis of AAMs also indicated the absence of an M-S-H phase (results are provided in the supporting information of the published work by the author (Publication III).

4.3.5 SEM analysis of AAMs

The SEM-EDS characterization of AG4 is provided in Fig. 33. Certain areas of interest are represented with labels. Areas m1 and m2 correspond to the unreacted glass precursors. The rims (r_{m1} and r_{m2}) around m1 and m2 are enriched with Mg, Si, and O and correspond to a Mg silicate phase that is apparently formed in the alteration layers on the surface of the glass particles. Characterization of the AAMs by ^{29}Si MAS NMR (section 4.3.4) and XRD (section 4.3.2) did not reveal any evidence for the presence of crystalline Mg silicate or M-S-H phases in the AAMs. Therefore, the rim areas (represented by r_{m1} and r_{m2}) are composed of an amorphous Mg silicate (AMS) phase. The areas labeled n1, n2, and n3 are enriched in Na and Al and possess Si and O. These areas correspond to the zeolites, in agreement with the XRD analysis (Fig. 27) and ^{29}Si MAS NMR analysis (section 4.3.4). The rims (r_{n1} $r_{n2,}$ and r_{n3}) that exist around the zeolites are enriched in Si, Mg, and O. These areas correspond to the AMS phase.

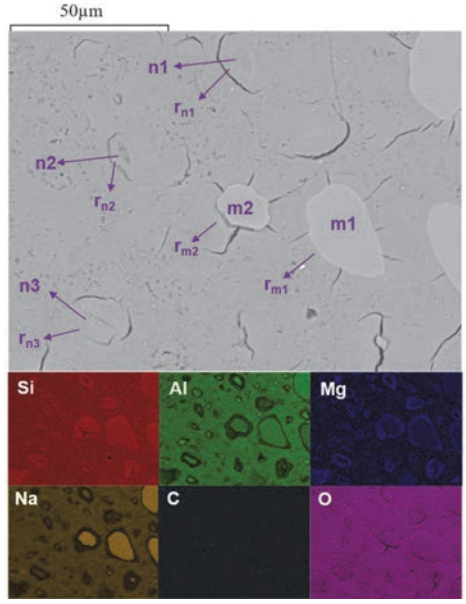

Fig. 33. SEM (low magnification) characterization of AG4 (Reprinted [adapted] under CC BY 4.0 license from Publication III © 2021 Authors).

The SEM-EDS characterization of AG4 conducted at higher magnification is provided in Fig. 34. The areas identified with lower magnification (Fig. 33) can be

seen in this figure with more clarity. The AMS phase, besides forming rims around unreacted glass and zeolite, also occurs as individual areas, as represented by z1. Other areas, such as y1 and y2, are enriched with C, Na, and O and correspond to the thermonatrite detected during XRD analysis (Fig. 27).

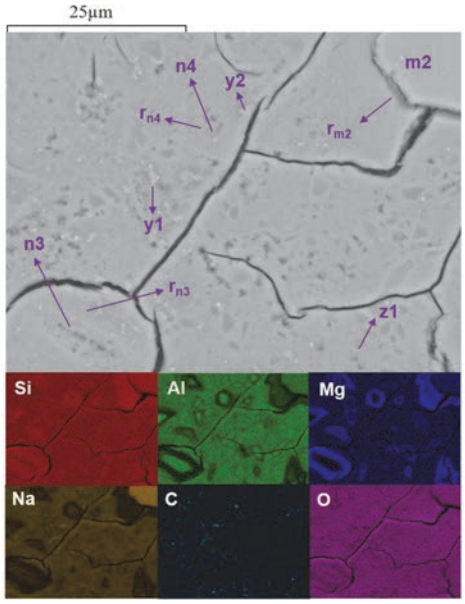

Fig. 34. SEM (high magnification) characterization of AG4 (Reprinted [adapted] under CC BY 4.0 license from Publication III © 2021 Authors).

The possible presence in AAMs of some form of amorphous magnesium silicate other than the traditional M-S-H was first put forward by Walkley et al. [25]. Those authors prepared AAMs in a CaO-MgO-Na_2O-Al_2O_3-SiO_2 regime and observed that hydrotalcite is the main Mg-containing phase in AAMs. However, plotting of the Mg:Al molar ratios (obtained from ESEM-EDS analysis) revealed that this ratio in a few AAMs was considerably larger than expected in a hydrotalcite phase. The authors therefore proposed the possibility of the existence of Mg in an amorphous Mg silicate form, apart from the hydrotalcite phase, since they did not obtain any evidence for the existence of M-S-H, Mg carbonate phases, or brucite in the AAMs.

The distribution of the network-modifying cations (Mg and Na), as observed in the SEM-EDS analysis of AG4 (Fig. 33 and 34), can be explained by considering a role preference among Na and Mg in an aluminosilicate system, as indicated by

the XPS analysis (section 4.1.3). Due to the high CFS of Mg, Mg prefers to neutralize the high negative charge of NBOs (in the case of AG4, NBO is associated with depolymerized silicate species ($Q^{0–3}$(*m*Al)). Due to the low CFS of Na, Na prefers to neutralize the low negative charge of BO (in the case of AG4, BO is attributed to tetrahedral aluminum species, especially those constituting the zeolitic structures). Hence, the preferential association of Na with zeolites and that of Mg with depolymerized silicate species (which results in AMS phase formation) can be explained. The Na/Mg molar ratio (theoretical) is 5.15. Despite the significant excess of Na, Na does not couple with depolymerized silicate species; instead, the excess Na forms thermonatrite, as revealed by XRD analysis (Fig. 27). This highlights the significant impact of CFS on the distribution of Mg and Na in AAM. In conclusion, the higher CFS of Mg (than Na) is the driving factor for AMS phase formation.

The SEM-EDS characterization of AG5 is provided in Fig. 35. The areas m4, m5, and m6 correspond to the unreacted glass precursor. The rims (r_{m4}, r_{m5}, and r_{m6}) around the unreacted glass precursors are richer in Mg, Si, and O and represent the AMS phase. The area n5 corresponds to zeolitic species and has a rim r_{n5} around it that represents the AMS phase. The areas labeled z2 and z3 also correspond to the AMS phase.

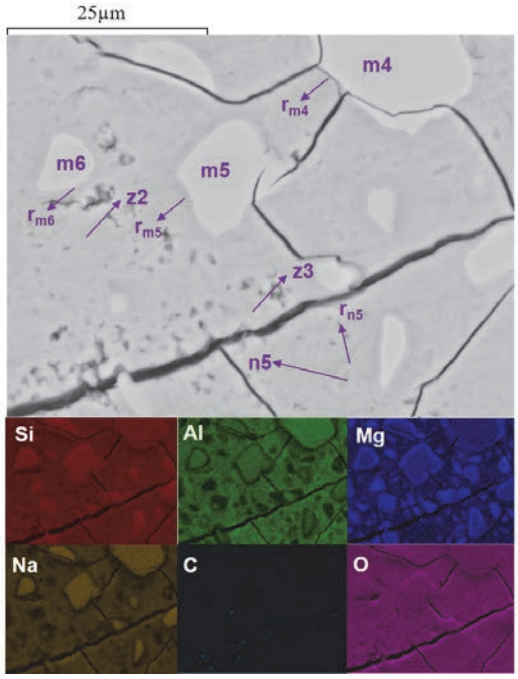

Fig. 35. SEM (high magnification) characterization of AG5 (Reprinted [adapted] under CC BY 4.0 license from Publication III © 2021 Authors).

The SEM-EDS characterization of AG6 is provided in Fig. 36. In this figure, the following areas are identified: m7 corresponds to the unreacted glass precursor; n6 represents a glass precursor that has reacted almost completely; a rim (r_{n6}) denotes the AMS phase; areas z4 and z5 represent the AMS phase; and y3 corresponds to thermonatrite. When compared to AG4 and AG5, the sample AG6 shows poor differentiation between the AMS and zeolitic phases. This could be because, while moving from sample AG4 to AG6, the quantity of extremely depolymerized silicate species (which is the major constituent of the AMS phase) reduces from ≈ 60% to ≈ 32% (Fig. 32). The zeolitic and AMS phases are intermixed in this AAM, resulting in poor differentiation between the AMS and zeolitic phases in the SEM-EDS images.

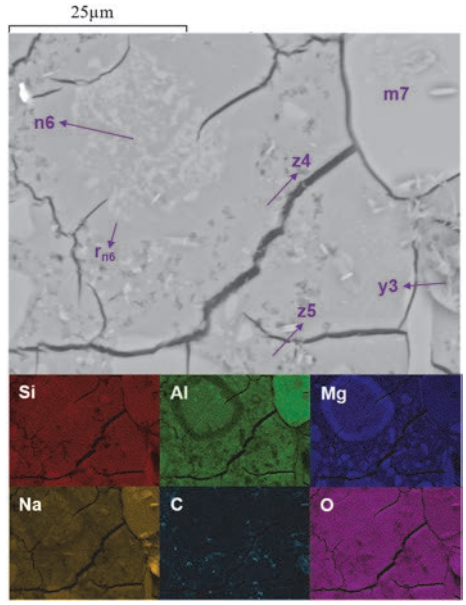

Fig. 36. SEM (high magnification) characterization of AG6 (Reprinted [adapted] under CC BY 4.0 license from Publication III © 2021 Authors).

The SEM-EDS characterization of AG9 is provided in Fig. 37. Even though the unreacted glass precursors (m8, m9, and m10) and the product phases (n7, n8, and n9) are clearly observed, no noticeable differentiation is evident between the AMS and zeolitic phases. The quantity of extremely depolymerized silicate species (which is the major constituent of the AMS phase) in AG9 is ≈ 15% (Fig. 32). The zeolitic and AMS phases are intermixed in this AAM.

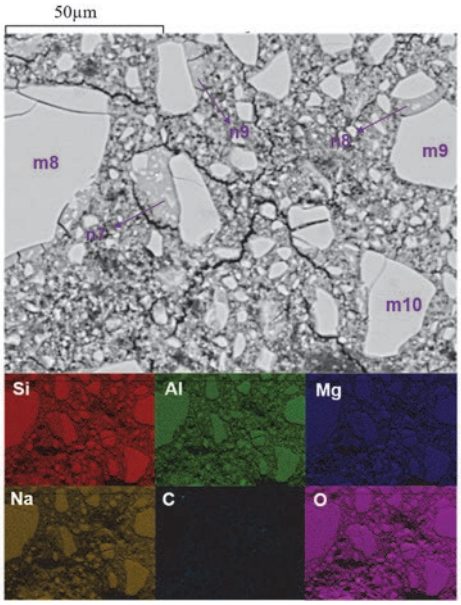

Fig. 37. SEM (high magnification) characterization of AG9 (Reprinted [adapted] under CC BY 4.0 license from Publication III © 2021 Authors).

The following conclusions can be drawn regarding the fate of Mg in AAMs, with the help of SEM-EDS analysis. None of the AAMs showed the following: 1) areas enriched with Al, Mg, and O only (which would correspond to hydrotalcite phases); 2) enriched with Mg, C, and O only (which would indicate magnesium (hydroxy-)carbonates), and 2) areas enriched with Mg and O only (which would represent brucite). Instead, the AAMs exhibited areas enriched with Mg, Si, and O only. This represents an amorphous magnesium silicate (AMS) phase, as the formation of crystalline magnesium silicate or conventional M-S-H was not supported by ^{29}Si MAS NMR analysis (Section 4.3.4) or XRD (Figure 3).

4.3.6 TG-MS characterization of AAMs

The TG-MS characterization of AAMs is provided in Fig. 38. The sample AG4 exhibits a loss of mass at ≈ 100 °C, and this is attributed to molecular water belonging to pore fluid and products such as zeolites. A second loss of mass (from ≈ 500 °C to ≈ 600 °C) is attributed to CO_2 release. This could be associated with decomposition of thermonatrite, which is the only carbonate phase present in AG4,

according to SEM and XRD analysis. Even though true thermonatrite begins to decompose normally at 800 °C, contamination of thermonatrite is known to bring down its decomposition temperature [108]. The sample AG7 also exhibits a mass loss at ≈ 100 °C, but this is less than the corresponding mass loss detected in AG4. This could originate from the lower reactivity of G7 than G4, resulting in fewer products in AG7 (when compared to AG4); therefore, less molecular water is present in AG7 than in AG4. The loss of mass detected at ≈ 100 °C is the lowest among all AAMs and could reflect the fact that G10 is the least reactive among all the glasses.

The TG-MS characterization of the AAMs provides no evidence for the presence of brucite, hydrotalcite, or the traditional M-S-H phase. Brucite, if formed, must produce a loss of mass at ≈ 400 °C [109]. Hydrotalcite, if present, should produce a first loss of mass at ≈ 180 °C and a second loss of mass extending from ≈ 270 °C to ≈ 390 °C [110]. The M-S-H phase, if formed, must show a loss of mass at ≈ 550 °C [111]. The absence of brucite, hydrotalcite, and the M-S-H phase, as indicated by TG-MS characterization, also corroborates the results of XRD, ^{29}Si NMR, ^{27}Al NMR, and the SEM characterization of the AAMs.

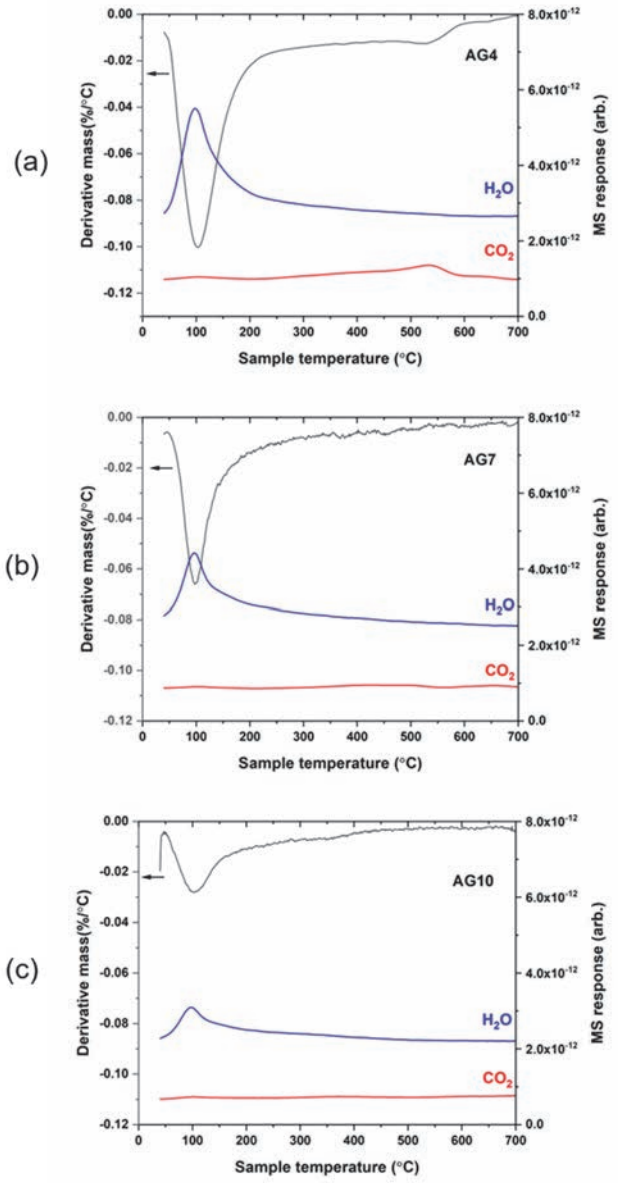

Fig. 38. TG-MS characterization of AG4, AG7, and AG10 (Reprinted [adapted] under CC BY 4.0 license from Publication III © 2021 Authors).

4.4 Alkaline reactivity of thermally treated phlogopite

This section deals with the estimation of the alkaline reactivity of thermally treated phlogopite. The samples were characterized by XRD to understand the phase changes accompanying thermal treatments. Alkaline dissolution experiments were performed to obtain the solubility of Si, Al, K, Mg, and Fe. Residues remaining after alkaline dissolution were examined by TEM to gain insights into the alkaline dissolution process. Acid etching was performed on the residues to obtain a rough estimate of the composition of the precipitated phases.

4.4.1 Phase changes during thermal treatment

The XRD analysis (Fig. 39) of all the samples treated up to 900 °C showed crystalline contributions arising only from phlogopite (PDF no:01-080-4054). This demonstrates the high thermal stability of phlogopite. The samples treated at 1100 °C (P1100) exhibited the presence of phlogopite, as well as phases like magnetite (PDF no: 00-001-1111), leucite (PDF no: 01-076-8732), and forsterite (PDF no: 01-071-6437). This indicates a partial decomposition of phlogopite into new phases. This observation is in line with the findings of Tutti et al. [53], who reported that dehydroxylation and structural decomposition of phlogopite begins at around 900 °C, reaches a maximum around 1100 °C, and completely finishes at 1200 °C. The sample treated at 1200 °C (P1200) contained both leucite and forsterite phases, as observed in the case of P1100, but a new phase (magnesioferrite aluminian; PDF no: 01-073-2410) appeared in place of magnetite. When compared to P1100, P1200 exhibited very minute reflections corresponding to phlogopite, thereby indicating near complete decomposition of phlogopite at 1200 °C. The sample P1300 showed XRD reflections closely similar to those of P1200, indicating that the formed phases are stable at a temperature range of 1200 °C to 1300 °C.

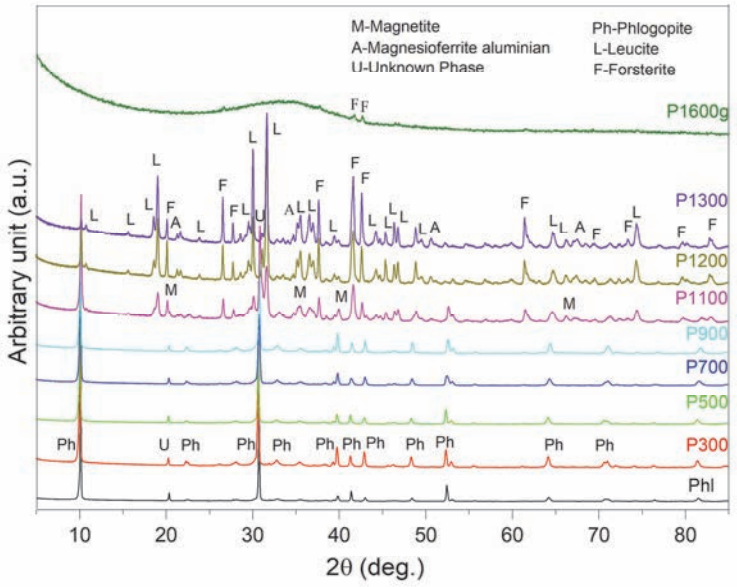

Fig. 39. XRD analysis of thermally treated phlogopite (Reprinted [adapted], with permission, from Publication IV © 2017 Elsevier Ltd.).

P1600, the sample obtained by quenching of molten phlogopite at 1600 °C, showed predominant amorphous features, except for minor contributions from crystalline forsterite (PDF no: 01-073-6339). The temperature-pressure phase diagram (Fig. 3) for the MgO-SiO_2-Al_2O_3-Fe_2O_3-K_2O-O_2 system (which corresponds to phlogopite composition) can explain the precipitation of forsterite. According to the phase diagram, forsterite is the first-precipitating solid phase from the molten slag, and no other solid phases develop in the temperature range of 1400 °C to 1550 °C. The higher temperature (1400 °C to 1550 °C) of the melt implies a greater mobility of ions; hence, the ions can arrange themselves in an orderly manner, leading to the precipitation of crystalline forsterite. The precipitation of all other solid phases happens at lower temperatures (<1400 °C), which reduces the mobility of ions. Hence, those phases precipitate in amorphous forms.

4.4.2 Enhancement in Si and Al solubility upon thermal treatment

The untreated phlogopite (Phl) exhibited very low Si and Al solubility, with both values close to 1 wt.% (Fig. 40), demonstrating the inertness of phlogopite toward alkali activation. For all the samples thermally treated up to 900 °C, Si and Al solubility remained low and comparable to that of Phl. This observation is in line with the thermal stability of phlogopite up to 900 °C, as observed previously by XRD analysis (Fig. 39). The sample P1100 showed improved Si and Al solubility when compared to P900, due to the partial decomposition of phlogopite and evolution of new phases, as indicated by XRD analysis. Both the samples P1200 and P1300 showed similar Si and Al solubility, and the values observed were less than the respective values of P1100. This could reflect the recrystallization of phases around 1200–1300 °C, as indicated by the closely similar reflections of P1200 and P1300 during the XRD analysis.

The sample with highest Si and Al solubility was the glass synthesized at 1600 °C (P1600g). The sample P1600g exhibited roughly 45 wt.% Si solubility and 35 wt.% Al solubility. The performance of P1600g was comparable to that of highly alkali-soluble metakaolin, for which the Si and Al solubilities were 26 wt.% and 40 wt.%, respectively. The Al solubility was substantially lower for P1600g than for metakaolin. One of the main reasons is that the Al content was significantly lower in P1600g than in metakaolin (10 wt.% Al in P1600g vs. 36 wt.% Al in metakaolin).

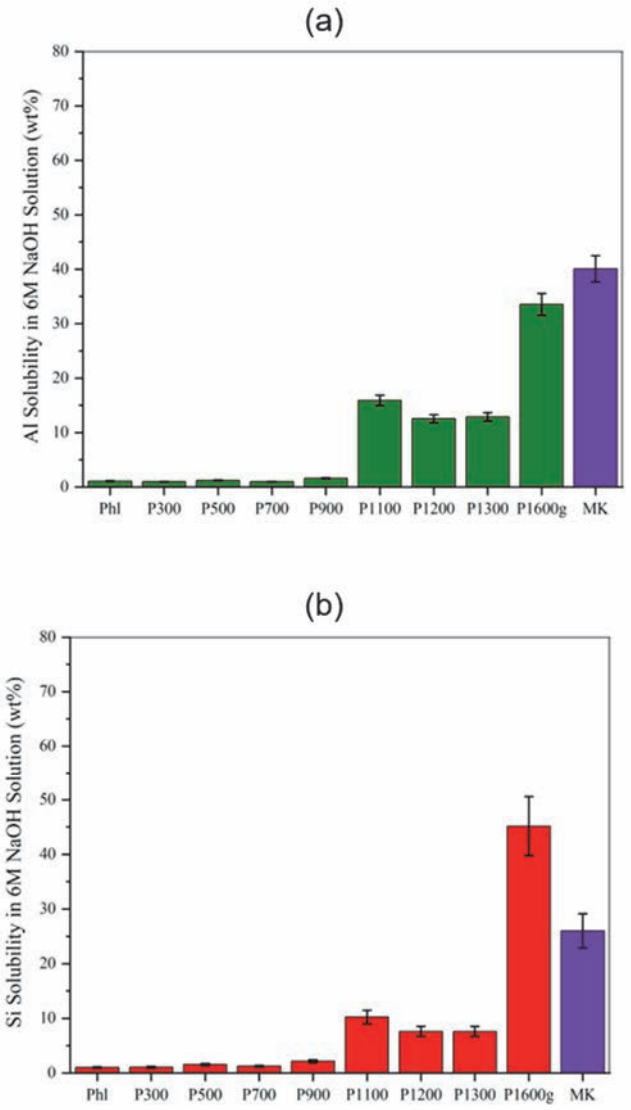

Fig. 40. Alkaline solubility of (a) Al and (b) Si in the case of thermally treated phlogopite samples (Reprinted [adapted], with permission, from Publication IV © 2017 Elsevier Ltd.).

4.4.3 Understanding the K solubility

The untreated phlogopite sample (Phl) showed a K solubility of around 15 wt.% (Fig. 41). The K solubility of Phl is substantially high when compared to the Si and Al solubility for the same sample (Fig. 41). Unlike Si and Al, K is loosely held in the interlayer of phlogopite; hence, K possesses higher mobility than either Si or Al. The K cation can also readily exchange with the smaller Na cation present in the highly concentrated NaOH solution (used in the alkaline dissolution experiment) [112]. These two factors result in a substantially higher K solubility than Si or Al in the same Phl sample. The K solubility in P700 and P900 is low when compared to P500, although no phase change is evident in samples treated up to 900 °C, as indicated by XRD analysis (Fig. 39). This decline in K solubility can be explained by previous high-temperature studies performed on phlogopite [53], [113]. The heating of phlogopite above 500 °C results in a parallel oxidation of Fe^{2+} and dehydrogenation reactions (from OH groups). These two processes are summarized by the equation

$$[2Fe^{2+} + 2OH^{-}]_{\text{phlogopite}} \rightarrow [2Fe^{3+} + 2O^{2-}]_{\text{phlogopite}} + H_2 \uparrow. \quad (3)$$

During this event, the only component lost is hydrogen, which is not a framework component of the phlogopite (Fig. 2). This means that the basic framework of phlogopite remains intact, in agreement with the XRD analysis showing no phase changes in the case of samples treated up to 900 °C. However, as a result of dehydrogenation, the repulsion forces between H^{+} (belonging to OH groups) and interlayer K cation decreases. The reduced repulsion would imply that K is more strongly held in the interlayer than it was before; hence, the K mobility is lower in P700 and P900 than in P500. This explains the reduced K solubility observed in case of P700 and P900 when compared to P500. The trends in K solubility for samples P1100, P1200, and P1300 are similar to the trends observed for both Si and Al. The trends in K solubility of these three samples can be explained by the same logic used previously to explain the trends in Si and Al solubility (Fig. 40).

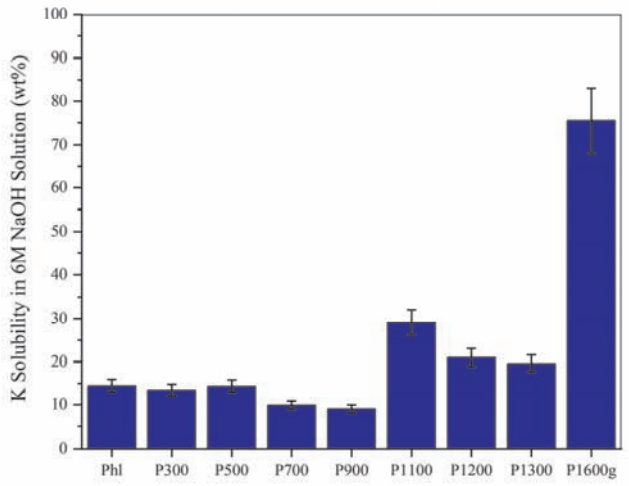

Fig. 41. Alkaline solubility of K in case of thermally treated phlogopite samples (Reprinted [adapted], with permission, from Publication IV © 2017 Elsevier Ltd.).

The K solubility of sample P1600g is around 75 wt.%, and this is very high when compared to either Si or Al solubility in the same sample (Fig. 40). This behavior can be explained using the fundamental concepts of glass chemistry. In glasses, alkali metals like K act as network modifiers, while both Si and Al act as network formers. Network formers are more strongly held than network modifiers [114]. The release of Si and Al from the glass structure is possible only by breakage of the glass network, while the release of K can be accomplished by breakage of glass network as well as by ion exchange with Na cations originating from the NaOH solution. The tendency to form precipitated products is also greater for dissolved Si and Al than for dissolved K. These two factors result in P1600g exhibiting a substantially higher K solubility than for either Si or Al.

4.4.4 Understanding the fate of Fe and Mg

The untreated phlogopite (Phl) showed very negligible Mg and Fe solubility (Fig. 42). The thermal treatment produced no significant impact on the Mg and Fe solubility compared to both Si and Al. Even in case of the most promising sample

P1600g, both Mg and Fe solubility remained less than 5 wt.%. Insights into the fate of Mg and Fe is possible through studies on the solid residues.

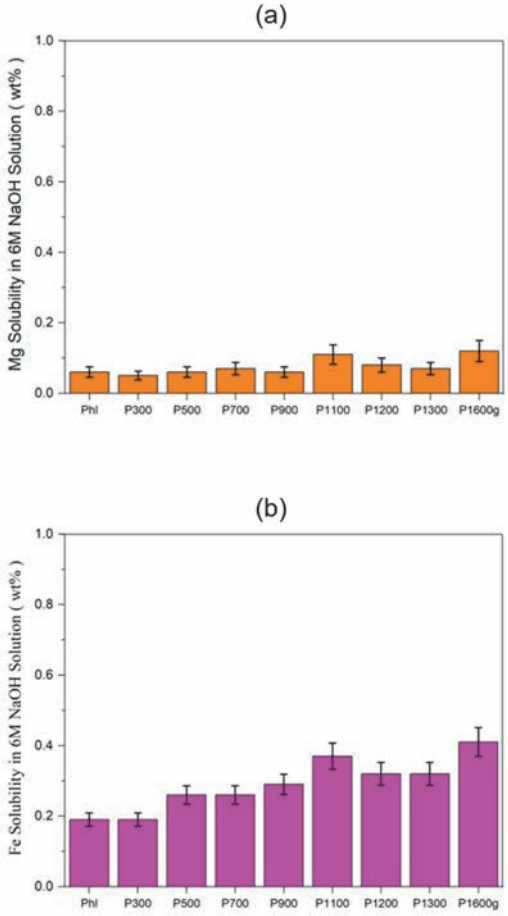

Fig. 42. Alkaline solubility of (a) Mg and (b) Fe (Reprinted [adapted], with permission, from Publication IV © 2017 Elsevier Ltd.).

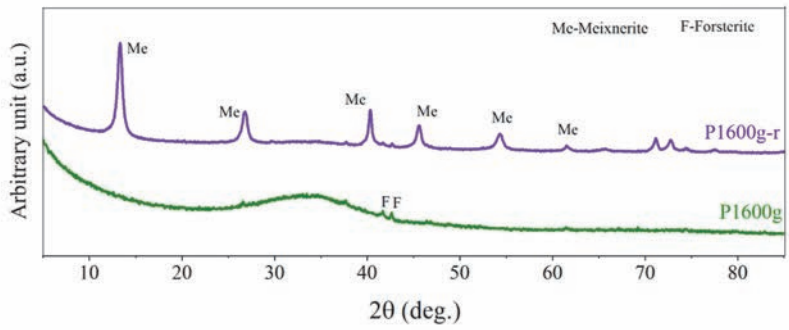

Fig. 43. XRD analysis of the solid residue (P1600g-r) remaining after the alkaline dissolution of P1600g (Reprinted [adapted], with permission, from Publication IV © 2017 Elsevier Ltd.).

The XRD and STEM analysis of the solid residue P1600g-r provided evidence that Mg and Fe are both released during the alkali dissolution process, but they exclusively form precipitated products. Analysis of P1600g-r by XRD (Fig. 43) revealed the formation of crystallites of meixnerite ($Mg_6Al_2(OH)_{18}\cdot 4H_2O$, PDF no: 01-082-8043). Unlike Al-containing meixnerite, no Si-containing precipitated product was detected during XRD analysis. This could be one of the reasons for the high Si solubility (45 wt.%) when compared to Al solubility (33 wt.%) observed during the alkaline dissolution of P1600g (Fig. 40).

STEM characterization was done for P1600g and P1600g-r, the solid residue obtained from P1600g. P1600g included irregularly shaped particles with even distribution of all major elemental constituents (Fig. 44), thereby indicating a homogenous glassy material. In the case of P1600g-r, unreacted material and precipitated products are clearly visible. Precipitated products are observed around the unreacted material, as well in the form of individual clusters. The precipitated phases are rich in Mg, Fe, and Al, in agreement with the XRD analysis (Fig. 39), which revealed crystalline meixnerite. The Fe present in the precipitate could form amorphous products; hence, it would not be detected in the previous XRD analysis. In short, STEM analysis indicated that both Mg and Fe are released during the alkaline dissolution process, but they formed precipitated products exclusively.

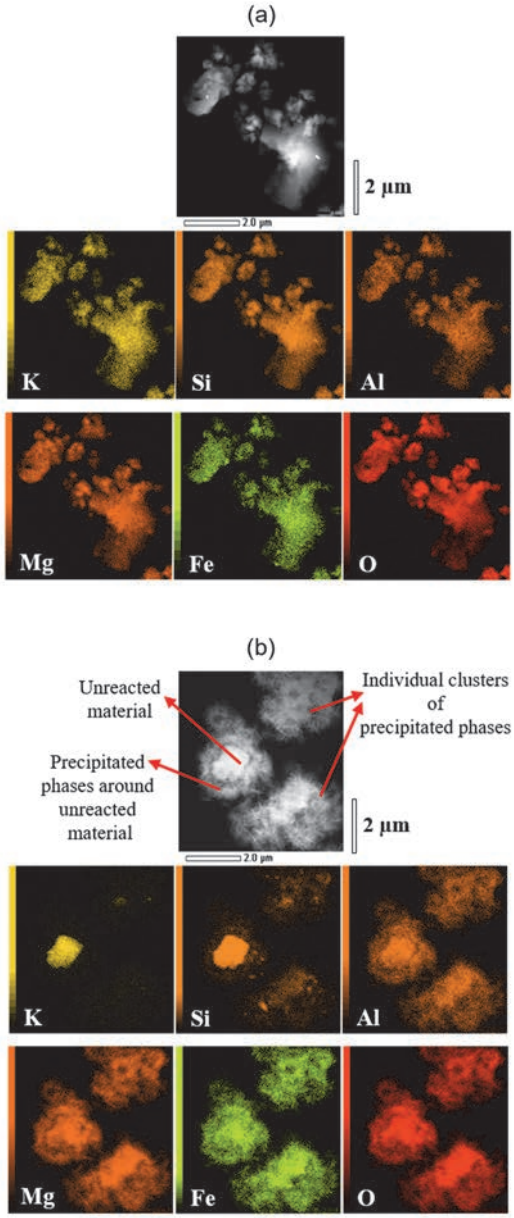

Fig. 44. STEM images along with elemental mapping for (a) P1600g and (b) P1600g-r (Reprinted [adapted], with permission, from Publication IV © 2017 Elsevier Ltd.).

4.4.5 Estimation of the composition of the precipitated products

The solubility of elements (mainly Si and Al) calculated from the alkaline solubility test is often used to estimate the potential of a material for alkali activation [115], [116]. However, during the actual synthesis of AAMs, both the soluble fraction and the precipitated fraction contribute to the development of the binder phase. Hence, estimation of the composition of the precipitated fraction, apart from the soluble fraction, is also relevant in the case of the alkaline solubility test. For this purpose, the acid solubility of the solid residue (P1600g-r) is determined to estimate the composition of the precipitated products. This estimation process assumes that the elements are homogenously distributed in the precursor (P1600g), as well as in the precipitated products.

Performing the acid solubility test for the residue (P1600g-r) in a series of concentrations of acid provides a rough estimation of the composition of the precipitated products. During the dissolution of residues in a low concentration of acid, the precipitated products (when compared to unreacted material) will be mainly dissolved (as precipitated products surround the unreacted material (Fig. 44). This implies that the filtrate (obtained from the acid dissolution experiment) will be richer in Mg, Al, and Fe, as these elements form the main constituents of the precipitated products. Increasing the concentration of acid used in the acid solubility test will eventually identify a point when the precipitated products are almost completely dissolved, thereby leading to greater dissolution of inner unreacted material. The unreacted material (when compared to precipitated products) has a higher concentration of Si and K (Fig. 44). Hence, when the unreacted material is significantly dissolved during the solubility test in a highly concentrated acid, an increase will appear in the slopes of Si and K, while the slopes of K, Mg, and Fe will decrease. This transition in slopes is observed between 0.03 and 0.1 M nitric acid (Fig. 45), implying that the composition corresponding to 0.03 M nitric acid roughly represents the lower limit of precipitated product composition, while the composition corresponding to 0.1 M nitric acid is a rough estimation of the upper limit of the precipitate composition (refer Table 6 for compositions). In this way, a rough estimation of the precipitated products can be obtained as follows: Mg (34–80%), Fe (29–76%), Al (21–46%), Si (5–33%), and K (1–8%).

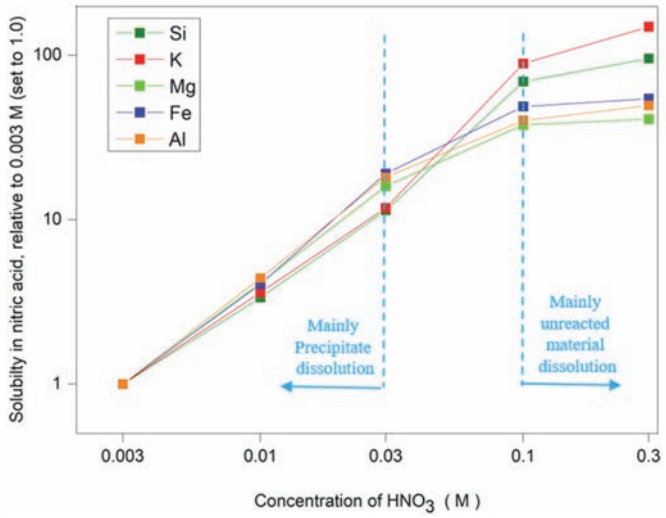

Fig. 45. The solubility of P1600g-r in nitric acid as a function of the nitric acid concentration. Solubility values are normalized with respect to the solubility in 0.003 M nitric acid to understand the trend (Reprinted [adapted], with permission, from Publication IV © 2017 Elsevier Ltd.).

Table 6. Solubility of various elemental constituents of P1600g-r in nitric acid (Reprinted [adapted], with permission, from Publication IV © 2017 Elsevier Ltd.).

Concentration of nitric acid (M)	Si (wt.%)	Al (wt.%)	Mg (wt.%)	Fe (wt.%)	K (wt.%)
0.003	0.48	1.15	2.12	1.56	0.09
0.01	1.60	5.06	8.72	6.34	0.33
0.03	5.41	20.83	33.89	29.75	1.07
0.1	32.92	46.04	79.84	76.25	8.11
0.3	45.53	56.91	86.62	84.97	13.56

4.4.6 The overall alkali activation potential of P1600g

The overall alkali activation potential of P1600g is represented by the total material reacted during the alkali dissolution and includes the soluble fraction and the precipitated fraction. Table 7 shows the overall alkali activation potential of P1600g. A significant proportion of the structure-forming elements (Si, Al, Mg, and Fe) is available for alkali activation. The unreacted material was obtained through mass balance.

Table 7. The overall alkali activation potential of P1600g (Reprinted [adapted], with permission, from Publication IV © 2017 Elsevier Ltd.).

Element	Overall potential for alkali activation			Unreacted material (wt.%)	Total (wt%)
	Solution (wt.%)	Precipitate (wt.%)	Total (wt.%)		
Si	57	5–33	62–90	10–28	100
Al	35	21–46	56–81	19–44	100
Mg	<0.5	34–80	34–80	20–66	100
Fe	<0.5	29–76	29–76	24–61	100
K	76	1–8	77–84	16–23	100

5 Conclusion and outlook

This thesis deals with the synthesis and alkali activation of Mg-rich aluminosilicates. The specific objectives involved the following: synthesis, characterization, and calculation of reactivity of Na-Mg aluminosilicate glasses; preparation of AAMs from the aluminosilicate glasses; detailed analysis of those AAMs to gain insights into the fate of Mg; and assessment of the potential of phlogopite as a Mg-rich precursor in the context of AA. In addressing these objectives, the major accomplishments made in this thesis can be summarized as follows.

The structure of the prepared Na-Mg aluminosilicate glasses is greatly influenced by the CFS of the network-modifying cations (Na and Mg). The higher CFS of Mg than Na means that Mg preferentially acts as a network modifier, while Na exhibits a preference for a charge-compensation role. Mg can effectively charge stabilize the NBO (with a higher negative charge density), while Na can effectively charge stabilize BO (with a lower negative charge density). When Na is replaced by Mg as the network modifier, this reduces the proportion of Q^3 species and increases the proportion of Q^2 species. When Mg replaces Na as a charge compensator, the following changes occur: 1) the amount of Al-rich Q^4 species (Q^4(3Al) & Q^4(4Al)) decreases, while the quantity of the Al-poor Q^4 species (Q^4(1Al) & Q^4(2Al)) increases; and 2) an enhanced propensity for Si and Al phase separation occurs in the aluminosilicate glasses. A summary of these findings is shown in Fig. 46.

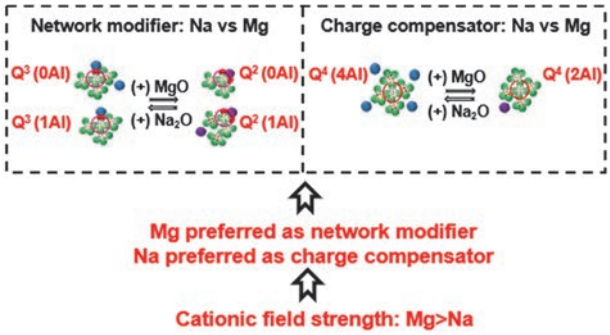

Fig. 46. The CFS of Mg and Na dictates the structure of Na-Mg aluminosilicate glasses (Reprinted [adapted] under CC BY 4.0 license from Publication I © 2020 Authors).

Alkaline dissolution experiments were performed to estimate the reactivity of Na-Mg aluminosilicate glasses. Reactivity is a prerequisite, but not a sufficient condition, for a promising raw material for AAMs. During the alkaline dissolution of glasses under the conditions used here, Al forms precipitated products in the form of hydrotalcite-group phases, while Si does not form any noticeable precipitated products. Hence, the solubility of Si can be used to represent the true reactivity of the glasses. The Si solubility analysis reveals the following trend in glass reactivity: An increase in Mg content of the glasses causes an initial increase in the reactivity of the glasses; the reactivity then attains a maximum, followed by a drop. The traditional parameters for estimating glass reactivity (optical basicity and NBO/T) cannot explain this observed trend in glass reactivity. Since NBO/T is the same for all the glasses, the glasses should exhibit similar reactivity on this basis, but the experimentally determined glass reactivities contradict this expectation. The other traditional parameter used for estimating glass reactivity, namely optical basicity, also does not fully account for the glass reactivity trend. Replacement of Na by Mg leads to a reduction in optical basicity, indicating that glass reactivity should drop with the introduction of Mg. This may be the reason behind the reduction in glass reactivity after the achievement of the maximum value of glass reactivity. However, it cannot explain the initial rise in the reactivity of the glasses. The glass reactivity (as observed in this study) is influenced by two factors: optical basicity and depolymerization of glasses. During the initial replacement of Na by Mg, the influence of glass depolymerization dominates over that of optical basicity, leading to a rise in glass reactivity. However, with greater replacement of Na by Mg, the influence of optical basicity dominates over that of glass depolymerization, leading to a drop in glass reactivity. Fig. 47 summarizes the analysis performed to estimate the reactivity of the glasses.

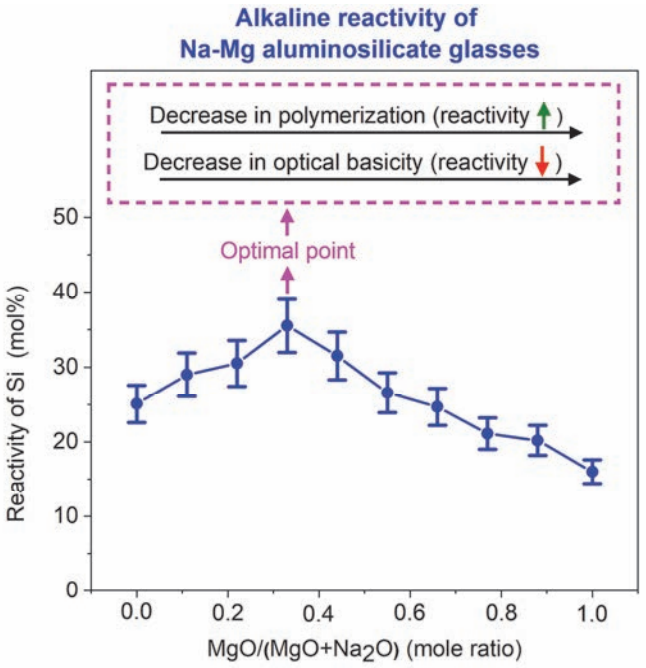

Fig. 47. Alkaline reactivity of Na-Mg aluminosilicate glasses influenced by depolymerization and optical basicity (Reprinted [adapted] under CC BY 4.0 license from Publication II © 2020 Authors).

The Na-Mg aluminosilicate glasses have been alkali-activated to produce AAMs with the main purpose of understanding the fate of Mg. Zeolites are the dominant crystalline product phase detected in all AAMs. The hydrotalcite phase is absent in this system, and this is attributed to the preferential incorporation of Al into zeolites. The major zeolites (garronite and LSX) detected in the AAMs possess a Si:Al ratio of 1, while the Si:Al ratio of all the glasses used for their synthesis is 2.5. This indicates that Al will act as a limiting reactant during the production of zeolites from glasses; hence, no Al will remain after zeolite production for the formation of hydrotalcite. Thorough characterization of the AAMs by XRD, ^{29}Si NMR, ^{27}Al NMR, TG-MS, and SEM provided no evidence for the existence of the following phases: 1) magnesium (hydroxy-)carbonates; 2) brucite; or 3) traditional magnesium silicate hydrate (M-S-H) phases. The Mg in AAMs instead occurs as an amorphous magnesium silicate (AMS) phase, the existence of which is not well documented in the literature. The driving force for AMS formation is the high CFS

of Mg (compared to Na), which results in Mg efficiently stabilizing the negative charge of the NBO belonging to the depolymerized silicate species. Hence, the possible presence of an AMS phase must be considered in Mg-rich AAMs, particularly in complex systems where its presence may be difficult to confirm. Fig. 48 summarizes the analysis conducted to understand the fate of Mg in AAMs.

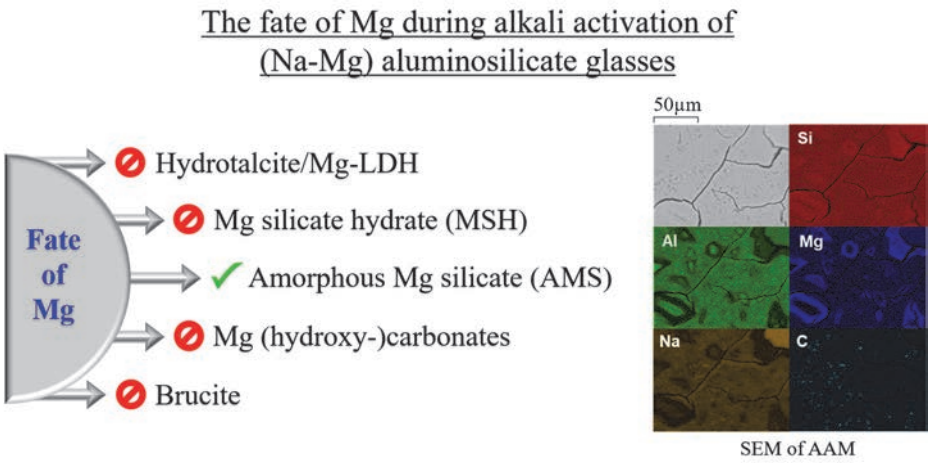

Fig. 48. The fate of Mg during alkali activation of Na-Mg aluminosilicate glasses (Under CC BY 4.0 license from Graphical abstract of Publication III © 2021 Authors).

Studies on the assessment of phlogopite as a Mg-rich precursor for alkali activation indicated that the untreated phlogopite is highly inert. The untreated phlogopite showed very low Si and Al solubilities (both values around 1 wt.%); however, thermal treatment could enhance the alkaline reactivity of phlogopite. The highest reactivity was achieved in the case of P1600g, the sample produced by rapid quenching of the phlogopite melt produced at 1600 °C. The Si and Al solubilities (45% and 33%, respectively) exhibited by P1600g are comparable to that of highly soluble metakaolin (26% Si and 40% Al). During alkali dissolution, significant proportions of Mg and Fe are also released, but they exclusively formed precipitated products. Meixnerite ($Mg_6Al_2(OH)_{18}\cdot 4H_2O$), a hydrotalcite-like compound, is the only crystalline precipitated phase. Note that the production of P1600g requires temperatures as high as 1600 °C, and this may potentially pose practical difficulties due to the high energy demand. However, this temperature is used primarily to ensure complete melting of the sample. In practical cases, the melting temperatures could be brought down by the application of fluxes like CaO

or Na_2O. If the melting temperature can be lowered to around 1450 °C, this would be in the same operational range as used for Portland cement and blast furnace slag production. Fig. 49 summarizes the studies conducted to estimate the AA potential of phlogopite.

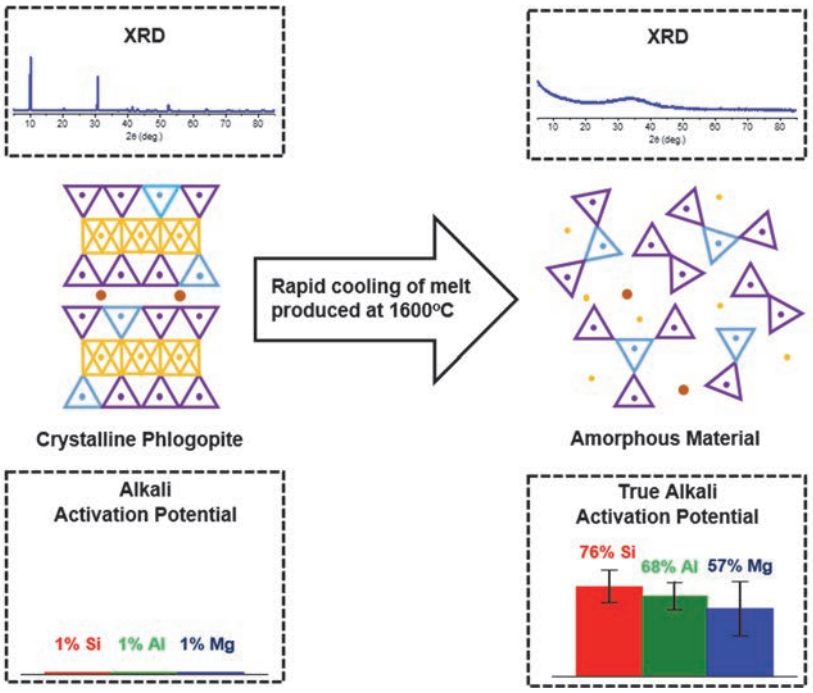

Fig. 49. Improving the alkali activation potential of phlogopite through thermal treatment (Reprinted [adapted], with permission, from Graphical abstract of Publication IV © 2017 Elsevier Ltd.).

This thesis work reveals the prospects of several relevant research themes for potential future scientific investigations. These include the following:

1. Detailed studies to understand how the AMS phase impacts the various properties of AAMs, such as compressive strength, shrinkage, chemical durability, fire resistance, etc.
2. Determination of how the formation of the AMS phase is affected by the presence of Ca in the precursor (possibly through detailed characterization of AAMs prepared from synthetic Na-Mg-Ca aluminosilicate glasses).

3. Determination of whether the AMS phase possibly transforms into M-S-H phases due to changes in conditions (for example, due to changes in pH of the system).
4. Studies focusing on reducing the melting temperature of phlogopite and other natural Mg silicate minerals to lower the cost and carbon footprint associated with the process.
5. Estimation of the alkali activation potential of other abundantly available and non-carbonate Mg-rich precursors.

List of references

[1] P. M. Vitousek, "Beyond Global Warming: Ecology and Global Change," *Ecology*, vol. 75, no. 7, pp. 1861–1876, 1994, doi: 10.2307/1941591.

[2] "AR5 Climate Change 2014: Mitigation of Climate Change - IPCC." https://www.ipcc.ch/report/ar5/wg3/ (accessed May 24, 2021).

[3] International Energy Agency, *Cement Technology Roadmap: Carbon Emissions Reductions up to 2050*. OECD, 2009. doi: 10.1787/9789264088061-en.

[4] J. S. Damtoft, J. Lukasik, D. Herfort, D. Sorrentino, and E. M. Gartner, "Sustainable development and climate change initiatives," *Cem. Concr. Res.*, vol. 38, no. 2, pp. 115–127, Feb. 2008, doi: 10.1016/j.cemconres.2007.09.008.

[5] J. S. J. van Deventer, C. E. White, and R. J. Myers, "A Roadmap for Production of Cement and Concrete with Low-CO_2 Emissions," *Waste Biomass Valor.*, vol. 12, no. 2, pp. 4745–4775, Aug. 2020, doi: 10.1007/s12649-020-01180-5.

[6] Intergovernmental Panel on Climate Change and O. Edenhofer, Eds., *Climate change 2014: mitigation of climate change: Working Group III contribution to the Fifth Assessment Report of the Intergovernmental Panel on Climate Change*. New York, NY: Cambridge University Press, 2014.

[7] G. Habert, "10 - Assessing the environmental impact of conventional and 'green' cement production," in *Eco-efficient Construction and Building Materials*, F. Pacheco-Torgal, L. F. Cabeza, J. Labrincha, and A. de Magalhães, Eds. Woodhead Publishing, 2014, pp. 199–238. doi: 10.1533/9780857097729.2.199.

[8] J. Provis and J. Deventer, *Alkali Activated Materials: State-of-the-Art Report, RILEM TC 224-AAM*. 2014. doi: 10.1007/978-94-007-7672-2.

[9] P. Duxson, A. Fernández-Jiménez, J. L. Provis, G. C. Lukey, A. Palomo, and J. S. J. van Deventer, "Geopolymer technology: the current state of the art," *J. Mater. Sci.*, vol. 42, no. 9, pp. 2917–2933, May 2007, doi: 10.1007/s10853-006-0637-z.

[10] S. Ruan and C. Unluer, "Comparative life cycle assessment of reactive MgO and Portland cement production," *J. of Clean. Prod.*, vol. 137, pp. 258–273, Nov. 2016, doi: 10.1016/j.jclepro.2016.07.071.

[11] F. Jin, K. Gu, and A. Al-Tabbaa, "Strength and drying shrinkage of reactive MgO modified alkali-activated slag paste," *Constr. Build. Mater.*, vol. 51, pp. 395–404, Jan. 2014, doi: 10.1016/j.conbuildmat.2013.10.081.

[12] S. A. Walling and J. L. Provis, "Magnesia-Based Cements: A Journey of 150 Years, and Cements for the Future?" *Chem. Rev.*, vol. 116, no. 7, pp. 4170–4204, Apr. 2016, doi: 10.1021/acs.chemrev.5b00463.

[13] M. B. Haha, B. Lothenbach, G. Le Saout, and F. Winnefeld, "Influence of slag chemistry on the hydration of alkali-activated blast-furnace slag — Part I: Effect of MgO," *Cem. Concr. Res.*, vol. 41, no. 9, pp. 955–963, Sep. 2011, doi: 10.1016/j.cemconres.2011.05.002.

[14] X. Ke, S. A. Bernal, and J. L. Provis, "Uptake of chloride and carbonate by Mg-Al and Ca-Al layered double hydroxides in simulated pore solutions of alkali-activated

slag cement," *Cem. Concr. Res.*, vol. 100, pp. 1–13, Oct. 2017, doi: 10.1016/j.cemconres.2017.05.015.

[15] S. A. Bernal *et al.*, "MgO content of slag controls phase evolution and structural changes induced by accelerated carbonation in alkali-activated binders," *Cem. Concr. Res.*, vol. 57, pp. 33–43, Mar. 2014, doi: 10.1016/j.cemconres.2013.12.003.

[16] Y. Chen and J. Wei, "Hydrated magnesium silicate system gelling material coagulating and hardening at normal temperature and its preparation method," CN1594195A, Mar. 16, 2005 Accessed: Aug. 15, 2020. [Online]. Available: https://patents.google.com/patent/CN1594195A/en

[17] S. A. Walling, H. Kinoshita, S. A. Bernal, N. C. Collier, and J. L. Provis, "Structure and properties of binder gels formed in the system $Mg(OH)_2$–SiO_2–H_2O for immobilisation of Magnox sludge," *Dalton Trans.*, vol. 44, no. 17, pp. 8126–8137, Apr. 2015, doi: 10.1039/C5DT00877H.

[18] T. Zhang, C. R. Cheeseman, and L. J. Vandeperre, "Development of low pH cement systems forming magnesium silicate hydrate (M-S-H)," *Cem. Concr. Res.*, vol. 41, no. 4, pp. 439–442, Apr. 2011, doi: 10.1016/j.cemconres.2011.01.016.

[19] N. Mobasher, S. A. Bernal, and J. L. Provis, "Structural evolution of an alkali sulfate activated slag cement," *J. Nucl. Mater.*, vol. 468, pp. 97–104, Jan. 2016, doi: 10.1016/j.jnucmat.2015.11.016.

[20] A. Buchwald, H. Hilbig, and Ch. Kaps, "Alkali-activated metakaolin-slag blends—performance and structure in dependence of their composition," *J. Mater. Sci.*, vol. 42, no. 9, pp. 3024–3032, May 2007, doi: 10.1007/s10853-006-0525-6.

[21] A. F. Abdalqader, F. Jin, and A. Al-Tabbaa, "Characterisation of reactive magnesia and sodium carbonate-activated fly ash/slag paste blends," *Constr. Build. Mater.*, vol. 93, pp. 506–513, Sep. 2015, doi: 10.1016/j.conbuildmat.2015.06.015.

[22] S. A. Walling, S. A. Bernal, L. J. Gardner, H. Kinoshita, and J. L. Provis, "Blast furnace slag-$Mg(OH)_2$ cements activated by sodium carbonate," *RSC Adv.*, vol. 8, no. 41, pp. 23101–23118, Jun. 2018, doi: 10.1039/C8RA03717E.

[23] O. Burciaga-Díaz and I. Betancourt-Castillo, "Characterization of novel blast-furnace slag cement pastes and mortars activated with a reactive mixture of MgO-NaOH," *Cem. Concr. Res.*, vol. 105, pp. 54–63, Mar. 2018, doi: 10.1016/j.cemconres.2018.01.002.

[24] J. Yliniemi, B. Walkley, J. L. Provis, P. Kinnunen, and M. Illikainen, "Nanostructural evolution of alkali-activated mineral wools," *Cem. Concr. Compos.*, vol. 106, p. 103472, Feb. 2020, doi: 10.1016/j.cemconcomp.2019.103472.

[25] B. Walkley, R. San Nicolas, M.-A. Sani, S. A. Bernal, J. S. J. van Deventer, and J. L. Provis, "Structural evolution of synthetic alkali-activated CaO-MgO-Na_2O-Al_2O_3-SiO_2 materials is influenced by Mg content," *Cem. Concr. Res.*, vol. 99, pp. 155–171, Sep. 2017, doi: 10.1016/j.cemconres.2017.05.006.

[26] Y. Chen, Z. Shui, W. Chen, Q. Li, and G. Chen, "Effect of MgO content of synthetic slag on the formation of Mg-Al LDHs and sulfate resistance of slag-fly ash-clinker binder," *Constr. Build. Mater.*, vol. 125, pp. 766–774, Oct. 2016, doi: 10.1016/j.conbuildmat.2016.08.086.

[27] T. Yang, Z. Zhang, H. Zhu, X. Gao, C. Dai, and Q. Wu, "Re-examining the suitability of high magnesium nickel slag as precursors for alkali-activated materials," *Constr. Build. Mater.*, vol. 213, pp. 109–120, Jul. 2019, doi: 10.1016/j.conbuildmat.2019.04.063.

[28] S. A. Walling, S. A. Bernal, L. J. Gardner, H. Kinoshita, and J. L. Provis, "Phase Formation and Evolution in $Mg(OH)_2$–Zeolite Cements," *Ind. Eng. Chem. Res.*, vol. 57, no. 6, pp. 2105–2113, Feb. 2018, doi: 10.1021/acs.iecr.7b04201.

[29] T. Yang, X. Yao, and Z. Zhang, "Geopolymer prepared with high-magnesium nickel slag: Characterization of properties and microstructure," *Constr. Build. Mater.*, vol. 59, pp. 188–194, May 2014, doi: 10.1016/j.conbuildmat.2014.01.038.

[30] P. Kinnunen, J. Yliniemi, B. Talling, and M. Illikainen, "Rockwool waste in fly ash geopolymer composites," *J. Mater. Cycles Waste Manag.*, vol. 19, no. 3, pp. 1220–1227, Jul. 2017, doi: 10.1007/s10163-016-0514-z.

[31] Y. J. Zhang, Y. L. Zhao, H. H. Li, and D. L. Xu, "Structure characterization of hydration products generated by alkaline activation of granulated blast furnace slag," *J. Mater. Sci.*, vol. 43, no. 22, pp. 7141–7147, Nov. 2008, doi: 10.1007/s10853-008-3028-9.

[32] B. O. Mysen, D. Virgo, and F. A. Seifert, "The structure of silicate melts: Implications for chemical and physical properties of natural magma," *Rev. Geophys.*, vol. 20, no. 3, pp. 353–383, 1982, doi: 10.1029/RG020i003p00353.

[33] L. M. Thompson and J. F. Stebbins, "Non-stoichiometric non-bridging oxygens and five-coordinated aluminum in alkaline earth aluminosilicate glasses: Effect of modifier cation size," *J. Non-Cryst. Solids*, vol. 358, no. 15, pp. 1783–1789, Aug. 2012, doi: 10.1016/j.jnoncrysol.2012.05.022.

[34] C. Le Losq and D. R. Neuville, "Effect of the Na/K mixing on the structure and the rheology of tectosilicate silica-rich melts," *Chem. Geol.*, vol. 346, pp. 57–71, May 2013, doi: 10.1016/j.chemgeo.2012.09.009.

[35] A. Quintas, D. Caurant, O. Majérus, T. Charpentier, and J.-L. Dussossoy, "Effect of the nature of alkali and alkaline-earth oxides on the structure and crystallization of an aluminoborosilicate glass developed to immobilize highly concentrated nuclear waste solutions," *arXiv:0912.1576 [cond-mat]*, Dec. 2009, Accessed: Feb. 19, 2020. [Online]. Available: http://arxiv.org/abs/0912.1576

[36] A. R. Allu *et al.*, "Structure and crystallization of alkaline-earth aluminosilicate glasses: prevention of the alumina-avoidance principle," *J. Phys. Chem. B*, vol. 122, no. 17, pp. 4737–4747, May 2018, doi: 10.1021/acs.jpcb.8b01811.

[37] J. R. Allwardt *et al.*, "Effect of structural transitions on properties of high-pressure silicate melts: ^{27}Al NMR, glass densities, and melt viscosities," *Am. Min.*, vol. 92, no. 7, pp. 1093–1104, Jul. 2007, doi: 10.2138/am.2007.2530.

[38] D. R. Neuville *et al.*, "Amorphous materials: Properties, structure, and durability: Structure of Mg- and Mg/Ca aluminosilicate glasses: ^{27}Al NMR and Raman spectroscopy investigations," *Am. Min.*, vol. 93, no. 11–12, pp. 1721–1731, Nov. 2008, doi: 10.2138/am.2008.2867.

[39] R. G. Kuryaeva, “The state of magnesium in silicate glasses and melts,” *Glass Phys. Chem.*, vol. 35, no. 4, pp. 378–383, Aug. 2009, doi: 10.1134/S1087659609040051.

[40] S. Bista and J. F. Stebbins, “The role of modifier cations in network cation coordination increases with pressure in aluminosilicate glasses and melts from 1 to 3 GPa,” *Am. Min.*, vol. 102, no. 8, pp. 1657–1666, Aug. 2017, doi: 10.2138/am-2017-6081.

[41] C. Weigel *et al.*, “Elastic moduli of $XAlSiO_4$ aluminosilicate glasses: effects of charge-balancing cations,” *J. Non-Cryst. Solids*, vol. 447, pp. 267–272, Sep. 2016, doi: 10.1016/j.jnoncrysol.2016.06.023.

[42] S. K. Lee, H.-I. Kim, E. J. Kim, K. Y. Mun, and S. Ryu, “Extent of Disorder in Magnesium Aluminosilicate Glasses: Insights from ^{27}Al and ^{17}O NMR,” *J. Phys. Chem. C*, vol. 120, no. 1, pp. 737–749, Jan. 2016, doi: 10.1021/acs.jpcc.5b10799.

[43] K. C. Mills and S. Sridhar, “Viscosities of ironmaking and steelmaking slags,” *Ironmak. Steelmak.*, vol. 26, no. 4, pp. 262–268, Aug. 1999, doi: 10.1179/030192399677121.

[44] P. T. Durdziński, R. Snellings, C. F. Dunant, M. B. Haha, and K. L. Scrivener, “Fly ash as an assemblage of model Ca–Mg–Na-aluminosilicate glasses,” *Cem. Concr. Res.*, vol. 78, pp. 263–272, Dec. 2015, doi: 10.1016/j.cemconres.2015.08.005.

[45] D. J. Sosinsky and I. D. Sommerville, “The composition and temperature dependence of the sulfide capacity of metallurgical slags,” *MTB*, vol. 17, no. 2, pp. 331–337, Jun. 1986, doi: 10.1007/BF02655080.

[46] L. S. Dent-Glasser and J. A. Duffy, “Analysis and prediction of acid–base reactions between oxides and oxysalts using the optical basicity concept,” *J. Chem. Soc., Dalton Trans.*, no. 10, pp. 2323–2328, Jan. 1987, doi: 10.1039/DT9870002323.

[47] J. A. Duffy and M. D. Ingram, “An interpretation of glass chemistry in terms of the optical basicity concept,” *J. Non-Cryst. Solids*, vol. 21, no. 3, pp. 373–410, Aug. 1976, doi: 10.1016/0022-3093(76)90027-2.

[48] E. M. Gartner and D. E. Macphee, “A physico-chemical basis for novel cementitious binders,” *Cem. Concr. Res.*, vol. 41, no. 7, pp. 736–749, Jul. 2011, doi: 10.1016/j.cemconres.2011.03.006.

[49] H. Airi, H. Olli, K. Kirsi, and S. Tuuli, “The Effect of Phlogopite Mica on the Sintering Point and Colour of a Claybody,” *Key Eng. Mater.*, 1997. https://www.scientific.net/KEM.132-136.2156 (accessed Nov. 17, 2020).

[50] W. D. Maier, R. Lahtinen, and H. O’Brien, *Mineral Deposits of Finland*. Elsevier, 2015.

[51] J. H. Rayner, “The crystal structure of phlogopite by neutron diffraction,” *Mineral. Mag.*, vol. 39, no. 308, pp. 850–856, Dec. 1974, doi: 10.1180/minmag.1974.039.308.04.

[52] P. Condamine and E. Médard, “Experimental melting of phlogopite-bearing mantle at 1 GPa: Implications for potassic magmatism,” *Earth Planet. Sci. Lett.*, vol. 397, pp. 80–92, Jul. 2014, doi: 10.1016/j.epsl.2014.04.027.

[53] F. Tutti, L. S. Dubrovinsky, and M. Nygren, “High-temperature study and thermal expansion of phlogopite,” *Phys. Chem. Min.*, vol. 27, no. 9, pp. 599–603, Nov. 2000, doi: 10.1007/s002690000098.

[54] G. Habert, N. Choupay, G. Escadeillas, D. Guillaume, and J. M. Montel, “Clay content of argillites: Influence on cement-based mortars,” *Appl. Clay Sci.*, vol. 43, no. 3, pp. 322–330, Mar. 2009, doi: 10.1016/j.clay.2008.09.009.

[55] S. C. Taylor-Lange, E. L. Lamon, K. A. Riding, and M. C. G. Juenger, “Calcined kaolinite–bentonite clay blends as supplementary cementitious materials,” *Appl. Clay Sci.*, vol. 108, pp. 84–93, May 2015, doi: 10.1016/j.clay.2015.01.025.

[56] H. Xu and J. S. J. Van Deventer, “Geopolymerisation of multiple minerals,” *Min. Eng.*, vol. 15, no. 12, pp. 1131–1139, Dec. 2002, doi: 10.1016/S0892-6875(02)00255-8.

[57] J. Ambroise, J. Gniewek, J. Dejean, and J. Pera, “Hydration of synthetic pozzolanic binders obtained by thermal activation of montmorillonite.,” *Am. Ceram. Soc. Bull.*, vol. 66, no. 12, pp. 1731–1733, 1987.

[58] C. He, E. Makovicky, and B. Osbæck, “Thermal stability and pozzolanic activity of raw and calcined mixed-layer mica/smectite,” *Appl. Clay Sci.*, vol. 17, no. 3, pp. 141–161, Sep. 2000, doi: 10.1016/S0169-1317(00)00011-9.

[59] A. McIntosh, S. E. M. Lawther, J. Kwasny, M. N. Soutsos, D. Cleland, and S. Nanukuttan, “Selection and characterisation of geological materials for use as geopolymer precursors,” *Adv. Appl. Ceram.*, vol. 114, no. 7, pp. 378–385, Oct. 2015, doi: 10.1179/1743676115Y.0000000055.

[60] M. N. Rhyner, “The Coulter Principle for Analysis of Subvisible Particles in Protein Formulations,” *AAPS J*, vol. 13, no. 1, pp. 54–58, Dec. 2010, doi: 10.1208/s12248-010-9245-6.

[61] T. D. T. Oyedotun, “X-ray fluorescence (XRF) in the investigation of the composition of earth materials: a review and an overview,” *Geo. Eco. Land.*, vol. 2, no. 2, pp. 148–154, Apr. 2018, doi: 10.1080/24749508.2018.1452459.

[62] A. A. Kovalev, L. A. Tishchenko, V. D. Shashurin, and A. L. Galinovskii, “Application of X-ray Diffraction Methods to Studying Materials,” *Russ. Metall.*, vol. 2017, no. 13, pp. 1186–1193, Dec. 2017, doi: 10.1134/S0036029517130110.

[63] M. He, B. Hu, B. Chen, and Z. Jiang, “Inductively Coupled Plasma Optical Emission Spectrometry for Rare Earth Elements Analysis,” *Phys. Sci. Rev.*, vol. 2, no. 1, Jan. 2017, doi: 10.1515/psr-2016-0059.

[64] P. J. Kempen, A. S. Thakor, C. Zavaleta, S. S. Gambhir, and R. Sinclair, “A Scanning Transmission Electron Microscopy (STEM) Approach to Analyzing Large Volumes of Tissue to Detect Nanoparticles,” *Microsc. Microanal.*, vol. 19, no. 5, pp. 1290–1297, Oct. 2013, doi: 10.1017/S143192761300192X.

[65] M. J. Duer, “The Basics of Solid-State NMR,” in *Solid-State NMR Spectroscopy Principles and Applications*, John Wiley & Sons, Ltd, 2001, pp. 1–72. doi: 10.1002/9780470999394.ch1.

[66] J. D. Andrade, “X-ray Photoelectron Spectroscopy (XPS),” in *Surface and Interfacial Aspects of Biomedical Polymers: Volume 1 Surface Chemistry and*

Physics, J. D. Andrade, Ed. Boston, MA: Springer US, 1985, pp. 105–195. doi: 10.1007/978-1-4684-8610-0_5.

[67] J. I. Goldstein, D. E. Newbury, J. R. Michael, N. W. M. Ritchie, J. H. J. Scott, and D. C. Joy, "SEM Image Interpretation," in *Scanning Electron Microscopy and X-Ray Microanalysis*, J. I. Goldstein, D. E. Newbury, J. R. Michael, N. W. M. Ritchie, J. H. J. Scott, and D. C. Joy, Eds. New York, NY: Springer, 2018, pp. 111–121. doi: 10.1007/978-1-4939-6676-9_7.

[68] B. Ravel and M. Newville, "Athena, artemis, hephaestus: data analysis for X-ray absorption spectroscopy using IFEFFIT," *J. Synchrotron. Radiat.*, vol. 12, no. Pt 4, pp. 537–541, Jul. 2005, doi: 10.1107/S0909049505012719.

[69] J. Yano and V. K. Yachandra, "X-ray absorption spectroscopy," *Photosynth. Res.*, vol. 102, no. 2, pp. 241–254, 2009, doi: 10.1007/s11120-009-9473-8.

[70] N. K. Nasikas, A. Chrissanthopoulos, N. Bouropoulos, S. Sen, and G. N. Papatheodorou, "Silicate glasses at the ionic limit: alkaline-earth sub-orthosilicates," *Chem. Mater.*, vol. 23, no. 16, pp. 36929–36972, Aug. 2011, doi: 10.1021/cm2012582.

[71] P. Hudon and D. R. Baker, "The nature of phase separation in binary oxide melts and glasses. I. Silicate systems," *J. Non-Cryst. Solids*, vol. 303, no. 3, pp. 299–345, Jun. 2002, doi: 10.1016/S0022-3093(02)01043-8.

[72] N. Kreidl, "Phase separation in glasses," *J. Non-Cryst. Solids*, vol. 129, no. 1, pp. 1–11, Mar. 1991, doi: 10.1016/0022-3093(91)90074-G.

[73] G. V. Gibbs, D. F. Cox, T. D. Crawford, K. M. Rosso, N. L. Ross, and R. T. Downs, "Classification of metal-oxide bonded interactions based on local potential- and kinetic-energy densities," *J. Chem. Phys.*, vol. 124, no. 8, p. 084704, Feb. 2006, doi: 10.1063/1.2161425.

[74] H. Sreenivasan *et al.*, "Field strength of network modifying cation dictates the structure of (Na-Mg) aluminosilicate glasses," *Front. Mater.*, vol. 7, 2020, doi: 10.3389/fmats.2020.00267.

[75] T. L. Barr, "The nature of the relative bonding chemistry in zeolites: An XPS study," *Zeol.*, vol. 10, no. 8, pp. 760–765, Nov. 1990, doi: 10.1016/0144-2449(90)90058-Y.

[76] B. O. Mysen, A. Lucier, and G. D. Cody, "The structural behavior of Al^{3+} in peralkaline melts and glasses in the system Na_2O-Al_2O_3-SiO_2," *Am. Min.*, vol. 88, no. 11–12, pp. 1668–1678, Nov. 2003, doi: 10.2138/am-2003-11-1206.

[77] B. Walkley and J. L. Provis, "Solid-state nuclear magnetic resonance spectroscopy of cements," *Mater. Today Adv.*, vol. 1, p. 100007, Mar. 2019, doi: 10.1016/j.mtadv.2019.100007.

[78] J. Mahler and A. Sebald, "Deconvolution of ^{29}Si magic-angle spinning nuclear magnetic resonance spectra of silicate glasses revisited — some critical comments," *Solid State Nucl. Magn. Reson.*, vol. 5, no. 1, pp. 63–78, Oct. 1995, doi: 10.1016/0926-2040(95)00027-N.

[79] J. Schneider, V. R. Mastelaro, H. Panepucci, and E. D. Zanotto, "^{29}Si MAS–NMR studies of Q^n structural units in metasilicate glasses and their nucleating ability," *J.*

Non-Cryst. Solids, vol. 273, no. 1, pp. 8–18, Aug. 2000, doi: 10.1016/S0022-3093(00)00139-3.

[80] S. K. Lee and J. F. Stebbins, "The degree of aluminum avoidance in aluminosilicate glasses," *Am. Min.*, vol. 84, no. 5–6, pp. 937–945, May 1999, doi: 10.2138/am-1999-5-631.

[81] A. R. Jones, R. Winter, G. N. Greaves, and I. H. Smith, "MAS NMR study of soda-lime–silicate glasses with variable degree of polymerisation," *J. Non-Cryst. Solids*, vol. 293–295, pp. 87–92, Nov. 2001, doi: 10.1016/S0022-3093(01)00656-1.

[82] D. R. Neuville, "Viscosity, structure and mixing in (Ca, Na) silicate melts," *Chem. Geo.*, vol. 229, no. 1, pp. 28–41, May 2006, doi: 10.1016/j.chemgeo.2006.01.008.

[83] E. Gambuzzi, A. Pedone, M. C. Menziani, F. Angeli, D. Caurant, and T. Charpentier, "Probing silicon and aluminium chemical environments in silicate and aluminosilicate glasses by solid state NMR spectroscopy and accurate first-principles calculations," *Geochim. Cosmochim. Acta*, vol. 125, pp. 170–185, Jan. 2014, doi: 10.1016/j.gca.2013.10.025.

[84] S. K. Lee, "Microscopic origins of macroscopic properties of silicate melts and glasses at ambient and high pressure: Implications for melt generation and dynamics," *Geochim. Cosmochim. Acta*, vol. 69, no. 14, pp. 3695–3710, Jul. 2005, doi: 10.1016/j.gca.2005.03.011.

[85] D. R. Neuville, L. Cormier, and D. Massiot, "Al environment in tectosilicate and peraluminous glasses: A ^{27}Al MQ-MAS NMR, Raman, and XANES investigation," *Geochim. Cosmochim. Acta*, vol. 68, no. 24, pp. 5071–5079, Dec. 2004, doi: 10.1016/j.gca.2004.05.048.

[86] B. O. Mysen, D. Virgo, and I. Kushiro, "The structural role of aluminum in silicate melts-A Raman spectroscopic study at 1 atmosphere," *Am. Min.*, vol. 66, no. 7–8, pp. 678–701, Aug. 1981.

[87] B. O. Mysen, "Structure and properties of magmatic liquids: from haplobasalt to haploandesite," *Geochim. Cosmochim. Acta*, vol. 63, no. 1, pp. 95–112, Jan. 1999, doi: 10.1016/S0016-7037(98)00273-7.

[88] G. S. Henderson, "A Si K-edge EXAFS/XANES study of sodium silicate glasses," *J. Non-Cryst. Solids*, vol. 183, no. 1, pp. 43–50, Apr. 1995, doi: 10.1016/0022-3093(94)00651-2.

[89] B. J. A. Moulton *et al.*, "The structure of haplobasaltic glasses investigated using X-ray absorption near edge structure (XANES) spectroscopy at the Si, Al, Mg, and O K-edges and Ca, Si, and Al L2,3-edges," *Chem. Geo.*, vol. 420, pp. 213–230, Jan. 2016, doi: 10.1016/j.chemgeo.2015.11.016.

[90] D. Li *et al.*, "X-ray absorption spectroscopy of silicon dioxide (SiO_2) polymorphs: The structural characterization of opal," *Am. Min.*, vol. 79, no. 7–8, pp. 622–632, Aug. 1994.

[91] G. S. Henderson and J. C. St-Amour, "A Si K-edge XANES study of Ti containing alkali/alkaline-earth silicate glasses," *Chem. Geo.*, vol. 213, no. 1, pp. 31–40, Dec. 2004, doi: 10.1016/j.chemgeo.2004.08.030.

[92] P. Lagarde, A. M. Flank, G. Tourillon, R. C. Liebermann, and J. P. Itie, "X-ray absorption near edge structure of quartz. Application to the structure of densified silica," *J. Phys. I France*, vol. 2, no. 6, pp. 1043–1050, Jun. 1992, doi: 10.1051/jp1:1992113.

[93] I. Davoli *et al.*, "Structure of densified vitreous silica: Silicon and oxygen XANES spectra and multiple scattering calculations," *Phys. Chem. Miner.*, vol. 19, no. 3, pp. 171–175, Sep. 1992, doi: 10.1007/BF00202105.

[94] C. Levelut, D. Cabaret, M. Benoit, P. Jund, and A.-M. Flank, "Multiple scattering calculations of the XANES Si K-edge in amorphous silica," *J. Non-Cryst. Solids*, vol. 293–295, pp. 100–104, Nov. 2001, doi: 10.1016/S0022-3093(01)00658-5.

[95] S. Bender, R. Franke, E. Hartmann, V. Lansmann, M. Jansen, and J. Hormes, "X-ray absorption and photoemission electron spectroscopic investigation of crystalline and amorphous barium silicates," *J. Non-Cryst. Solids*, vol. 298, no. 2, pp. 99–108, Mar. 2002, doi: 10.1016/S0022-3093(02)00943-2.

[96] P. Faucon, T. Charpentier, D. Bertrandie, A. Nonat, J. Virlet, and J. C. Petit, "Characterization of calcium aluminate hydrates and related hydrates of cement pastes by ^{27}Al MQ-MAS NMR," *Inorg. Chem.*, vol. 37, no. 15, pp. 3726–3733, Jul. 1998, doi: 10.1021/ic9800076.

[97] A. Perez, D. Daval, M. Fournier, M. Vital, J.-M. Delaye, and S. Gin, "Comparing the reactivity of glasses with their crystalline equivalents: The case study of plagioclase feldspar," *Geochim. Cosmochim. Acta*, vol. 254, pp. 122–141, Jun. 2019, doi: 10.1016/j.gca.2019.03.030.

[98] A. Rodrigues, S. Fearn, and M. Vilarigues, "Mixed reactions: Glass durability and the mixed-alkali effect," *J. Am. Cer. Soc.*, vol. 102, no. 12, pp. 7278–7287, 2019, doi: 10.1111/jace.16665.

[99] B. C. Bunker, G. W. Arnold, E. K. Beauchamp, and D. E. Day, "Mechanisms for alkali leaching in mized-Na/K silicate glasses," *J. Non-Cryst. Solids*, vol. 58, no. 2, pp. 295–322, Nov. 1983, doi: 10.1016/0022-3093(83)90031-5.

[100] B. M. J. Smets and M. G. W. Tholen, "The absence of a mixed-alkali effect in the leaching of corrosion-resistant glasses," *J. Mater. Sci.*, vol. 20, no. 3, pp. 1027–1032, Mar. 1985, doi: 10.1007/BF00585747.

[101] D. E. Day, "Mixed alkali glasses — Their properties and uses," *J. Non-Cryst. Solids*, vol. 21, no. 453, pp. 11343–11372, Aug. 1976, doi: 10.1016/0022-3093(76)90026-0.

[102] W. Zhifang, Z. Nai, M. Bo, and S. Zhongxin, "Study of the mixed alkali effect on chemical durability of alkali silicate glasses," *J. Non-Cryst. Solids*, vol. 84, no. 1, pp. 468–476, Jul. 1986, doi: 10.1016/0022-3093(86)90811-2.

[103] B. Lothenbach, D. Nied, E. L'Hôpital, G. Achiedo, and A. Dauzères, "Magnesium and calcium silicate hydrates," *Cem. Concr. Res.*, vol. 77, pp. 60–68, Nov. 2015, doi: 10.1016/j.cemconres.2015.06.007.

[104] S. K. Lee and J. F. Stebbins, "The Structure of Aluminosilicate Glasses: High-Resolution ^{17}O and ^{27}Al MAS and 3QMAS NMR Study," *J. Phys. Chem. B*, vol. 104, no. 17, pp. 4091–4100, May 2000, doi: 10.1021/jp994273w.

[105] G. Engelhardt, “Chapter 9 Solid state NMR spectroscopy applied to zeolites,” in *Studies in Surface Science and Catalysis*, vol. 137, H. van Bekkum, E. M. Flanigen, P. A. Jacobs, and J. C. Jansen, Eds. Elsevier, 2001, pp. 387–418. doi: 10.1016/S0167-2991(01)80251-2.

[106] S. A. Bernal *et al.*, “Gel nanostructure in alkali-activated binders based on slag and fly ash, and effects of accelerated carbonation,” *Cem. Concr. Res.*, vol. 53, pp. 127–144, Nov. 2013, doi: 10.1016/j.cemconres.2013.06.007.

[107] D. Nied, K. Enemark-Rasmussen, E. L’Hopital, J. Skibsted, and B. Lothenbach, “Properties of magnesium silicate hydrates (M-S-H),” *Cem. Concr, Res.*, vol. 79, pp. 323–332, Jan. 2016, doi: 10.1016/j.cemconres.2015.10.003.

[108] R. V. Siriwardane, J. A. Poston, C. Robinson, and T. Simonyi, “Effect of additives on decomposition of sodium carbonate: precombustion CO_2 capture sorbent regeneration,” *Energy Fuels*, vol. 25, no. 3, pp. 1284–1293, Mar. 2011, doi: 10.1021/ef101486m.

[109] K. J. D. MacKenzie and R. H. Meinhold, “Thermal decomposition of brucite, $Mg(OH)_2$: A ^{25}Mg MAS NMR study,” *Thermochim. Acta*, vol. 230, pp. 339–343, Dec. 1993, doi: 10.1016/0040-6031(93)80371-G.

[110] F. Rey, V. Fornés, and J. M. Rojo, “Thermal decomposition of hydrotalcites. An infrared and nuclear magnetic resonance spectroscopic study,” *J. Chem. Soc., Faraday Trans.*, vol. 88, no. 15, pp. 2233–2238, 1992, doi: 10.1039/FT9928802233.

[111] S. A. Walling, H. Kinoshita, S. A. Bernal, N. C. Collier, and J. L. Provis, “Structure and properties of binder gels formed in the system $Mg(OH)_2$–SiO_2–H_2O for immobilisation of Magnox sludge,” *Dalton Trans.*, vol. 44, no. 17, pp. 8126–8137, Apr. 2015, doi: 10.1039/C5DT00877H.

[112] N. Sánchez-Pastor, K. Aldushin, G. Jordan, and W. W. Schmahl, “K^+–Na^+ exchange in phlogopite on the scale of a single layer,” *Geochim. Cosmochim. Acta*, vol. 74, no. 7, pp. 1954–1962, Apr. 2010, doi: 10.1016/j.gca.2009.12.026.

[113] G. Ventruti, M. Zema, F. Scordari, and G. Pedrazzi, “Thermal behavior of a Ti-rich phlogopite from Mt. Vulture (Potenza, Italy): An in-situ X-ray single-crystal diffraction study,” *Am. Miner.*, vol. 93, no. 4, pp. 632–643, Apr. 2008, doi: 10.2138/am.2008.2700.

[114] A. Campopiano *et al.*, “Dissolution of glass wool, rock wool and alkaline earth silicate wool: Morphological and chemical changes in fibers,” *Regul. Toxicol. Pharmacol.*, vol. 70, no. 1, pp. 393–406, Oct. 2014, doi: 10.1016/j.yrtph.2014.05.023.

[115] Y. Pontikes *et al.*, “Slags with a high Al and Fe content as precursors for inorganic polymers,” *Appl. Clay Sci.*, vol. 73, pp. 93–102, Mar. 2013, doi: 10.1016/j.clay.2012.09.020.

[116] T. Seiffarth, M. Hohmann, K. Posern, and Ch. Kaps, “Effect of thermal pre-treatment conditions of common clays on the performance of clay-based geopolymeric binders,” *Appl. Clay Sci*, vol. 73, pp. 35–41, Mar. 2013, doi: 10.1016/j.clay.2012.09.010.

Original publications

This thesis is based on the following publications, which are referred to throughout the text by their Roman numerals:

I Sreenivasan, H., Kinnunen, P., Adesanya E., Patanen, M., Kantola, A. M., Telkki, V.-V., Huttula, M., Cao, W., Provis, J. L., & Illikainen, M. (2020). Field strength of network-modifying cation dictates the structure of (Na-Mg) aluminosilicate glasses. *Frontiers in Materials, 7*, 267. https://doi.org/10.3389/fmats.2020.00267

II Sreenivasan, H., Cao, W., Hu Y., Xiao, Q., Shakouri, M., Huttula, M., Provis, J. L., Illikainen, M., & Kinnunen, P. (2020). Towards designing reactive glasses for alkali activation: Understanding the origins of alkaline reactivity of Na-Mg aluminosilicate glasses. *PlOS ONE, 15*(12), e0244621. https://doi.org/10.1371/journal.pone.0244621

III Sreenivasan, H., Adesanya E., Niu, H., Perumal, P., Kantola, A. M., Telkki, V.-V., Huttula, M., Cao, W., Provis, J. L., Illikainen, M., & Kinnunen, P. (2021). Evidence of formation of an amorphous magnesium silicate (AMS) phase during alkali activation of (Na-Mg) aluminosilicate glasses. *Cement and Concrete Research, 145*,106464. https://doi.org/10.1016/j.cemconres.2021.106464

IV Sreenivasan, H., Kinnunen, P., Heikkinen, E.-P., & Illikainen, M. (2017). Thermally treated phlogopite as magnesium-rich precursor for alkali activation purpose. *Minerals Engineering, 113*, 47–54. https://doi.org/10.1016/j.mineng.2017.08.003

Original publications are not included in the electronic version of the dissertation.

[1]https://creativecommons.org/licenses/by/4.0/

787. Miettinen, Jyrki & Visuri, Ville-Valtteri & Fabritius, Timo (2021) Carbon-containing thermodynamic descriptions of the Fe–Cr–Cu–Mo–Ni–C system for modeling the solidification of steels

788. Tavakolian, Mohammad (2021) Efficient spatiotemporal representation learning for pain intensity estimation from facial expressions

789. Longi, Henna (2021) Regional innovation systems and company engagement in the Arctic context

790. Moltafet, Mohammad (2021) Information freshness in wireless networks

791. Nevanperä, Tuomas (2021) Catalytic oxidation of harmful chlorine- and sulphur-containing VOC emissions : a study of supported Au, Pt and Cu catalysts

792. Baharmast, Aram (2021) Wide dynamic range CMOS receiver techniques for a pulsed Time-of-Flight laser rangefinder

793. Haiko, Oskari (2021) Effect of microstructural characteristics and mechanical properties on the impact-abrasive and abrasive wear resistance of ultra-high strength steels

794. Oppenlaender, Jonas (2021) Crowdsourcing creative work

795. Kimbi Yaah, Velma Beri (2021) Development of novel biomass-based materials for the treatment of emerging contaminants in water

796. Liu, Chen-Feng (2021) Resource allocation for ultra-reliable and low-latency 5G communication

797. Kilpijärvi, Joni (2021) RF-microwave sensor development for cell and human in vitro and ex vivo monitoring

798. Huikari, Jaakko (2021) 2D CMOS SPAD array techniques in 1D pulsed TOF distance measurement applications

799. Peyvasteh, Motahareh (2021) Polarimetric and spectral imaging approaches for quantitative characterization of inhomogeneous scattering media including biotissues

800. Shehab, Mohammad (2021) Energy efficient QoS provisioning and resource allocation for machine type communication

801. Jounila, Henri (2021) Integroidulla HSEQ-johtamisella kokonaisvaltaista yritysvastuullisuutta : tapaustutkimuksia yritysten työturvallisuuden ja HSEQ:n kehittämisestä

Book orders:
Virtual book store
http://verkkokauppa.juvenesprint.fi

UNIVERSITY OF OULU P.O. Box 8000 FI-90014 UNIVERSITY OF OULU FINLAND

ACTA UNIVERSITATIS OULUENSIS

ISBN 978-952-62-3058-0 (Paperback)
ISBN 978-952-62-3059-7 (PDF)
ISSN 0355-3213 (Print)
ISSN 1796-2226 (Online)

UNIVERSITY OF OULU